

**AIR-SEA COUPLING OVER THE EQUATORIAL  
INDIAN OCEAN**

**Dissertation**

**Submitted in partial fulfillment for the award of the degree of**

*Master of Technology*

*In*

*Atmospheric Science*

**By**

**GOPIKA.N**

**Department of Atmospheric Science**

**Cochin University of Science and Technology**

**Cochin, Kerala-682016**

**Under the guidance of**

**Dr. S. PRASANNA KUMAR**

**Scientist F**

**Physical Oceanography Division**

**National Institute of Oceanography**

**Dona Paula, Goa-403004**

**July 2006 to April-2007**

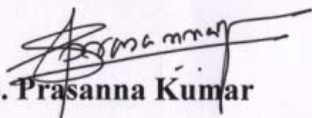
**Dr. S. Prasannakumar**

Deputy Director & Scientist F  
Physical Oceanography Division  
**E-mail: prasanna@nio.org**

Date: 10 April 2007

**CERTIFICATE**

This is to certify that **Miss Gopika.N**, student of Master of Technology (M.Tech Atmospheric Science) from Department of Atmospheric Science, Cochin University of Science and Technology, Cochin-682016, Kerala, India, has successfully undertaken and completed her project work title "**AIR-SEA COUPLING OVER THE EQUATORIAL INDIAN OCEAN**" under the guidance of **Dr. S, Prasanna Kumar**, at National Institute of Oceanography (NIO), Goa. Miss Gopika.N has done this project during 01/07/2006 to 10/04/2007.

  
**Dr. S. Prasanna Kumar**

Deputy Director

## DECLARATION

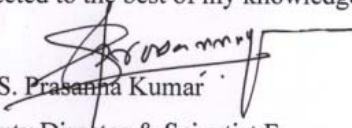
I here by declare that the work which is being presented in dissertation work entitled "**AIR-SEA COUPLING OVER THE EQUATORIAL INDIAN OCEAN**" in partial fulfillment of requirement for the award of degree of **Master of Technology in Atmospheric Science** and submitted in Department of Atmospheric Science, Cochin University of Science and Technology, is an authentic record of my own work, conducted under the supervision of **Dr. S. Prasanna Kumar**, Scientist, POD, National Institute of Oceanography, Goa.

I further declare that to best of my knowledge the dissertation report does not contain any part of work, which has been submitted for the award of any degree either in this University or in any other University without proper citation.



(GOPIKA. N)

This is to certify that, the above statement made by the candidate is corrected to the best of my knowledge.



Dr. S. Prasanna Kumar

Deputy Director & Scientist F

**Physical Oceanography Division**

National Institute of Oceanography

Goa-403004

## ACKNOWLEDGEMENT

First of all I would like to express my earnest gratitude and thankfulness to my guide, **Dr. S. Prasanna Kumar**, Deputy Director & Scientist F, Physical Oceanographic Division, National Institute of Oceanography, Goa. His constant encouragement, keen interest, worthy guidance, valuable suggestion throughout the period has helps me for successful completion of my work.

I would like to express my sincere thanks to **Dr. K. Mohan Kumar**, Dept. of Atmospheric Science, Cochin University of Science and Technology for his valuable suggestions and encouragement. He advised me to carry out my project work at National Institute of Oceanography, Goa.

I am very thankful to **Dr. S. R. Shetye**, Director, National Institute of Oceanography, Goa for permitting me to carry out my project work and providing all the necessary facilities during the course of my work at NIO, Goa.

I would take this opportunity to express my gratitude to the **National Institute of Oceanography, Goa**, for all the facilities provided. In this regard I express my sincere thanks to **Mr. Gourish Salgaonkar**, **Miss. Jayu Narvekar** and **Mr. Nuncio** for their helping nature.

I express my sincere thanks to **Dr.C.A.Babu**, Head of the Dept., Dept. of Atmospheric Science, Cochin University of Science and Technology for his valuable suggestions whenever required during my M.Tech course.

I express my deep sense of gratitude to the **lectures and staff** of the Dept. of Atmospheric Science, Cochin University of Science and Technology for their constant support and encouragement.

My heartfelt thanks to my friend **Miss Deepthi** with whom I spent 10 months of dissertation period and whose constant encouragement and support helped in the completion of my project work.

I would like to express my sincere thanks to my beloved juniors **Balu, Vivek, Ratheesh, Vidya and Smitha** for their help, suggestions and encouragement whenever required.

I would also like to thank my **classmates and friends** for their cooperation and suggestions.

I express my deep sense of gratitude and indebtedness to **my parents, grand parents and relatives** for their prayers and blessings, which have become an indispensable part of my life.

Finally I express my sincere thanks to all those who have extended their help directly or indirectly to make the study a success.

	<b>CONTENTS</b>	<b>Page No.</b>
	<b>LIST OF FIGURES</b>	9
	<b>Chapter 1: Introduction</b>	12
1.1	Introduction	13
1.2	Equatorial Indian Ocean	13
1.3	Geographic location of the study area	17
1.4	Previous Work	18
1.5	Present Work	27
1.5.1	Motivation	27
1.5.2	Objectives	27
	<b>Chapter 2: Data and Methods</b>	29
2.1	Introduction	30
2.1.1	Mixed-layer	30
2.1.2	Barrier layer	31
2.1.3	Mid-Thermocline depth	32
2.2	Data	34
2.2.1	Oceanic data	34
2.2.1.1	Hydrographic data	34
2.2.1.2	Ocean surface current data	35
2.2.2	Atmospheric data	35
2.3	Method	36
2.3.1	Hydrographic data analysis	36
2.3.2	Criteria for selecting the mixed layer depth	50
2.3.3	Criteria for selecting the Barrier layer thickness	50
2.3.4	Criteria for selecting the Mid- thermocline depth	51
2.3.5	Sensible and Latent Heat Fluxes	51
2.3.6	Wind Stress	52

2.3.7	Long wave flux	52
2.3.8	Short wave flux	52
2.3.9	Net Heat flux	53
2.3.10	Precipitation	53
	<b>Chapter 3: Results and Discussion</b>	54
3.1	Seasonal cycle of Oceanic parameters	55
3.1.1	Seasonal cycle of Sea surface temperature	55
3.1.2	Seasonal cycle of Sea surface salinity	58
3.1.3	Seasonal cycle of Mixed layer depth	62
3.1.4	Seasonal cycle of Barrier layer thickness	67
3.1.5	Seasonal cycle of mid-thermocline depth	70
3.1.6	Surface current distributions	73
3.2	Seasonal cycle of Atmospheric parameters	78
3.2.1	Seasonal cycle of air temperature	78
3.2.2	Seasonal cycle of Net evaporation rate	82
3.2.3	Seasonal cycle of Net heat flux	86
3.2.4	Seasonal cycle of Scalar wind	90
3.2.5	Seasonal cycle of wind stress curl	94
	<b>Chapter 4: Summary and Conclusion</b>	99
	<b>REFERENCES</b>	108

## LIST OF FIGURES

Fig. No.	Figure Caption	Page No.
Fig.1	Map showing the area of study.	9
Fig.2	Schematics showing the vertical profiles of temperature (red), salinity (blue), sigma-t (green) and the MLD, BLT, isothermal layer and the D20.	24
Fig.3	Total number of temperature and salinity profile (1202) obtained from CTD and ARGO in each of the 1°×1° grid for the month of January	28
Fig.4	Total number of temperature and salinity profile (1033) obtained from CTD and ARGO in each of the 1°×1° grid for the month of February	29
Fig.5	Total number of temperature and salinity profile (1220) obtained from CTD and ARGO in each of the 1°×1° grid for the month of March	30
Fig.6	Total number of temperature and salinity profile (1334) obtained from CTD and ARGO in each of the 1°×1° grid for the month of April	31
Fig.7	Total number of temperature and salinity profile (1414) obtained from CTD and ARGO in each of the 1°×1° grid for the month of May	32
Fig.8	Total number of temperature and salinity profile (1336) obtained from CTD and ARGO in each of the 1°×1° grid for the month of June	33
Fig.9	Total number of temperature and salinity profile (1759) obtained from CTD and ARGO in each of the 1°×1° grid for the month of July	34
Fig.10	Total number of temperature and salinity profile (1512) obtained from CTD and ARGO in each of the 1°×1° grid for the month of August	35
Fig.11	Total number of temperature and salinity profile (1553) obtained from CTD and ARGO in each of the 1°×1° grid for the month of September	36
Fig.12	Total number of temperature and salinity profile (1512) obtained from CTD and ARGO in each of the 1°×1° grid for the month of October	37



Fig.13	Total number of temperature and salinity profile (1542) obtained from CTD and ARGO in each of the 1°×1° grid for the month of November	38
Fig.14	Total number of temperature and salinity profile (1508) obtained from CTD and ARGO in each of the 1°×1° grid for the month of December	39
Fig.15	Spatial distribution of SST (°C) during spring intermonsoon	47
Fig.16	Spatial distribution of SST (°C) during summer monsoon.	47
Fig.17	Spatial distribution of SST (°C) during fall intermonsoon.	48
Fig.18	Spatial distribution of SST (°C) during winter monsoon.	48
Fig.19	Spatial distribution of SSS (psu) during spring intermonsoon.	51
Fig.20	Spatial distribution of SSS (psu) during summer monsoon.	51
Fig.21	Spatial distribution of SSS (psu) during fall intermonsoon.	52
Fig.22	Spatial distribution of SSS (psu) during winter monsoon.	52
Fig.23	Spatial distribution of MLD (m) during spring intermonsoon.	55
Fig.24	Spatial distribution of MLD (m) during summer monsoon.	55
Fig.25	Spatial distribution of MLD (m) during fall intermonsoon	56
Fig.26	Spatial distribution of MLD (m) during winter monsoon	56
Fig.27	Spatial distribution of BLT (m) during spring intermonsoon.	59
Fig.28	Spatial distribution of BLT (m) during summer monsoon.	59
Fig.29	Spatial distribution of BLT (m) during fall intermonsoon	60
Fig.30	Spatial distribution of BLT (m) during winter	60
Fig.31	Spatial distribution of D20 (m) during spring intermonsoon	61
Fig.32	Spatial distribution of D20 (m) during summer monsoon	62

Fig.33	Spatial distribution of D20 (m) during fall inter-monsoon	63
Fig.34	Spatial distribution of D20 (m) during winter monsoon	63
Fig.35	Surface current distribution during January, February, March and April	66
Fig.36	Surface current distribution during May, June, July and August	67
Fig.37	Surface current distribution during September, October, November and December	68
Fig.38	Air temperature ( $^{\circ}\text{C}$ ) at 10m heights during January, February, March and April.	70
Fig.39	Air temperature ( $^{\circ}\text{C}$ ) at 10m heights during May, June, July and August.	71
Fig.40	Air temperature ( $^{\circ}\text{C}$ ) at 10m heights during September, October, November and December.	72
Fig.41	Fresh water flux (E-P) (m/year) during January, February, March and April.	74
Fig.42	Fresh water flux (E-P) (m/year) during May, June, July and August	75
Fig.43	Fresh water flux (E-P) (m/year) during September, October, November and December	76
Fig.44	Net heat flux ( $\text{W}/\text{m}^2$ ) during January, February, March and April.	78
Fig.45	Net heat flux ( $\text{W}/\text{m}^2$ ) during May, June, July and August	79
Fig.46	Net heat flux ( $\text{W}/\text{m}^2$ ) during September, October, November and December	80
Fig.47	Wind speed (m/s) during January, February, March and April.	82
Fig.48	Wind speed (m/s) during May, June, July and August.	83
Fig.49	Wind speed (m/s) during September, October, November and December.	84
Fig.50	Wind stress curl ( $\text{N}/\text{m}^3$ ) during January, February, March and April	86
Fig.51	Wind stress curl ( $\text{N}/\text{m}^3$ ) during May, June, July and August	87
Fig.52	Wind stress curl ( $\text{N}/\text{m}^3$ ) during September, October, November and December	88

# **Chapter 1**

## **Introduction**

## **1.1 Introduction**

Tropical Ocean plays major roles in the natural variability of the world climate. The Indian Ocean is unique among the three tropical Ocean basins in that it is blocked at 25°N by the Asian land mass. Second, it is not bounded by a "solid" coastal eastern boundary, as the Atlantic and Pacific Oceans are. Next, it is split into two basins - the Arabian Sea and the Bay of Bengal. Thus, the Indian Ocean doesn't have the currents to transport and discharge heat to higher latitudes, as the Gulf Stream and Kuroshio do in the Atlantic and the Pacific, respectively. What's more, it is relatively well connected to the western part of the Pacific Ocean characterized with its "Warm Pool". The two-basin split of the ocean and seasonal heating over this land mass sets the stage for dramatic monsoon wind reversals and intense summer rains over the Indian subcontinent and adjoining areas of Southeast Asia. Recurrence of these summer monsoon rains is critical to agricultural production that provides life-sustaining support for a billion people in the region. The reversing monsoon winds also generate a unique reversing ocean current system unlike those observed in the tropical Atlantic and Pacific, which are under the influence of steadier trade winds.

## **1.2 Equatorial Indian Ocean**

Disappearance of the Coriolis force at the equator as well as its variation with latitude makes the equatorial areas a special region. This makes the equator as a wave-guide within which the signal of atmospheric forcing could be transferred over long distances without much energy loss. For

example, the zonal momentum transferred from the atmosphere to the ocean concentrates on the equator and forms a narrow accelerating jet which moves eastward.

Equatorial Indian Ocean (EIO) behaves uniquely compared to the other regions of the world ocean primarily due to the seasonal reversal of the monsoon winds between winter and summer [Hastenrath & Greishar, 1989]. In boreal winter (December-February) the northeasterly monsoon winds sweep the north Indian Ocean, cross the equator, and recurve to meet the SE trade winds. In boreal summer (June-September) the southeasterly trade winds cross the equator and curve to become the southwesterly monsoon penetrating into the southern part of the Asian continent. In response to the wind reversal, the upper ocean currents also reverse.

In the EIO during the northeast monsoon months (December-February), north equatorial current (NEC) flows westward approximately between  $8^{\circ}\text{N}$  and  $2^{\circ}\text{S}$ . From  $2^{\circ}\text{S}$  to  $8^{\circ}\text{S}$  an equatorial counter current (ECC) flows eastward. South of this is the westwards flowing south equatorial current (SEC), which does not show any seasonal change. The mass convergence at the western boundary due to NEC and SEC drives the equatorial under current (EUC) between 100-250m. This undercurrent exists only during winter when NEC exists. During the southwest monsoon (June-September), NEC changes to eastward flowing summer monsoon current (SMC) combining with ECC. As a result, the surface water is pushed downwind by the equatorial beta plane effect and the water piles up at the eastern end establishing a horizontal pressure gradient beneath the surface water. This phenomenon in the EIO occurs every year with year-to-year variations in the intensities. The most prominent feature of the equatorial Indian Ocean is the semi-annual equatorial Kelvin waves and the

associated eastward jet [Wyrtki, 1973]. These jets form during spring (March-May) and fall (October-November) intermonsoons and flow towards the east as a strong narrow current as it is equatorially trapped. The SST in the eastern equatorial Indian Ocean (90°E-110°E, 10°S-0) is warmer than 27.5°C, the threshold required for deep convection in the tropics [Gadgil *et al.*, 1984], and forms a part of the Indo-Pacific warm pool. The eastern equatorial Indian Ocean experiences heavy rainfall throughout the year resulting in a barrier layer [Sprintall & Tomzak, 1992, Masson *et al.*, 2002] and the barrier layer variability there may play a role in the interannual variability of tropical Indian Ocean. Another distinction of EIO is that equatorial upwelling does not occur in the Indian Ocean as it does in the Pacific and Atlantic. This is because in those oceans, the southeast trade winds blowing across the equator causes surface divergence. However, during summer strong upwelling occurs along the western boundary (along Somalia), and the seasonal cycle of the SST propagates eastward unlike the equatorial Atlantic and Pacific Ocean, where it propagates westward. Also there is a deeper thermocline in the eastern equatorial region and rises in the western equatorial Indian Ocean.

In the Indian Ocean, as the northern region is land-locked by the Asian land mass, these currents cannot export heat to the northern subtropics. The resulting oceanic thermal structure produces feedbacks to the overlying atmosphere that affect not only the monsoon circulation and rainfall patterns, but also weather and climate in remote parts of the globe through atmospheric teleconnections. Sea surface temperature (SST) variance in the Indian Ocean, though small compared to the Pacific Ocean, is an important variable for understanding ocean-atmosphere interactions and predicting climate variability. In the western deep tropics

between the equator and about 10°S, where thermocline domes, the ocean is tightly coupled to the atmosphere [Reverdin, 1987; Murtugudde and Busalacchi, 1999; Xie et al, 2002] and therefore expected to influence the regional climate variability. In recent years Saji et al. [1999] showed that the eastern EIO, which is warmer than the western EIO in normal years, becomes occasionally colder and this condition has been termed as the “Indian Ocean Dipole” mode (IOD). Indian Ocean Dipole (IOD) is a coupled ocean-atmosphere phenomenon. It is characterized by anomalous cooling of SST in the south eastern EIO and anomalous warming of SST in the western EIO. The changes in SST during IOD events are found to be associated with changes in the surface wind field of the central equatorial Indian Ocean. In fact, the winds reverse from the usual westerly to an easterly direction during IOD events [Saji *et al.*, 1999; Webster *et al.*, 1999; Behera and Yamagata, 2001].

IOD develops during April to August and during September to October it matures with warmer than usual SST over large parts of the western equatorial Indian Ocean (WEIO) and cooling in the eastern equatorial Indian Ocean (EEIO). The cold SST anomalies suppress convection over the EEIO and warm SST anomalies enhance the convection over the WEIO; resulting heavy rainfall in the east African region and western coast of India and droughts in Indonesia. During IOD year the eastward propagating Wyrcki jets are weaker. These jets are very strongly influenced by the anomalous westward winds during spring and fall. For reaching the peak phase of IOD with strong east-west gradient in SST anomaly, the increase in SST over the WEIO changes the stability of the overlying air-mass which in turn changes the convection in the boundary layer. Increase in the convective activity leads to strengthen the convergence in the west to central Indian Ocean enhancing the easterly

component of wind over the EEIO. The dipole pattern is not restricted only to SST anomalies. The thermocline rises in the east and deepens in the central and western parts in response to anomalous equatorial winds, thus giving rise to a sub surface dipole [Suryachandra Rao *et al.*,2002]. Dipole mode Index is used to find the strength of the IOD. Dipole Mode Index (DMI) is the difference between western (50°E-70°E, 10°S-10°N) and eastern (90°E-110°E, 10°S-equator) tropical Indian Ocean.

### **1.3 Geographic location of the study area**

The spatial domain selected for the present study is the Equatorial Indian Ocean between latitude 10°S-10°N and longitude between 40°E-110°E (Fig.1). This region is selected for study because it is a region of intense air-sea interaction, equatorial waves and semi-annually reversing equatorial currents, and hence an ideal site for exploring the forcing-response pattern of the ocean-atmosphere as a coupled system. For example, the anomalous ocean-atmosphere coupled phenomena like Indian Ocean Dipole mode produces anomalous atmospheric and oceanic condition that influence regional climate.



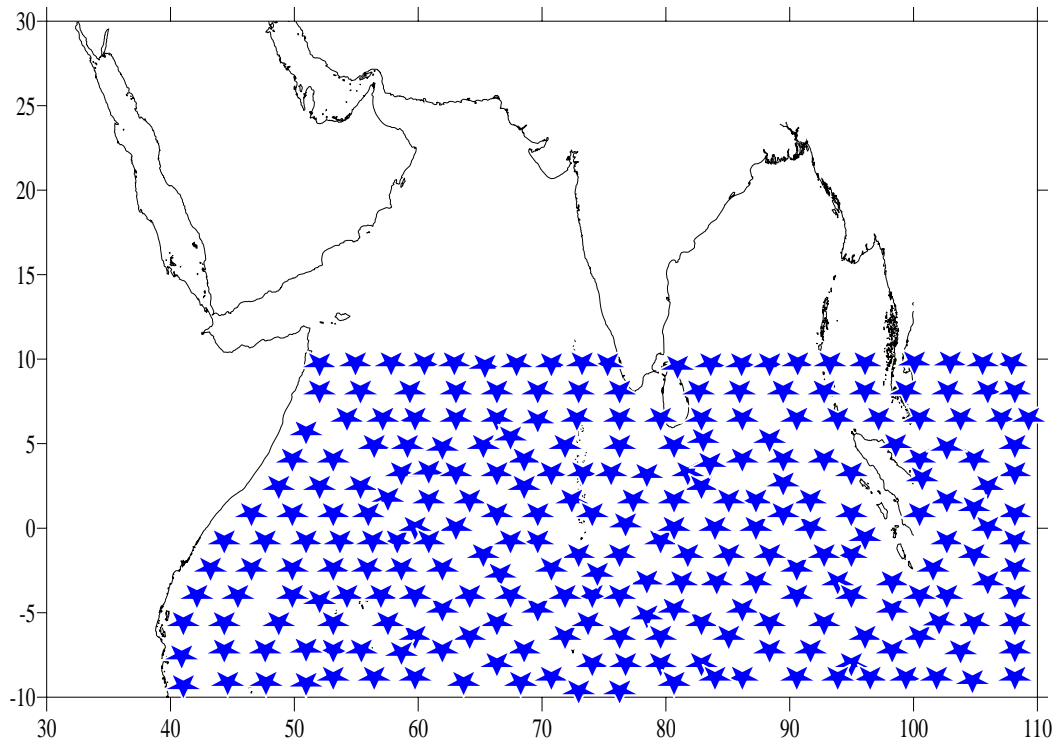


Fig.1 Map showing the area of study.

## 1.4 Previous Work

Despite the importance of the Indian Ocean in the regional and global climate system, it is the most poorly sampled and hence least studied region of the three tropical Oceans. This section provides an over view of our present understanding of the EIO emanating from the review of previous research work.

The unique boundary conditions make the Indian Ocean interesting to study in its own right; for climate prediction however the attention necessarily focuses on the SST. In the tropics, SST anomalies play a crucial role in the evolution of the atmospheric events. In turn these SST anomalies are driven by the processes responsible for the heat budget and

thickness of the mixed layer (energy fluxes through the Sea surface, horizontal and vertical advection, horizontal and vertical turbulence) [Rao *et al.*, 1989]. Most of the observed SST variance in the northern Indian Ocean is due to heat fluxes [Klein *et al.*, 1999; Rao and Siva Kumar, 2000], while Ocean dynamics contribution is substantial over the southern Indian Ocean, particularly in the neighborhood of the equatorial zone [Murtugudde *et al.*, 2000; Xie *et al.*, 2002; Huang and Kinter, 2002].

An adequate description of the space time variability of the SST and mixed layer depth in the equatorial Indian Ocean and the processes which determine this variability would provide crucial information about the dynamics and importance of air-Sea interactions. There exist several SST climatologies for the Indian Ocean. Hastenrath and Lamb [1979] and Reynolds [1983], for instance, constructed mean monthly SST climatologies for the basin. The Hastenrath and Lamb [1979] climatology was generated from 60 years of surface marine observations. Reynolds [1983], in turn used a 122 year record to generate a global SST climatology. Levitus [1982] produced climatology of the subsurface temperature and salinity structure for the entire Indian Ocean as part of a global climatology.

Rao *et al.*, [1989] generated mean monthly mixed layer depth (MLD), SST and surface current climatologies for the tropical Indian Ocean. In addition meteorological climatologies were produced for those variables, which could influence the evolution of the MLD and SST fields. They found that largest amplitude in the annual harmonic of MLD was in the southern tropical Indian Ocean, the extreme northern Arabian Sea, the central Arabian Sea and the western Bay of Bengal. Largest amplitude in the annual harmonic for SST was observed in the southern tropical Indian

Ocean, in the extreme northern Arabian Sea and Bay of Bengal. Maximum in the annual harmonic of the surface heat flux distribution were observed in the southern tropical Indian Ocean and northern Arabian Sea. They also found that surface fluxes could account for 75% of the variance in the SST and MLD time series over most of the region south of the equator. Thus, through the direct effects of surface heating on mixed layer temperature and through convective effects on MLD, surface fluxes could play an important role in the mixed layer dynamics over a considerable portion of the Indian Ocean. Large correlations between wind stress and MLD were found in the southern tropical Indian Ocean and the central Arabian Sea. In these regions, wind stirring could be an important factor in driving MLD variability. Surface currents were most strongly correlated with MLD in the central Arabian Sea, in the vicinity of the south equatorial current and in the extreme eastern equatorial Indian Ocean.

McPhaden [1982] examined heat and turbulent energy balances in the central equatorial Indian Ocean using over two years of simultaneous oceanic and atmospheric measurements from the Island of Gan. McPhaden found that zonally varying SST pattern was two orders of magnitude larger in the equatorial Oceans than at the mid latitudes and was comparable in both magnitude and spatial structure to the wind driven equatorial circulation. This strong dynamical effect is due to sensitivity of geostrophic currents to small changes in horizontal thermal gradients at low latitude. SST was used as an indicator of subsurface processes where in a strong correlation was found between dynamically controlled changes in thermocline depth and SST. The physical basis for the correspondence is that when cold thermocline water is carried closer to (further from) the surface, it is easier (harder) to mix across the base of

the mixed layer. This in turn leads to colder (warmer) SST. Most of the variability in mixed layer temperature was due to variability in surface heat flux. Horizontal advection was of secondary importance and that entrainment, as determined from relative changes in mixed layer and thermocline depths, was active on only a few occasions.

Jochum and Murtugudde [2005] studied the internal variability of the Indian Ocean SST. Internal oceanic variability was caused by instabilities of the wind driven currents. They showed that two conditions must be met for a mesoscale eddy field to cause inter-annual SST variability and introduce atmospheric variability. Firstly, eddies must persist long enough so that they can change the oceanic conditions for the next season where the currents become unstable. The nonlinearities of the instability mechanism can then amplify the small changes in the new initial condition. Second, because oceanic eddy scales were much smaller than the atmospheric Rossby radius, eddies must modify the ocean-atmosphere heat exchange, thereby affecting the total heat in the mixed layer.

SST is the result not only of internal and atmospherically forced variability, but it also reflects positive feedback between the ocean and atmosphere. In principle even an infinitesimally small disturbance could trigger the rapid growth of anomalies in the coupled ocean-atmosphere system. Since the seasonal cycle in the Indian Ocean is fairly stable and is dominated by the monsoon the interannual variability in the Indian Ocean has to be mostly the result of external atmospheric forcing and internal oceanic variability [Jochum and Murtugudde, 2005]. In most part of the Indian Ocean, the internal variability of SST appears to be negligible, compared to the seasonal or observed interannual variability. However, in the western Indian Ocean, the internal variability explains a significant

part of the observed SST variability. Large internal variability in the western Indian Ocean arises due to the effect of mesoscale variability which cannot be removed by simply averaging over the eddy time scale. The eddies make a net contribution to the mixed layer heat budget; because the generating instability processes are nonlinear, thus the contribution will vary and the SST will be different from year to year, even under climatological forcing [Jochum and Murtugudde, 2005].

Though the large internal SST variability is restricted to the western Indian Ocean, it can project directly on to the zonal SST gradient and change its seasonal cycle. This can have implication for the onset and development of the IODZM. It can also affect the amount of moisture that is picked up by the Findlater Jet and delivered to the Indian subcontinent during the southwest monsoon. During the times of strong eddy activity the Findlater Jet picks up less moisture which can have implications of the strength of monsoon rains over the India. Rodwell and Hoskins [1994] demonstrated that the vertical structure of atmospheric heating over the western Indian Ocean and the horn of Africa determines the latitude at which Findlater Jet turns east in the northern hemisphere. Thus, western Indian Ocean mesoscale variability may be an important component in the irregularity of the Indian monsoon rainfall [Jochum and Murtugudde, 2005].

Murtugudde and Busalacchi [1999] used a reduced gravity, primitive equation, sigma coordinate OGCM coupled to an advective atmospheric mixed layer model to study the seasonal and interannual variability of the tropical Indian Ocean. The seasonal cycle of SST along the equator showed eastward phase propagation with larger variability in the east which was opposite to what was observed in the equatorial Pacific. The

barrier layer variability was large in the eastern equatorial Indian Ocean where rainfall variability was large and also in the zonal band between  $10^{\circ}$  and  $20^{\circ}$  S. Analysis of Seasonal heat budgets for the mixed layer showed that the western south tropical Indian Ocean (STIO) had a large seasonal cycle of SST and mixed layer because the thermocline was close to the surface due to the Ekman pumping. The seasonal cycle in the eastern STIO is slightly smaller due to a deeper thermocline. However the interannual SST anomalies in the western and eastern south tropical Indian Ocean tend to be of opposite sign. Anderson and Carrington [1993] concluded that the wind driven variations in SST were not a good indicator of interannual SST variability in the Indian Ocean. The variability of SST anomalies in the Arabian Sea, the Somali current and the south tropical Indian Ocean depend on surface heat fluxes as well as wind forcing. The Bay of Bengal and the eastern STIO were significantly affected by anomalies in the solar radiation and cloudiness.

One major factor in the variability of the southern IO is the introduction of Pacific waters through the Indonesian through flow (ITF). Murtugudde *et al.*, [1998] found that the spreading of the thermocline by the ITF reduced the effect of upwelling on SST variability off Java. ITF removes mass and heat from the western Pacific warm pool and affects the thermohaline circulation and air-Sea heat exchange pattern of the global Ocean [Gordon, 1986; Broecker, 1991; Hirst and Godfrey, 1993; Godfrey, 1996; Schneider and Barnett, 1997; Schiller *et al.*, 1998]. The estimated upper ocean through flow volume transport was found to be 5-10Sv ( $\text{Sv} = 10^6 \text{m}^3/\text{s}$ ) with an annual variability of about 5Sv. Maximum flow into the IO occurs during the southwest monsoon from July to September [Meyers *et al.*, 1995; Potemra, 1999]. Tomczak and Godfrey [1994] indicated that the IO circulation was not only forced by intense

annually reversing monsoon winds but also influenced by the through flow variability.

Rao and Sivakumar [2000] used a subset of the global ocean temperature climatology to characterize the observed seasonal variability in the near surface thermal structure of the tropical IO. In the near surface isothermal layer the seasonal variability was least in the warm pool region and increased poleward. Over much of the tropical IO, local surface heat fluxes overwhelm horizontal advection in the seasonal evolution of the mixed layer temperature. Entrainment cooling was weaker by an order of magnitude than the other two processes. Several dynamical processes produce the most prominent signals in the thermocline in different geographic regions, such as coastal upwelling/downwelling with associated reversals in the flow of Arabia, off south west India, and off the east coast of India, Ekman driven thermocline deepening in the central Arabian Sea, convergence of waters caused by equatorial jets in the eastern EIO, Ekman divergence of a dome of cold waters just south of the equator in the west, propagating Kelvin waves in the coastal regions of the Bay of Bengal and propagating Rossby waves from off south west India to Somalia and in the Indo Pacific through flow region. The seasonal variability of the near surface thermal structure clearly shows two distinct regimes: - the first in the topmost 50-75m layer, which is nearly isothermal where thermodynamic forcing is important, and second is below this isothermal layer where several dynamical forcings are important.

Atmospheric variability in the tropical Indian Ocean has two dominant intraseasonal modes with 30-60 day and 10-20 day (or quasi-biweekly) period [Yasunari, 1981; Krishnamurti and Ardunay, 1980; Krishnamurti

*et al.*, 1988; Goswami *et al.*, 1998]. The 30-60 day eastward propagating Madden-Julian oscillation is the dominant mode of intraseasonal variability [Madden and Julian, 1972 & 1994] in the equatorial region. The 30-60 day mode, which appear to propagate northward in summer [Sikka and Gadgil, 1980], and a westward propagating quasi-biweekly mode (QBM) largely determine the active-break cycle of the summer monsoon over the Bay of Bengal [Krishnamurti and Arduway, 1980].

Observed currents in the equatorial Indian Ocean have consistently shown intraseasonal variability with periods of a few days to 60 days [Schott and McCreary, 2001]. A prominent 26 day oscillation of meridional current in the western EIO [Luyten and Roemmich, 1982] is due to mixed Rossby-gravity (MRG) waves with zonal wavelength of 1100-2000 km [Reverdin and Luyten, 1986; Tsai *et al.*, 1992]. Model studies suggest that the 26-day MRG wave is generated by dynamic instability of seasonal currents [Kindle and Thompson, 1989]. The 1973-1975 weekly record from Gan Island (73°E) [Knox, 1976] showed dominant 30-60 day variability of equatorial zonal current, and suggested the presence of variability with periods shorter than 20 days [McPhaden, 1982].

Hsiung *et al.* [1989] found a southward oceanic heat transport in boreal summer and northward transport in boreal winter (ie, a heat transport always toward the winter hemisphere enhanced during boreal summer). Ekman transport which carries the warmest temperature of the water column and which reverses to the northwest during the northeast monsoon can play a decisive role in reversing the sign of the net heat transport at that season, at least north of 10°S, where the Indian Ocean is most influenced by the monsoon [Levitus, 1987].



Lee and Marotzke [1998] studied the seasonal cycles of meridional overturning and heat transport of the Indian Ocean. Meridional overturning displayed large seasonal variation; the largest variations occur near  $10^{\circ}\text{S}$  and  $10^{\circ}\text{N}$  which corresponds to the latitudes where the easterlies over the southern Indian Ocean and the monsoon over the northern Indian Ocean have the largest seasonal variability. The meridional transport stream function was decomposed into three components to highlight the relative importance of various dynamical processes in causing the seasonal cycles: the external mode plus zonally varying topography, the Ekman flow plus a barotropic compensation and vertically sheared flow comprising the thermal wind and ageostrophic flow associated with friction and nonlinear effects. Overall the Ekman component causes dominant seasonal variations in meridional overturning and heat transport due to monsoonal reversal over the subtropical southern Indian Ocean. They found that the northern Indian Ocean as a whole was more adiabatic as compared with the very southern part of the Indian Ocean.

Hastenrath and Greischar [1993] evaluated the heat budget of the combined hydrosphere-atmosphere system in the Indian Ocean sector ( $30^{\circ}\text{N}$ - $30^{\circ}\text{S}$ ,  $30^{\circ}\text{E}$ - $120^{\circ}\text{E}$ ). The net radiation at the top of the atmosphere represents the energy input to the combined Ocean-atmosphere system. During the boreal winter semester the net radiation heat input to the system increased from the north toward the equatorial region and the southern Indian Ocean, while during boreal summer it diminished from the northern portion of the basin southward. During the boreal winter half year, net Oceanic heat gain prevailed through most of the basin including the equatorial and southern tropical Indian Ocean. Positive heat storage

was indicated for most of the northern portion of the basin during boreal winter. The pattern of Oceanic heat transport is approximately opposite to that of heat storage, with import indicated for much of the northern portion of the basin and export from the south tropical Indian Ocean. During the boreal summer net oceanic heat gain was prevailingly positive to the north and negative to the south of the equator.

## **1.5 Present Work**

### **1.5.1 Motivation**

Equatorial regions are special areas of the world ocean where intense air-sea interaction takes place and the ocean and atmosphere is tightly coupled. Equatorial Indian Ocean, in spite of its very special characteristics compared to equatorial Pacific or Atlantic, is the least studied region. This is primarily due to the scarcity of observation. With the advent of ocean remote sensing technique, the availability of high resolution data, both space and time, makes it now possible to address several aspects of Indian Ocean. In addition to this, the deployment of ARGO profiling floats in the Indian Ocean dramatically increased the vertical profiles of temperature and salinity. This allows one to address the variability of EIO on a seasonal scale.

### **1.5.2 Objectives**

The present work aims at understanding the upper ocean variability of the EIO on a seasonal scale and then to explore the atmospheric forcing responsible for it. The specific objectives are:

1. Seasonal variability of sea surface temperature, sea surface salinity, mixed layer depth, barrier layer depth and depth of mid-thermocline.
2. Seasonal variability of net heat flux, fresh water flux, and momentum flux.
3. What controls the mixed layer depth and barrier layer depth in the EIO?

# **Chapter 2**

## **Data and Methods**

## **2.1 Introduction**

In order to find the seasonal cycle of the upper ocean variability and the air-sea interaction responsible for it, the study uses water column (hydrographic) data such as temperature and salinity profiles, ocean surface currents and the atmospheric data such air temperature, wind speed and direction, etc. were used from various sources. In order to decipher the upper ocean variability it is important to determine the mixed layer depth, barrier layer depth as well as the mid-thermocline depth. Variation in these parameters indicates effect of atmospheric forcing. Hence it is appropriate to define them.

### **2.1.1 Mixed-layer**

The mixed-layer is the upper layer of the ocean within which all the physical properties of water such as temperature, salinity and density remains almost the same (see Fig.2). The depth of this layer usually ranges between 25 and 200m in the tropical region. The mixed-layer owes its existence to the mixing initiated by waves and turbulence caused by the wind stress on the sea surface. An effect of mixing is to make both the properties of water, temperature and salinity, and hence the density, more uniform. The penetration of mixing to a certain depth (the mixed-layer depth) depends on the stability of the seawater. Seawater stability in the near surface is determined by the atmospheric fluxes through the ocean surface (momentum, heat and fresh water). A typical unstable configuration is when water is denser (“heavier”) at the surface than below. The mixing that ensues, for example with some impulse from

waves or turbulence, renders the density more uniform and deepens the mixed-layer.

In many situations, the mixed-layer can be identified with the layer of mixed temperature, when the salinity does not vary much with increasing depth. The mixed-layer is the oceanic surface zone that responds most quickly and directly to atmospheric fluxes, and it is through the mixed-layer that such influence is transmitted to the whole ocean in the long term. Conversely, the mixed-layer is the part of the ocean through which the ocean influences directly to the atmosphere. Many important processes occur within the mixed-layer, whether physical (e.g. direct wind-forcing of the ocean circulation), chemical (e.g. dissolution of incoming CO<sub>2</sub> from the atmosphere), or biological (e.g. phytoplankton production).

### **2.1.2 Barrier layer**

Barrier layer is the layer between the base of the mixed layer and top of the thermocline (Fig.2). In the tropics where heavy precipitation takes place, the surface-trapped freshwater pool forms a very shallow mixed layer within a deeper nearly isothermal layer. The region between the shallower (density defined) well-mixed layer and the deeper isothermal layer within which salinity changes drastically with depth, is referred to as a salinity-stratified barrier layer. The barrier layer may have important implications on the heat balance within the surface layer because, as the name suggests, it effectively limits communication between the ocean mixed layer and the deeper permanent thermocline. Even if under light wind conditions water is entrained from below into the mixed layer, it

will have the same temperature as the water in this upper layer. Thus, there is no heat flux through the bottom of the mixed layer and other sinks must come into play to balance the solar warming that is confined to the surface.

### **2.1.3 Mid-Thermocline depth**

Thermocline depth is the depth at which the rate of decrease of temperature with increase of depth is the largest. In general the sea water temperature decreases from the surface to the deepest levels, except in high latitudes where the configuration can be more complex. There exists in most ocean areas (apart from polar and sub-polar oceans) a zone where the rate of decrease of temperature is much larger compared with that above and below, hence the definition. Depending on the geographical location, the thermocline depth ranges from about 50m to 1000m. A simplified view is to consider the thermocline as the separation zone between the mixed layer above, much influenced by atmospheric fluxes, and the deep ocean. In the tropical region the mid-thermocline depth is used as an indicator to characterize the thermocline oscillations and variability. In the EIO, the equatorial under current is situated in the thermocline and hence assumes importance. In the tropics, 20°C isotherm is usually located in the mid-thermocline region and hence this is used to study the thermocline variability.

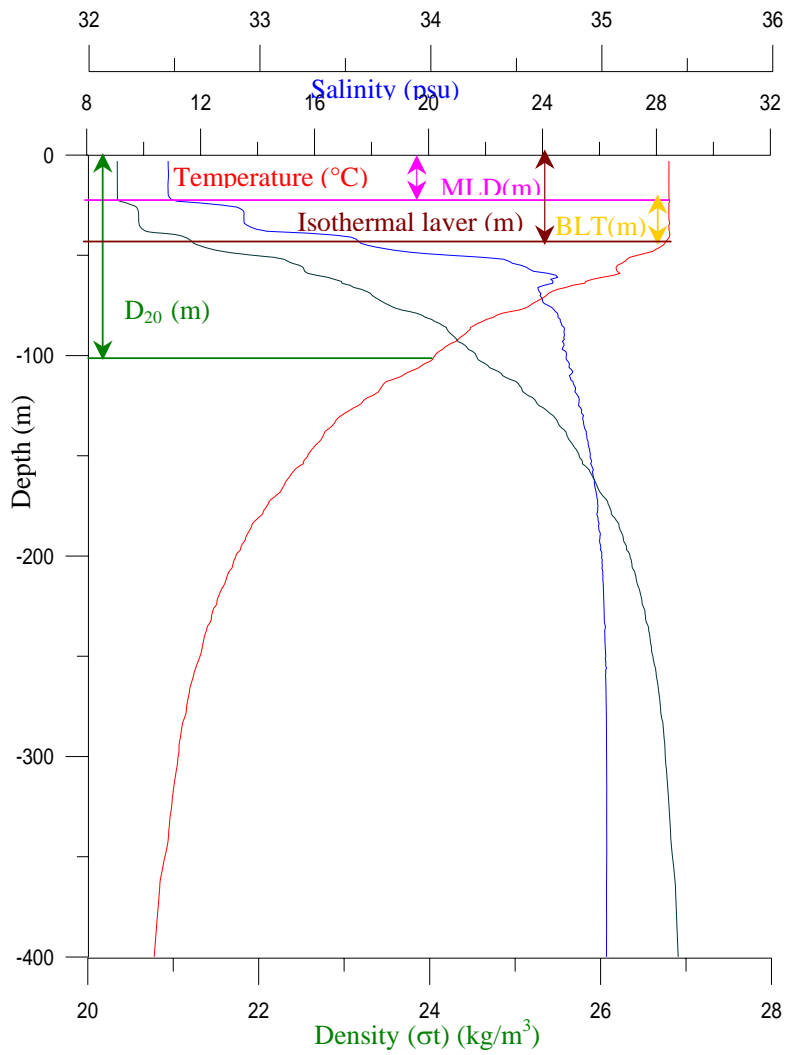


Fig.2 Schematics showing the vertical profiles of temperature (red), salinity (blue), sigma-t (green) and the MLD, BLT, isothermal layer and the  $D_{20}$ .



## **2.2 Data**

### **2.2.1 Oceanic data**

The oceanographic data on temperature, salinity and surface currents were used for the present study.

The study uses both *in situ* data and remote sensing data

1. *In situ* hydrographic data – Vertical profiles of temperature and salinity
2. Remote sensing data – Ocean surface current

#### **2.2.1.1 Hydrographic data**

The hydrographic data used for the study were mainly extracted from three sources:

1. World Ocean Database 2005 (WOD05) [Boyer *et al.*, 2006; Johnson *et al.*, 2006], which contains temperature and salinity data from conductivity-temperature-depth (CTD) cast during the period 1970-2000 [<http://www.nodc.noaa.gov/OC5/indprod.html>].
2. Responsible National Oceanographic Data Center (RNODC), Goa which contains temperature and salinity data from conductivity-temperature-depth (CTD) casts for the period 1983-2004, collected by the Indian research vessels.
3. ARGO data which contains temperature and salinity profiles during 2000 to 2006 were used for the present study [<http://www.usgodae.org>]. Argo is a global array of 3,000 free-drifting profiling floats that measures the temperature and salinity of the upper 2000 m of the ocean. This will allow continuous monitoring of the climate state of the ocean, with all data being relayed and made publicly available within hours after

collection. Once deployed, each Argo float descends to as deep as 2000 meters where it drifts with the currents. After a typical period of 10 days, it slowly rises to the surface measuring temperature and salinity profiles. At the surface, it relays this information to satellites for immediate availability via the Global Telecommunication System (GTS) and on the Internet after quality checks. It then sinks to begin another cycle. The expected life of an Argo float is about four years. Deployments began in 2000. Presently there are 450 Argo floats profiling temperature and salinity in the Indian Ocean.

### **2.2.1.2 Ocean surface current data**

The monthly mean ocean surface current (Ocean Surface Current Analysis- Real time - OSCAR) data during 1992 to 2006 was used [<http://www.oscar.noaa.gov/datadisplay>] to generate monthly climatology of the surface currents. OSCAR is near-real time ocean surface current derived from satellite altimeter and scatterometer data. It is a pilot processing system being developed to provide operational ocean surface velocity fields computed from sea surface height and vector wind data. Surface currents consist of a geostrophic component, which can be computed from the altimeter heights, and a wind-driven component, computed from wind vectors derived from satellite scatterometers. OSCAR is based on a hybrid geostrophic-Ekman scheme that is continuous across the equatorial latitudes.

### **2.2.2 Atmospheric data**

Atmospheric data on air temperature, wind speed and direction, net heat flux, wind stress, and fresh water flux used for this study was derived

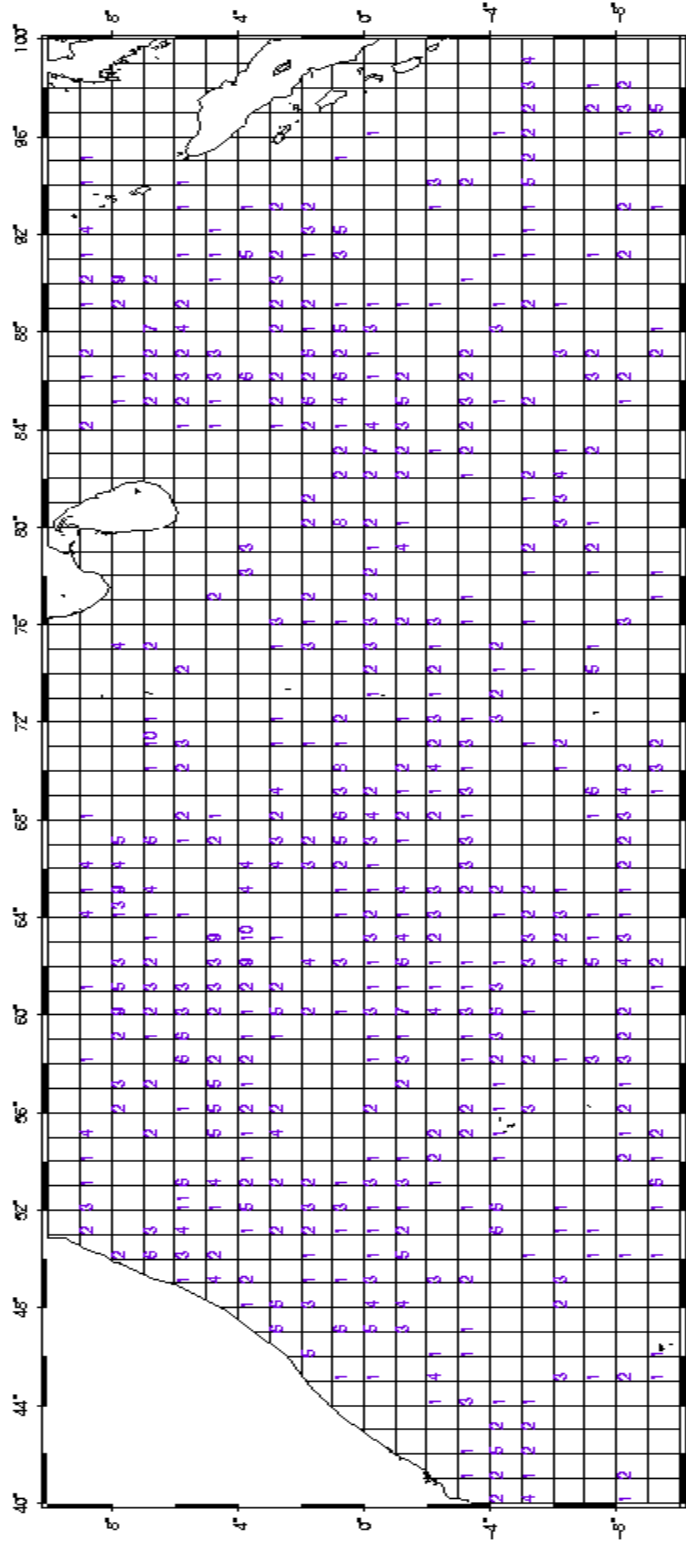
from Southampton Oceanography Center [Josey *et al.*, 1998] [<http://www.noc.soton.ac.uk/ooc/CLIMATOLOGY/index.php>] data. Global monthly mean climatology of meteorological parameters (10m air temperature, 10m wind speed, 10m humidity) and air-Sea fluxes of heat, momentum and freshwater have been calculated from a dataset of marine meteorological reports spanning the period 1980 - 1993, which has been corrected for biases arising from variations in observing procedure. The dataset is a modified version of the Comprehensive Ocean - Atmosphere Dataset (COADS).

## **2.3 Method**

### **2.3.1 Hydrographic data analysis**

The hydrographic data on temperature and salinity were subjected to the following quality control procedures to obtain quality data. First, duplicate profiles, as well as those with obvious errors, were excluded by visual inspection. Then, profiles with depths less than 50m were eliminated. Then the quality-controlled data was binned into a 1-degree longitude by 1-degree latitude grid ( $1^{\circ} \times 1^{\circ}$ ) within the study domain. These data were further used to calculate the density values. From each of this quality controlled profiles SST and sea surface salinity (SSS) were determined in each  $1^{\circ} \times 1^{\circ}$  grid. From these values monthly mean SST and SSS were calculated for each of the  $1^{\circ} \times 1^{\circ}$  grid.

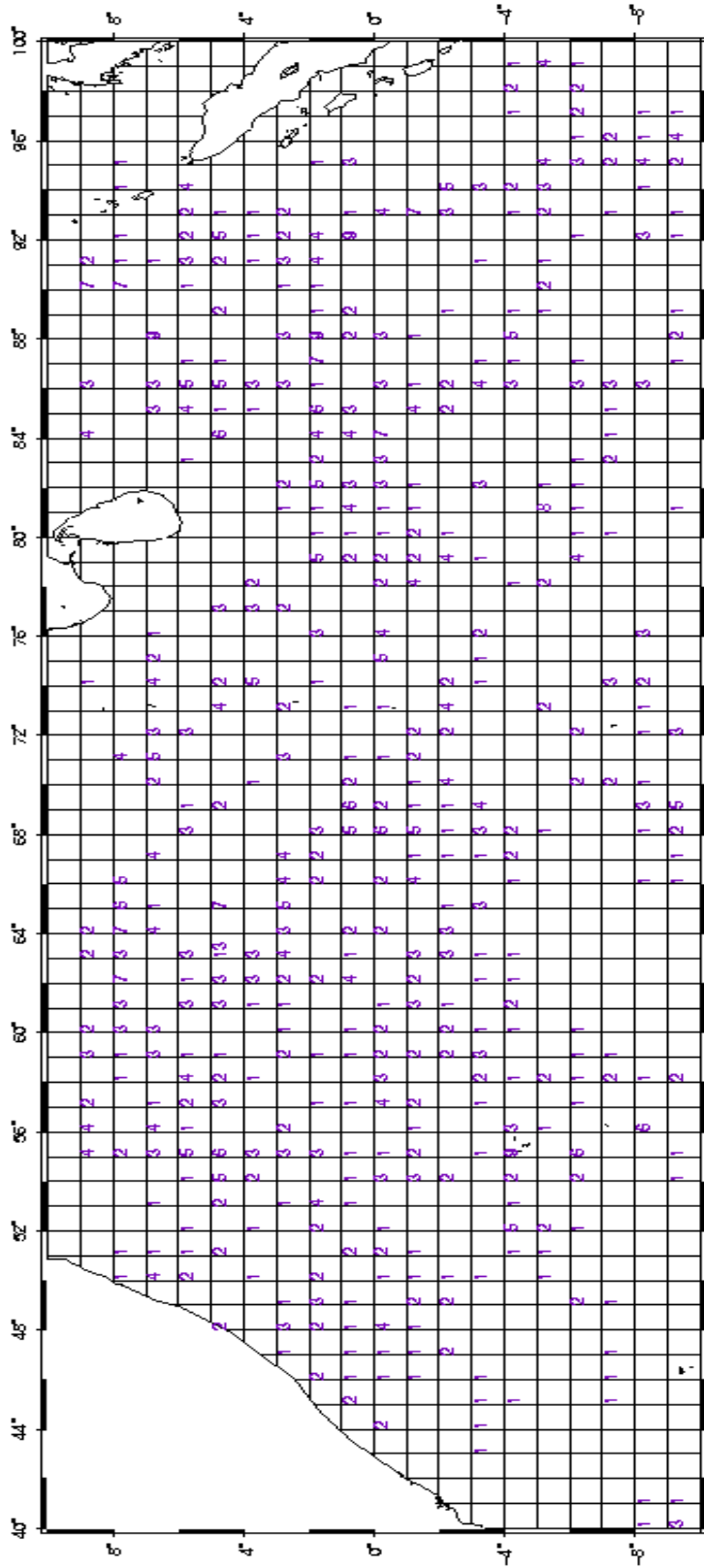
Month: JANUARY  
 Duration of Data Collected: 1-Jan-1975 / 30-Dec-2006



No. of Profiles: 1202

Fig.3 Total number of temperature and salinity profile (1202) obtained from CTD and ARGO in each of the 1°x1° grid for the month of January

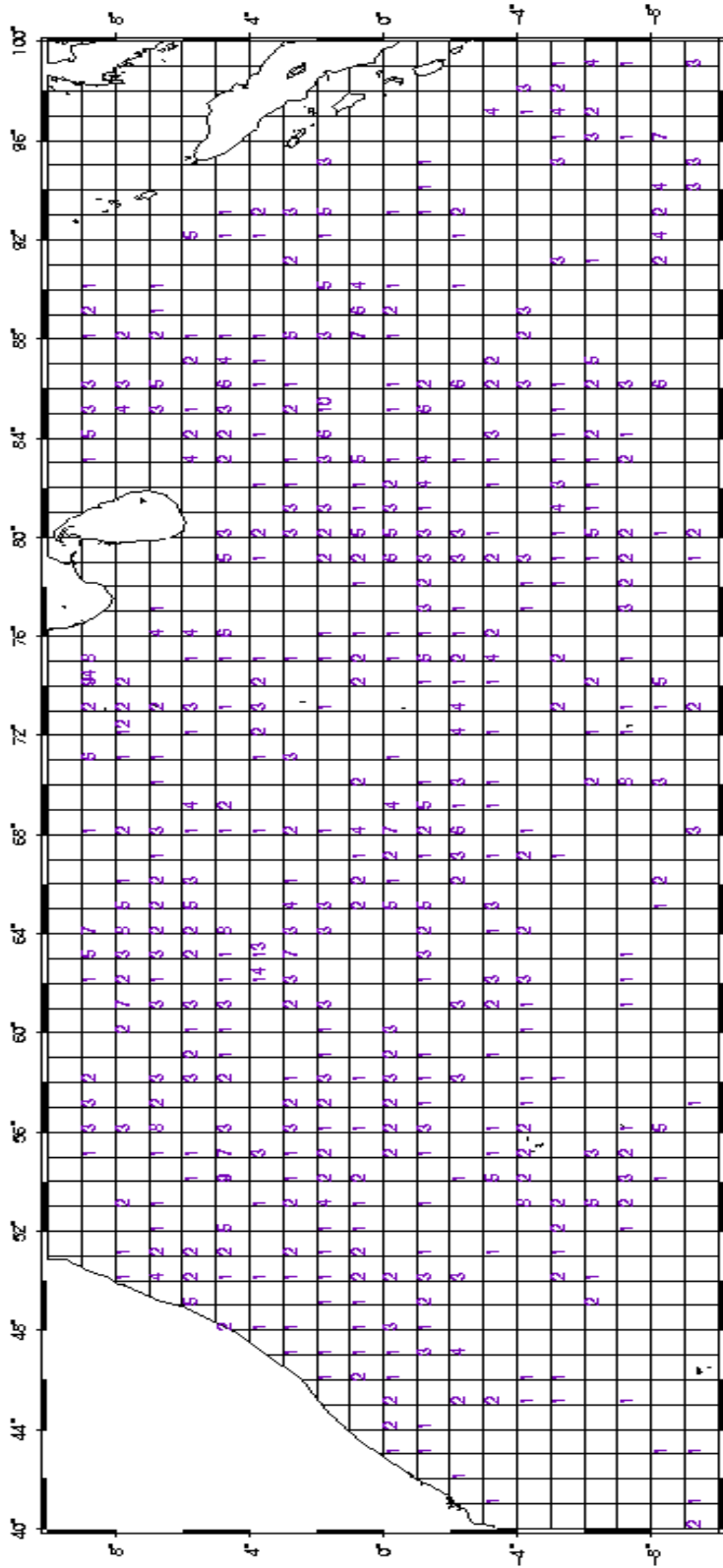
Month: FEBRUARY  
 Duration of Data Collected: 1-Jan-1975 / 30-Dec-2006



No. of Profiles: 1033

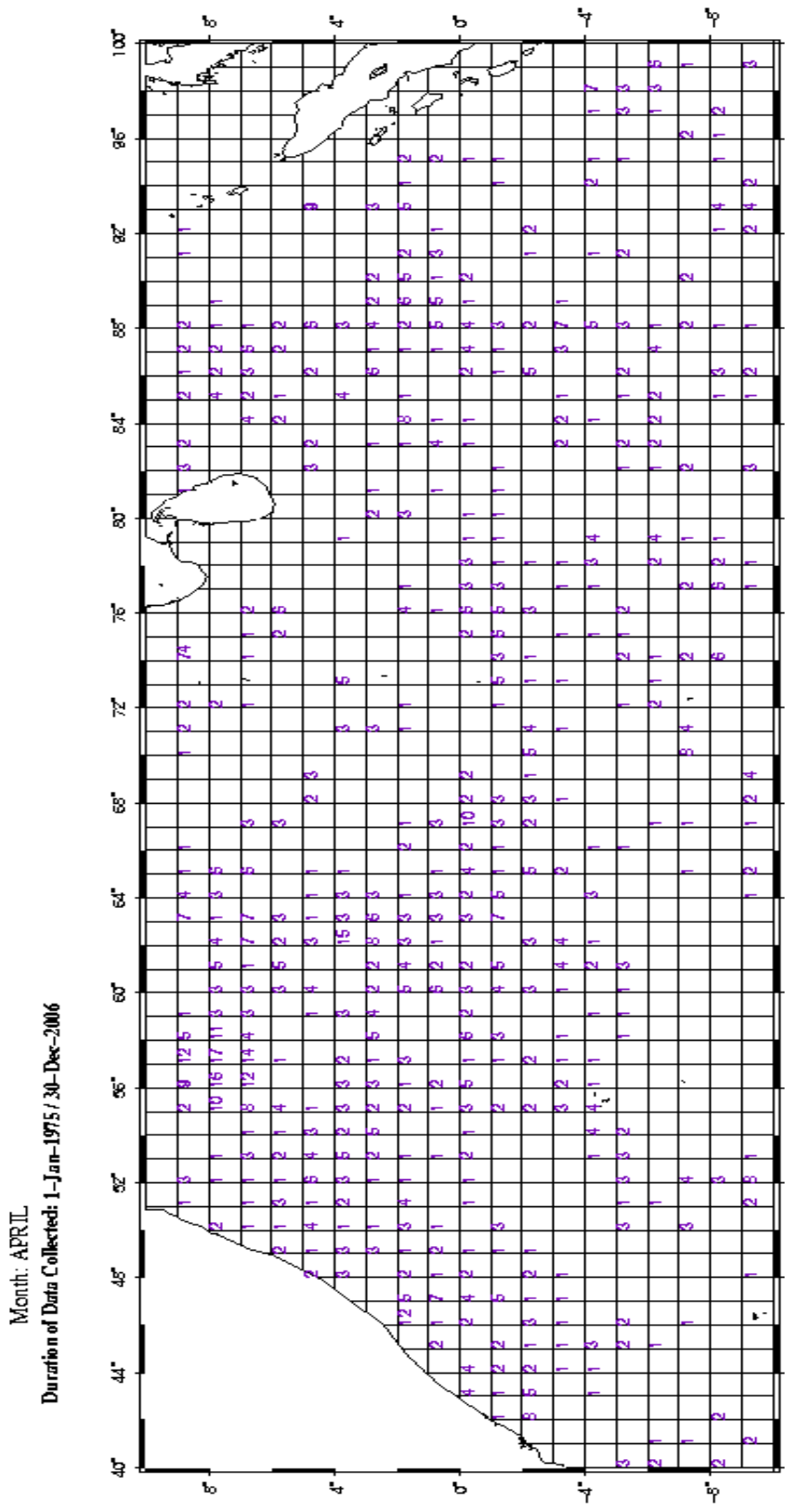
Fig.4 Total number of temperature and salinity profile (1033) obtained from CTD and ARGO in each of the 1°×1° grid for the month of February

Month: MARCH  
 Duration of Data Collected: 1-Jan-1975 / 30-Dec-2006



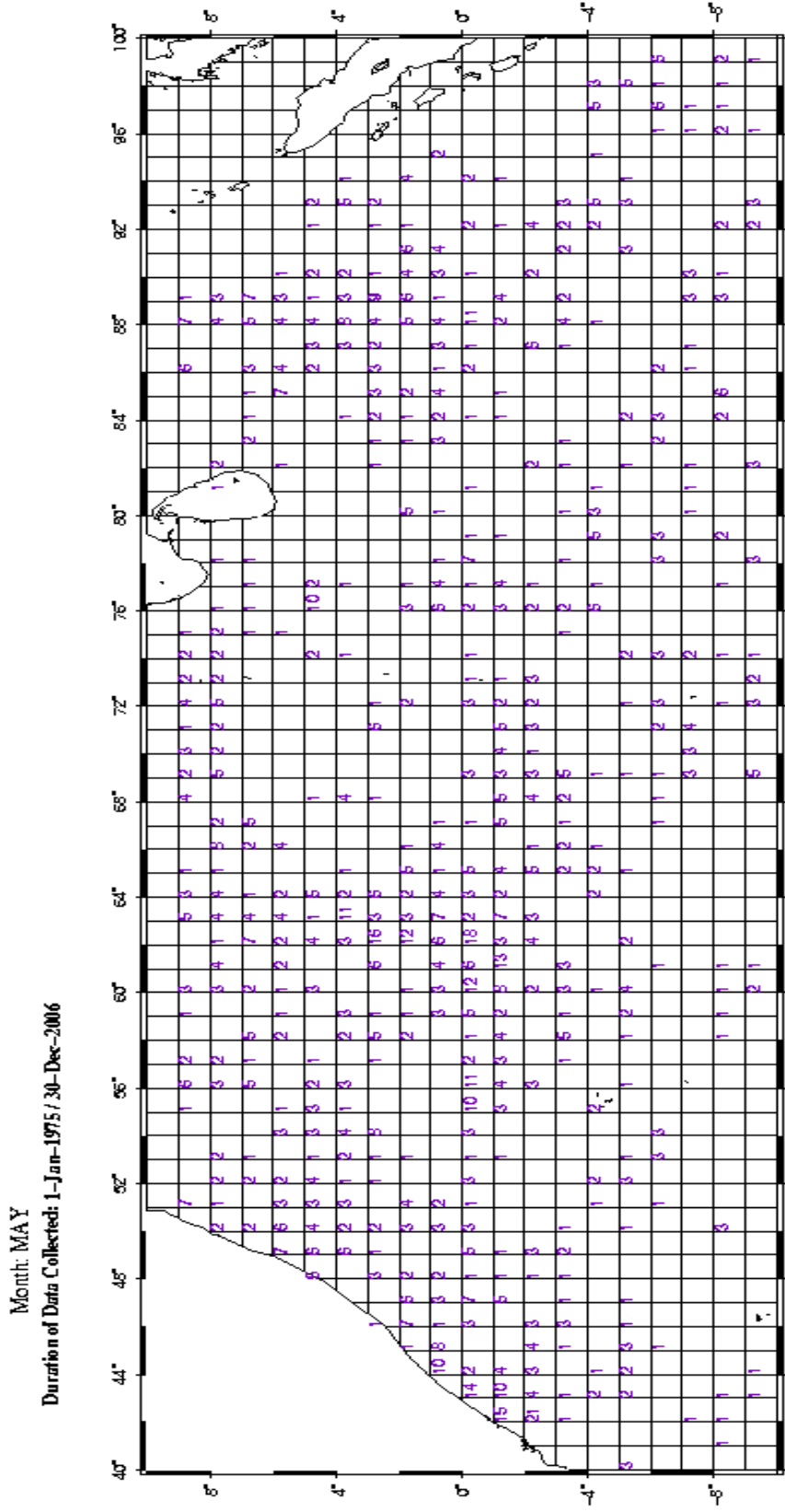
No. of Profiles: 1220

Fig.5 Total number of temperature and salinity profile (1220) obtained from CTD and ARGO in each of the 1°×1° grid for the month of March



No. of Profiles: 1334

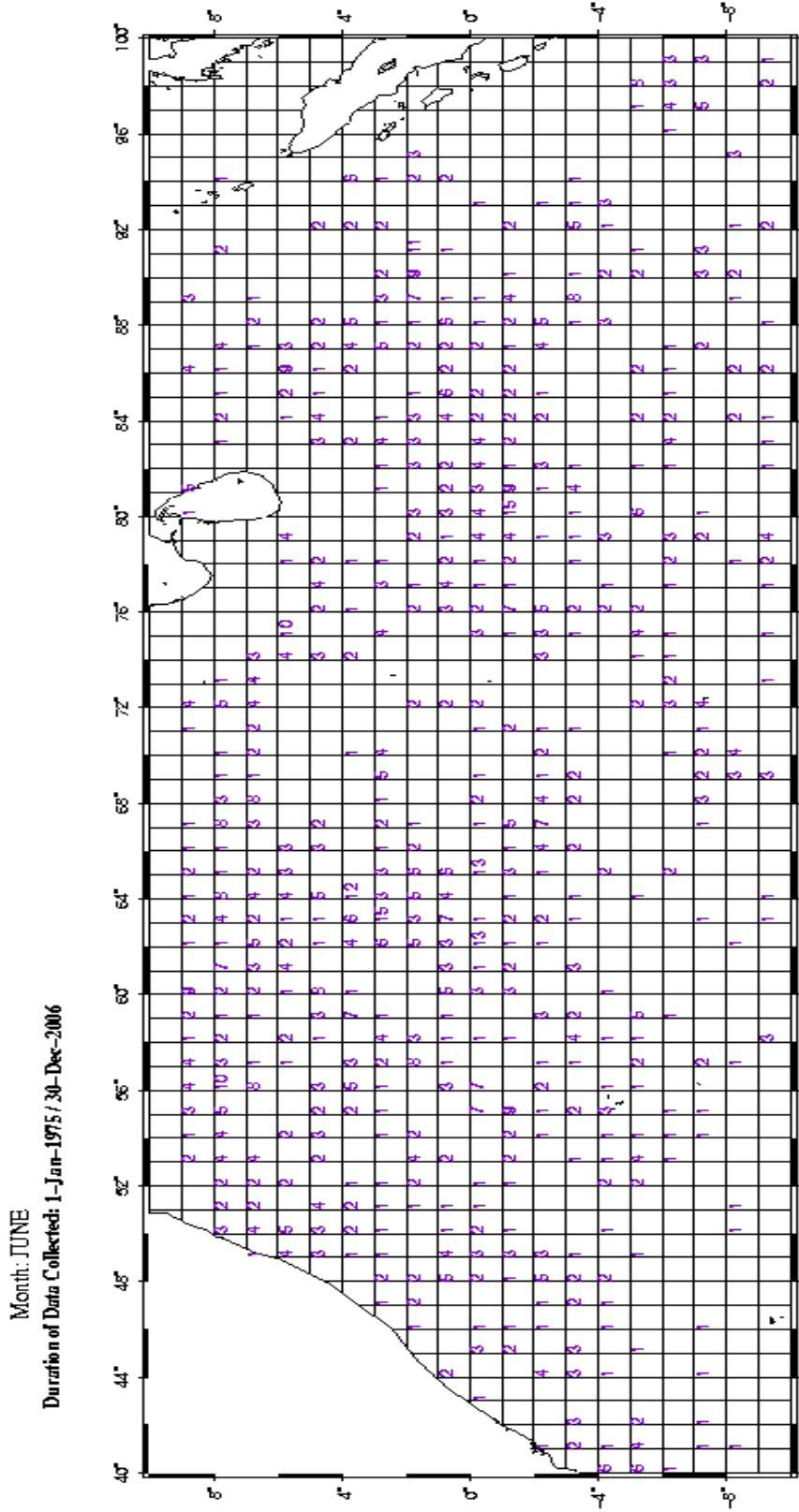
Fig.6 Total number of temperature and salinity profile (1334) obtained from CTD and ARGO in each of the 1°×1° grid for the month of April



No. of Profiles: 1414

Fig.7 Total number of temperature and salinity profile (1414) obtained from CTD and ARGO in each of the 1°x1° grid for the month of May





No. of Profiles: 1336

Fig.8 Total number of temperature and salinity profile (1336) obtained from CTD and ARGO in each of the 1°×1° grid for the month of June.

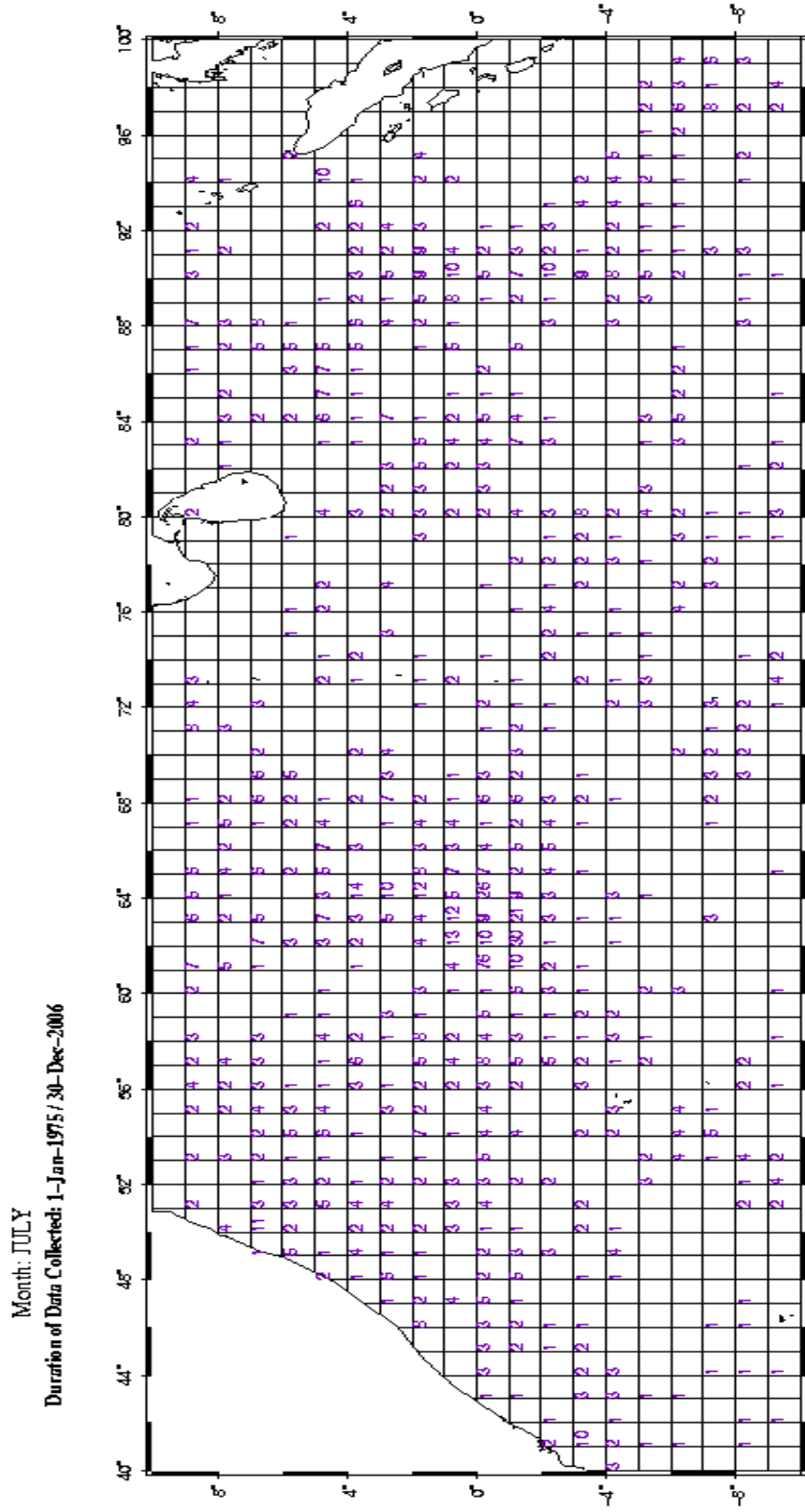
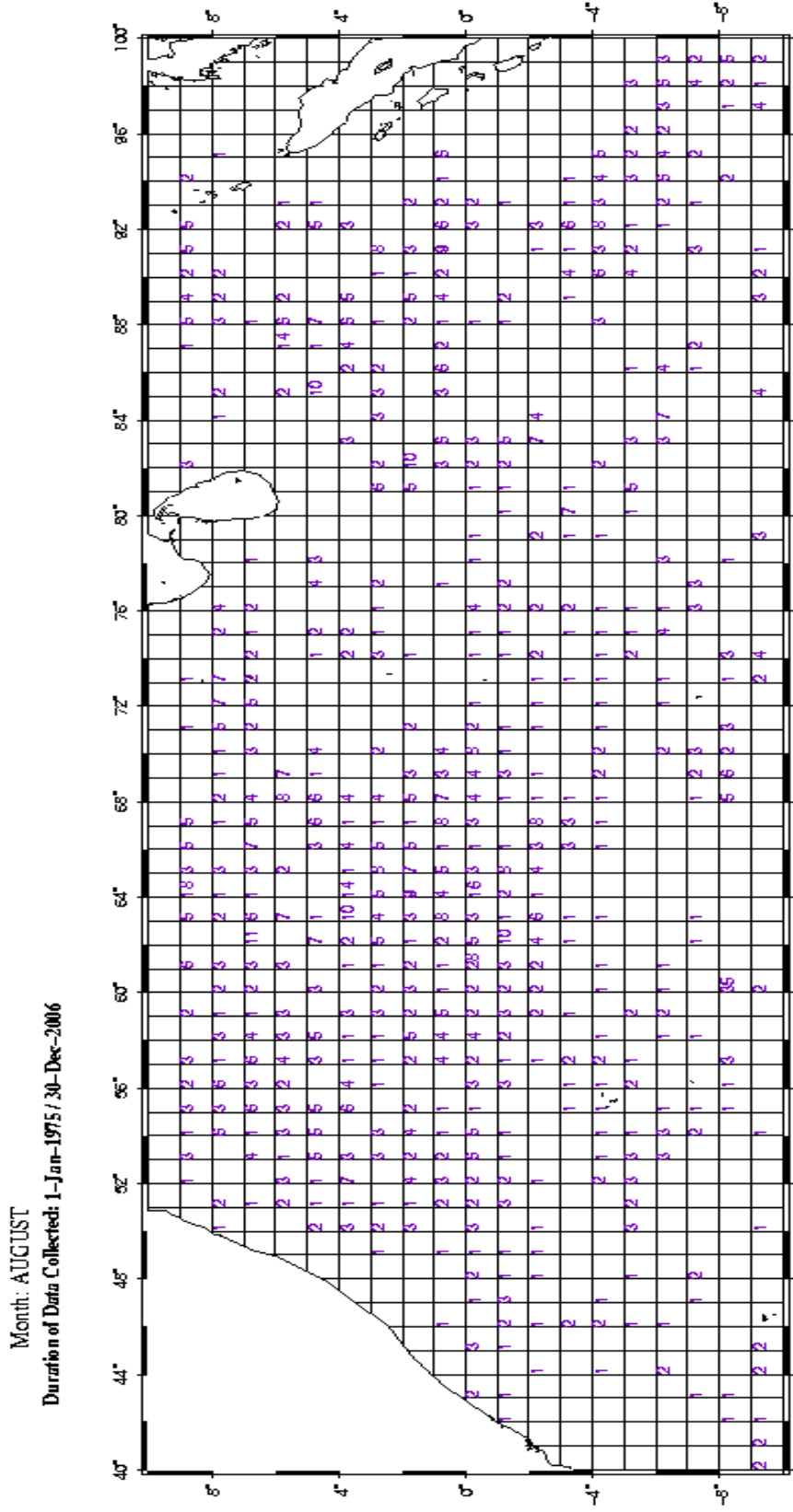


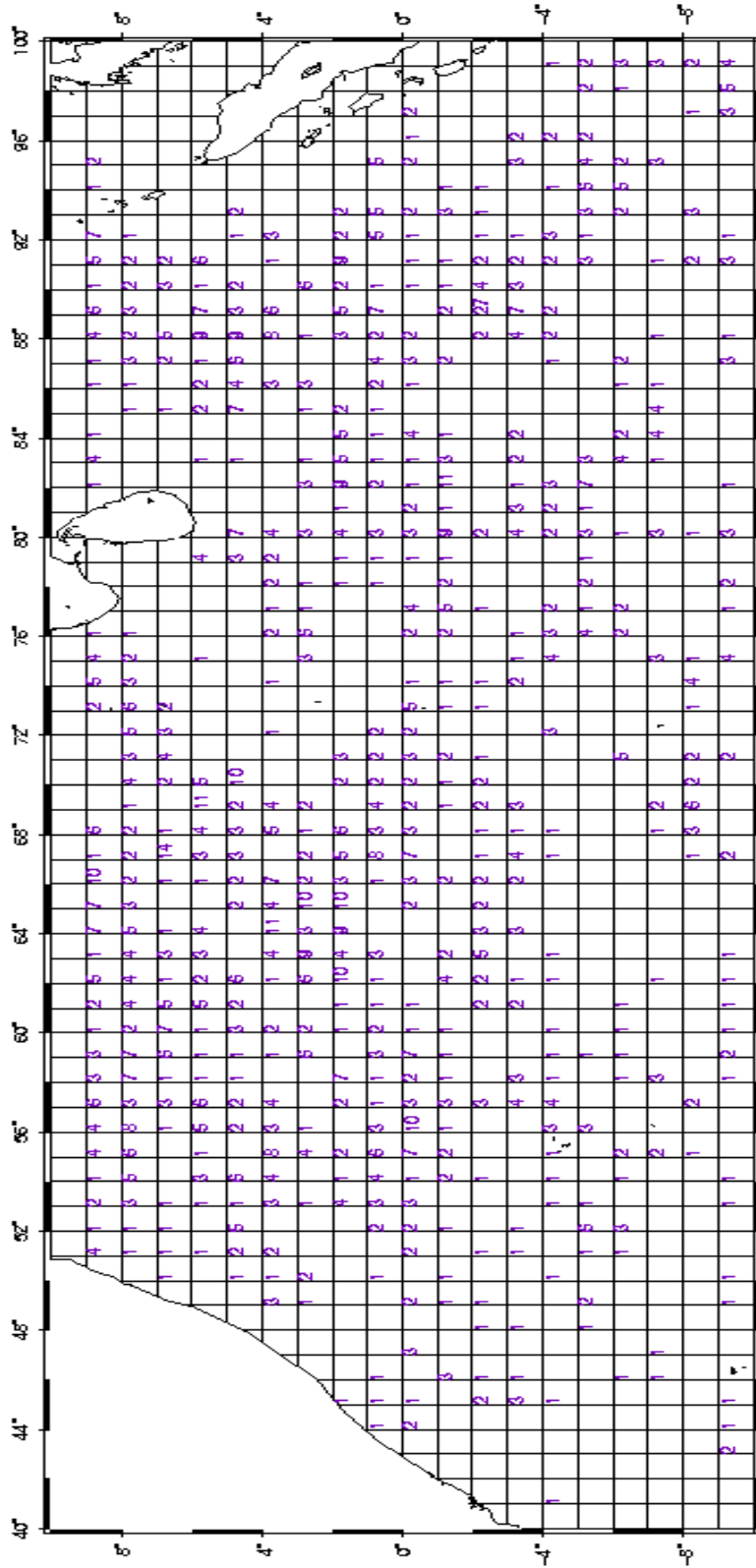
Fig.9 Total number of temperature and salinity profile (1759) obtained from CTD and ARGO in each of the  $1^{\circ} \times 1^{\circ}$  grid for the month of July



No. of Profiles: 1512

Fig.10 Total number of temperature and salinity profile (1512) obtained from CTD and ARGO in each of the 1°x1° grid for the month of August

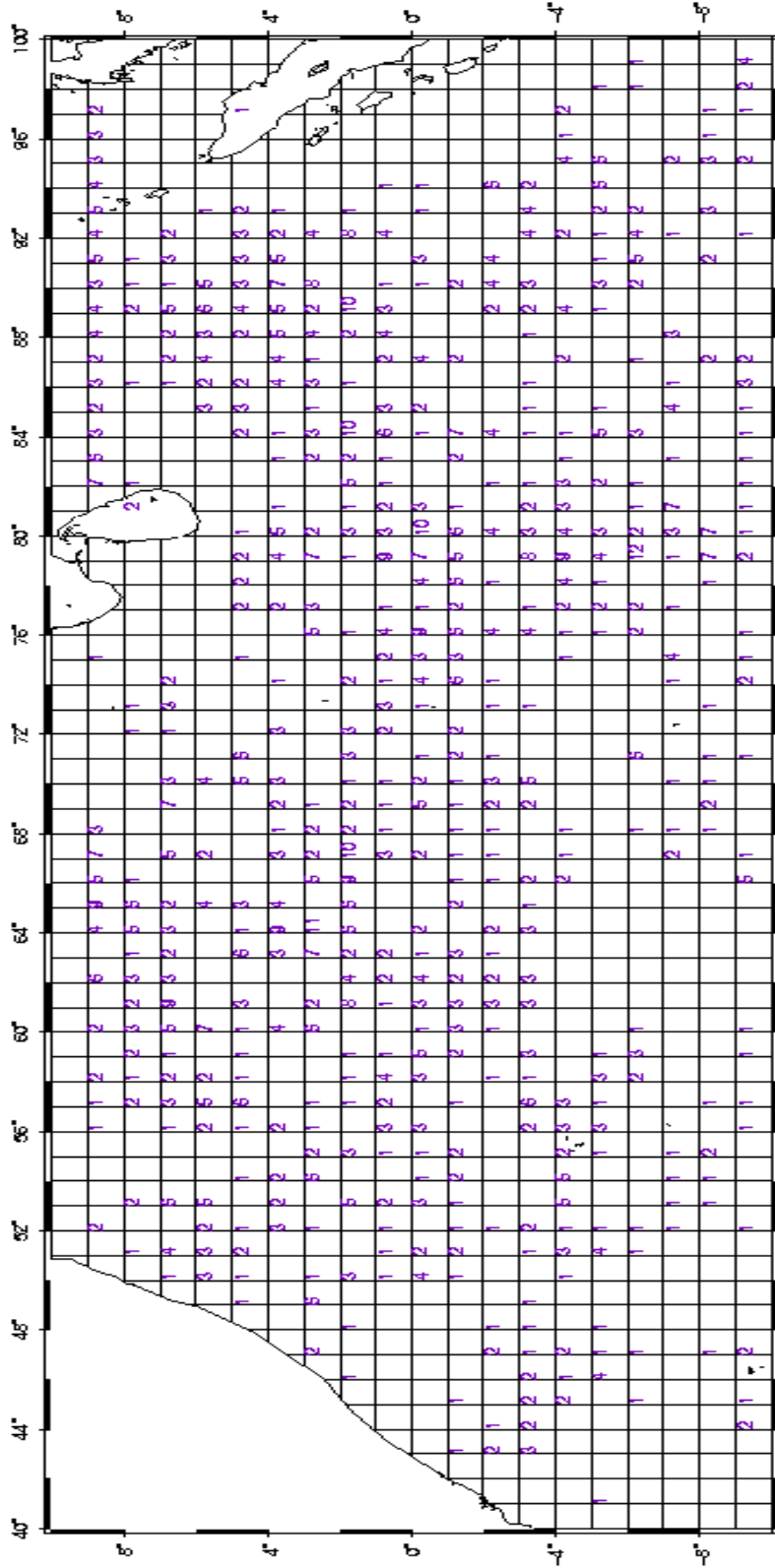
Month: SEPTEMBER  
 Duration of Data Collected: 1-Jan-1975 / 30-Dec-2006



No. of Profiles: 1553

Fig.11 Total number of temperature and salinity profile (1553) obtained from CTD and ARGO in each of the 1°×1° grid for the month of September

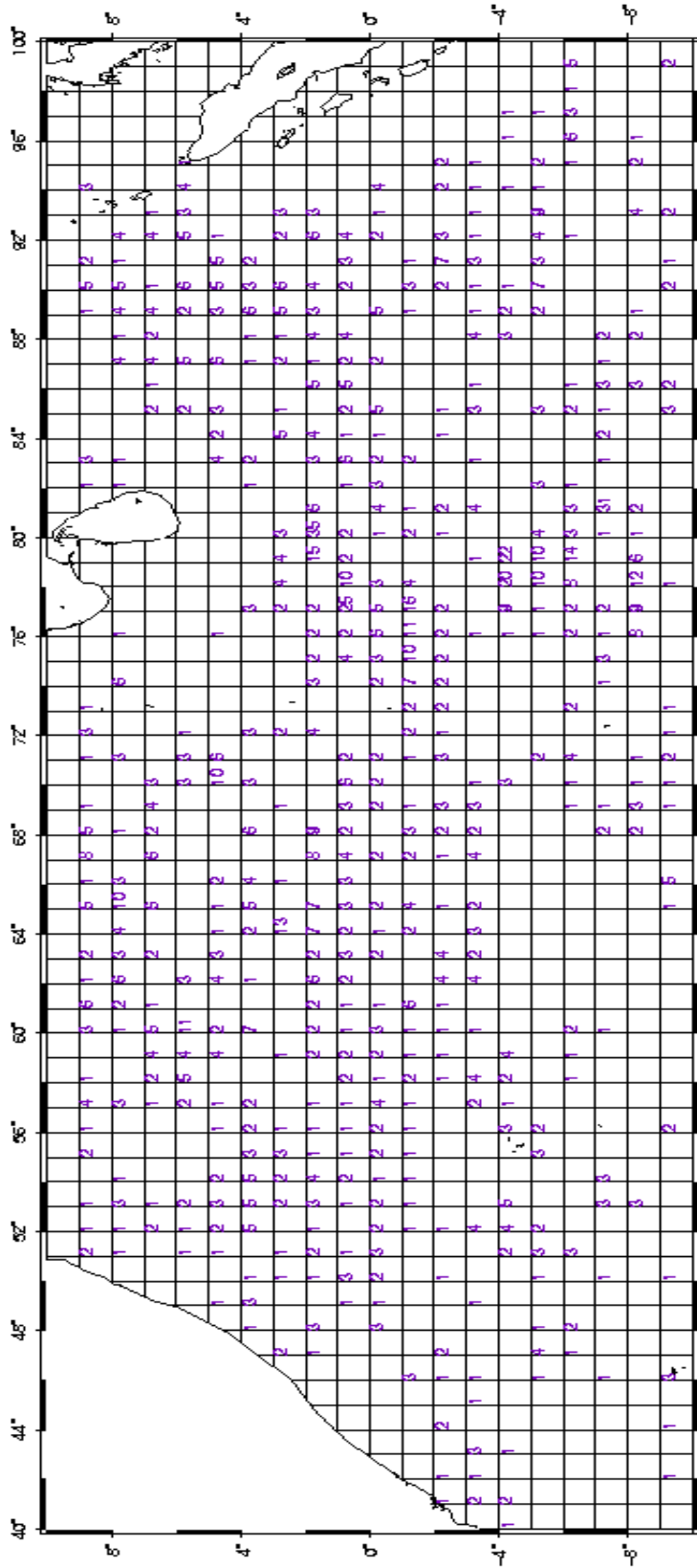
Month: OCTOBER  
 Duration of Data Collected: 1-Jan-1975 / 30-Dec-2006



No. of Profiles: 1438

Fig. 12 Total number of temperature and salinity profile (1512) obtained from CTD and ARGO in each of the 1°x1° grid for the month of October

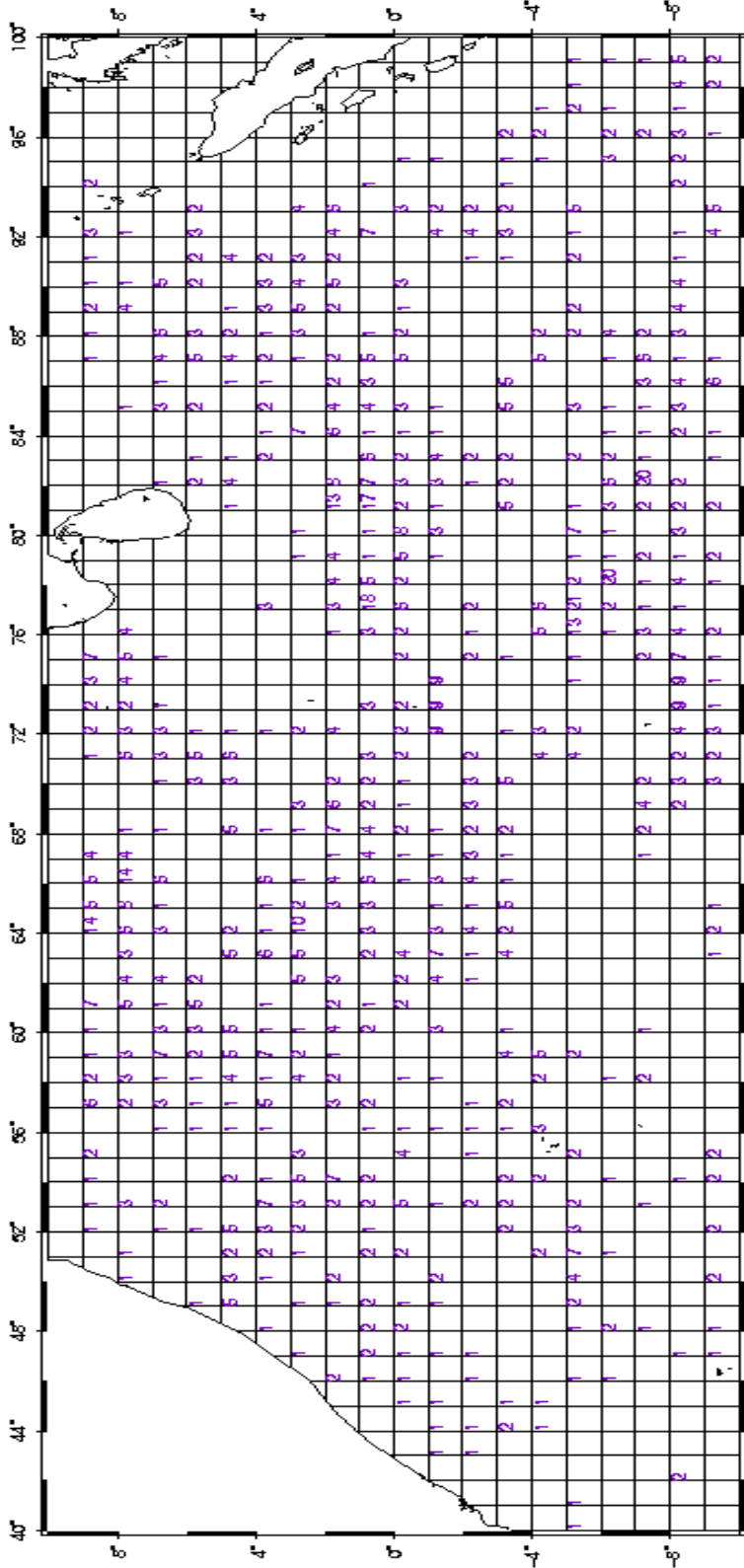
Month: NOVEMBER  
 Duration of Data Collected: 1-Jan-1975 / 30-Dec-2006



No. of Profiles: 1542

Fig.13 Total number of temperature and salinity profile (1542) obtained from CTD and ARGO in each of the 1°x1° grid for the month of November

Month: DECEMBER  
 Duration of Data Collected: 1-Jan-1975 / 30-Dec-2006



No. of Profiles: 1508

Fig.14 Total number of temperature and salinity profile (1508) obtained from CTD and ARGO in each of the 1°×1° grid for the month of December

Table.1 Total number of temperature-salinity profiles available in each month in the study domain (10°N-10°S, 40°E-100°E) from CTD and Argo

Month	Total number of CTD profiles during the period 1970 -2004	Total number of ARGO profiles during the period 2000 - 2006
January	267	935
February	183	850
March	297	923
April	456	878
May	454	960
June	270	1066
July	633	1126
August	365	1147
September	380	1173
October	207	1231
November	108	1434
December	162	1346

Spatial distribution total number of quality controlled CTD and Argo data available in each of the 1°×1° grid is presented in Fig.3 to Fig.14, while the total number of CTD and Argo profiles available in each month is presented in Table 1. From the spatial distribution of data it is evident that there are large data gaps on a monthly scale. Hence, to obtain a robust signature of oceanic variability it was decided to group the data on a seasonal basis and the seasons were defined as follows:

Spring inter-monsoon      March – May  
 Summer monsoon            June – September  
 Fall inter-monsoon        October – November  
 Winter monsoon             December – February



### **2.3.2 Criteria for selecting the mixed layer depth**

In applying the concept of mixed layer to an oceanic situation, one must be careful to choose a mixed layer definition that matches the physics of the problem being studied. Operationally, this is the depth at which some hydrographic property deviates from its surface value. Two types of mixed layer depth (MLD) definitions have been most commonly used; the first is based on specifying a difference in temperature or density relative to the surface value [Wyrski, 1994; Levitus, 1982; Schneider and Muller, 1990]. A second definition is based on specifying a gradient in temperature or density [Bathen, 1972; Lukas and Lindstorm, 1991].

In order to decide what criteria should be followed to define mixed layer, it is important to examine the distribution of (physical) properties within the upper layer. An examination of the profiles indicates that the isothermal, isohaline and isopycnal layer; in general, do not seem to coincide in the upper ocean (Fig.2). Usually, the temperature shows an isothermal layer within which the salinity increases rapidly with depth. Hence, the criteria for defining the MLD should take into account the density variation rather than temperature or salinity.

In the present study MLD is the depth at which the density ( $\sigma_t$ ) exceeds  $0.2 \text{ kg/m}^3$  from its surface value. For this purpose, the monthly mean temperature, salinity and  $\sigma_t$  profiles were interpolated onto 1 m-depth intervals by the cubic spline method.

### **2.3.3 Criteria for selecting barrier layer thickness (BLT)**

Since barrier layer is the layer within which temperature of the water column remains almost constant (isothermal) but the salinity increases drastically with depth (Fig.2). Hence depth of the barrier layer was

determined by subtracting the MLD from the isothermal layer. In the present study, isothermal layer is defined as the depth at which the temperature decreases from SST by 1°C.

### **2.3.4 Criteria for selecting mid-thermocline depth (D20)**

In tropical Ocean, depth of 20°C isotherm is generally located in the mid-thermocline region and hence in the present study middle thermocline depth is taken as the depth of the 20°C isotherm.

### **2.3.5 Sensible and Latent Heat Fluxes**

The sensible and latent heat fluxes, QH and QE, have been calculated using the bulk formulae

$$QH = \rho c_p C_h u (T_s - (T_a + \gamma z))$$

$$QE = \rho L C_e u (q_s - q_a)$$

where  $\rho$  is the density of air;  $c_p$ , the specific heat capacity of air at constant pressure;  $L$ , the latent heat of vaporization;  $C_h$  and  $C_e$ , the stability and height dependent transfer coefficients for sensible and latent heat respectively;  $u$ , the wind speed;  $T_s$ , the sea surface temperature ;  $T_a$ , the surface air temperature with a correction for the adiabatic lapse rate,  $\gamma$ ;  $z$  , the height at which the air temperature was measured;  $q_s$  , 98% of the saturation specific humidity at the sea surface temperature to allow for the salinity of sea water, and  $q_a$  , the atmospheric specific humidity. The air density is determined from the ideal gas equation in the form,

$$\rho = 0.3484 P / T_v$$

where the units of density are  $\text{kg m}^{-3}$ ,  $P$  is the reported pressure in mb and  $T_v$  the virtual temperature. The formulae used for  $c_p$  and  $L$  have been taken from Stull [1988],

$$c_p = 1004.67 + 0.84q_s$$

$$L = 10^6 [2.501 - 0.00237(T_s - 273.16)]$$

where the units are  $J kg^{-1} K^{-1}$  for  $c_p$  and  $J kg^{-1}$  for  $L$ . The rate of evaporation,  $E$ , corresponding to the latent heat flux has also been determined by taking the ratio of  $Q_E$  to  $L$ .

### 2.3.6 Wind Stress

Estimates of the zonal,  $\tau_x$ , and meridional,  $\tau_y$ , components of the wind stress has been determined using the bulk formula,

$$\tau_x = \rho C_D u_x (u_x^2 + u_y^2)^{1/2}$$

$$\tau_y = \rho C_D u_y (u_x^2 + u_y^2)^{1/2}$$

where  $C_D$  is a stability dependent drag coefficient, and  $u_x$  and  $u_y$  are the zonal and meridional components of the wind speed respectively.

### 2.3.7 Longwave Flux

$$Q_{LW} = \epsilon \sigma_{SB} T_s^4 (0.39 - 0.05e^{1/2}) (1 - \lambda n^2) + 4 \epsilon \sigma_{SB} T_s^3 (T_s - T_a)$$

where  $e$  is the emittance of the sea surface, taken to be 0.98;  $\sigma_{SB}$ , the Stefan – Boltzmann constant, equal to  $5.7 \times 10^{-8} W m^{-2} K^{-4}$ ;  $e$ , the water vapour pressure;  $n$ , the fractional cloud cover;  $\lambda$ , a latitude dependent cloud cover coefficient;  $T_s$  and  $T_a$ , the sea surface and air temperatures in degrees Kelvin.

### 2.3.8 Short-wave Flux

The monthly mean net shortwave flux,  $Q_{SW}$ , has been determined using

the Reed [1977] formula which is based on an analysis of weather ship and coastal station measurements,

$$Q_{SW} = (1 - \alpha) Q_c [1 - 0.62 n + 0.0019 \theta_N]$$

where  $\alpha$  is the albedo;  $Q_c$ , the clear - sky solar radiation ;  $n$ , the monthly mean fractional cloud cover and  $\theta_N$ , the monthly mean local noon solar elevation.

### 2.3.9 Net Heat Flux

The net heat flux,  $Q_{Net}$ , is given by the sum of the four individual components,

$$Q_{Net} = Q_H + Q_E + Q_{LW} + Q_{SW}$$

### 2.3.10 Precipitation

Estimates of the precipitation rate,  $P$ , have been obtained from the Present Weather field where available in COADS1a using a modified version of the empirical parameterisation developed by Tucker [1961]. The parameterisation was originally based on station data collected in the vicinity of the British Isles and has subsequently been revised by Dorman and Bourke [1978] in an attempt to allow for the stronger rainfall rates typical of the tropics. For this purpose, they introduced an air temperature dependent correction factor and we have made use of their suggested annual mean relationship such that,

$$P = (a + bT + cT^2) P_T$$

Where  $P_T$  is the rate obtained with original Tucker [1961] parameterisation,  $a = 0.507$ ,  $b = 0.0506$  and  $c = 0.00341$ .

The monthly mean climatology was used for all the atmospheric parameters.

# **Chapter 3**

## **Results and Discussion**

## **3.1 Seasonal cycle of oceanic parameters**

### **3.1.1 Seasonal cycle of sea surface temperature**

The study domain showed high sea surface temperature (SST), in excess of 29°C, during the spring inter-monsoon (March-May), except along the African coast where it was 1°C cooler (Fig.15). Highest SST of  $\approx 30^\circ\text{C}$  was found near the Sumatra region. During summer season (June to September), there were two regions of cold SST, one west of 55°E and the other in the southern part of Indian peninsula (Fig.16). In both regions SST values were  $<25.5^\circ\text{C}$  along the African coast and southwestern region. These low SSTs may be linked to the process of upwelling along the Somali coast as well as the southern part of the west coast of India. However, the low SST in the southwestern region is away from the boundary and may not be linked to coastal upwelling process. In the rest of the region SST values increased from west to east and high values ( $\approx 29^\circ\text{C}$ ) were found around the equator between 60°E to 100°E. In the fall inter-monsoon (October, November) the colder regions along the western boundary appeared to have spread towards off shore, especially in the southwestern region. The cold SST patch near the Indian peninsula disappeared during this period. However, colder SST was seen as a zonal band near 10°S. In the rest of the region, SST was between 28° and 29°C. During winter season (December to February), low SST ( $<26.5^\circ\text{C}$ ) was observed along the African coast (Fig.18). East of 55°E, SST showed weak gradient towards east and increased to 29°C around the Sumatra coast.

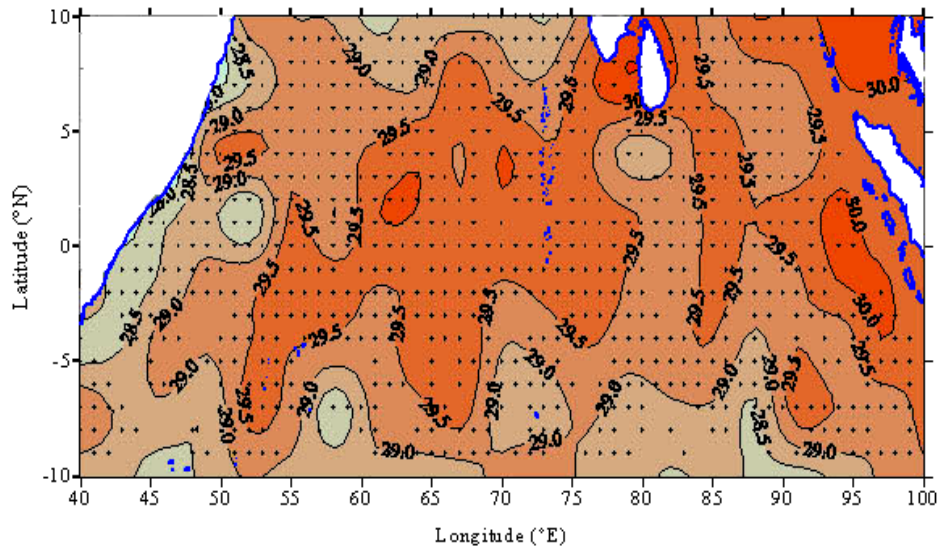


Fig.15 Spatial distribution of SST ( $^{\circ}$ C) during spring inter-monsoon.

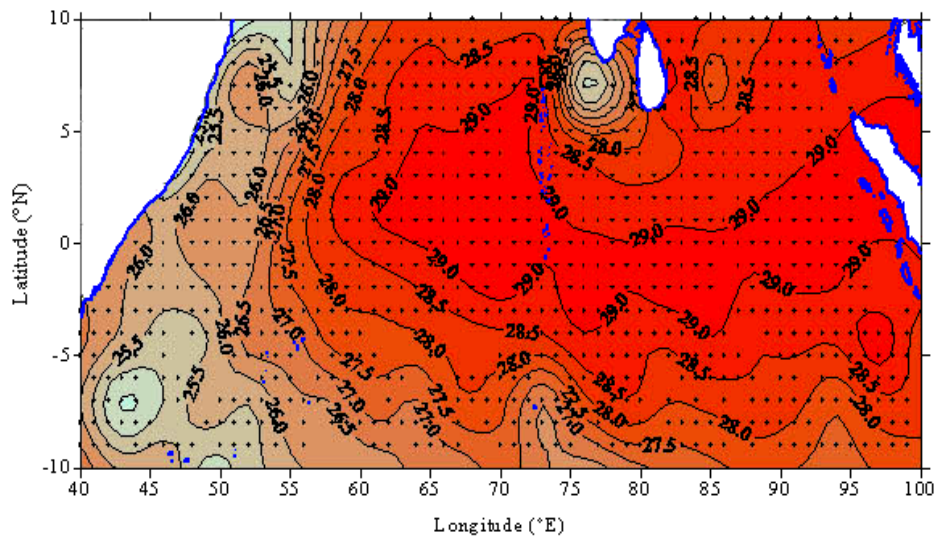


Fig.16 Spatial distribution of SST ( $^{\circ}$ C) during summer monsoon.

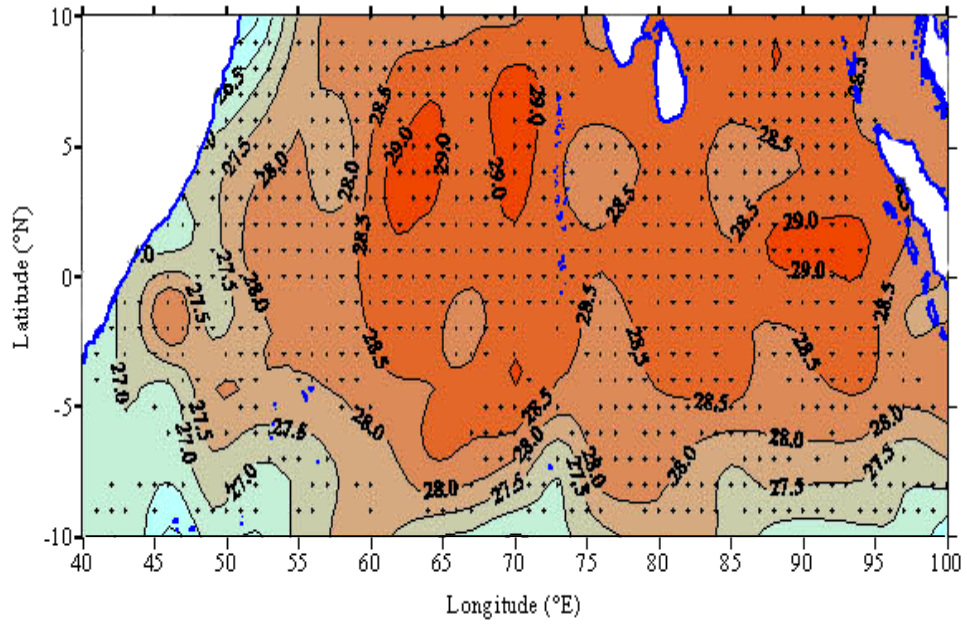


Fig.17 Spatial distribution of SST ( $^{\circ}$ C) during fall inter-monsoon.

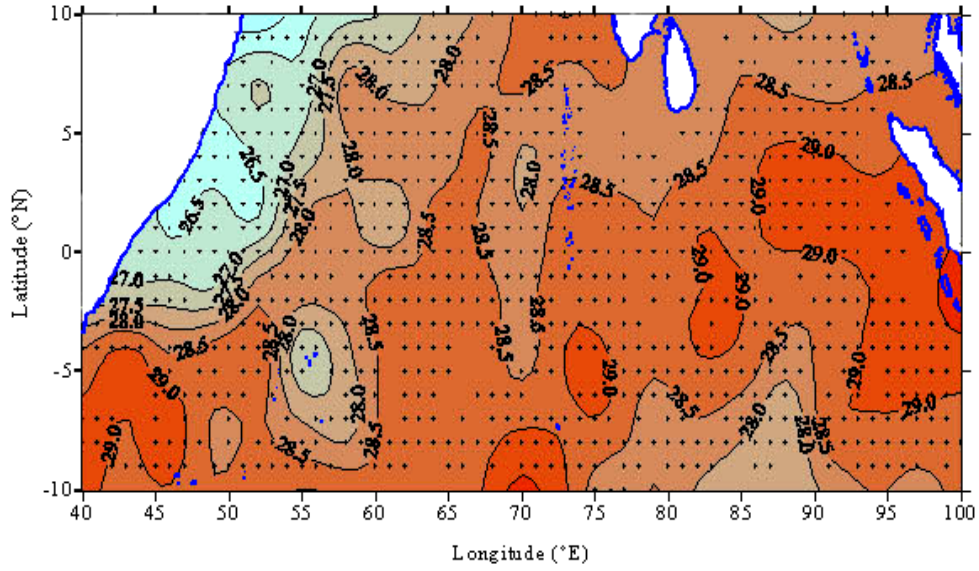


Fig.18 Spatial distribution of SST ( $^{\circ}$ C) during winter monsoon.



In summary, highest SST (30°C) occurred during spring inter-monsoon, followed by fall inter-monsoon, when the entire study domain showed the least spatial variability of 2°C. The coldest SST was seen in summer (<25.5°C), followed by winter (<26.5°C) near the western boundary and southern part of peninsular India (only during summer). Though the spatial variability of SST during summer as well as winter was about 4°C, the SST gradient near the western boundary was large in summer. In general, western EIO was colder than eastern EIO in any given season, and the SST in the eastern EIO was always >29°C.

### **3.1.2 Seasonal cycle of sea surface salinity**

During spring inter-monsoon sea surface salinity (SSS) distribution showed that the high salinity waters, in excess of 35 psu, occupies the entire region west of 65°E, but extends up to about 75°E along the equator (Fig. 19). This high salinity waters appear to have originated from the Arabian Sea and advected towards south in the western region and a part of it moved towards the east along the equator. A distinct low salinity region, with salinity <34psu, was noticed in the eastern region north of 5°N and east of 70°E. The Lowest salinity in this region was less than 33psu which occurred close to 10°N. The orientation of salinity front indicated the influence of the advection of low salinity waters from the Bay of Bengal. Along the eastern boundary also the salinity was less than 34 psu. A second region of low salinity water was also noticed close to 10°S in the eastern region which may be linked to Indonesian through flow.

In summer, the advection of high salinity waters from the north seen during spring extends much further south and east (Fig.20). Similarly, the

advection of low salinity waters from the Bay of Bengal was also seen extending towards south. The salinity distribution in summer clearly demarcated two regimes, low salinity waters confined to east of  $95^{\circ}\text{E}$ , while the rest of the region was occupied by high salinity waters. Note that the highest ( $>36$  psu) and lowest ( $<33$  psu) salinity waters were in the north, north of  $5^{\circ}\text{N}$ , indicating the source of each.

During fall inter-monsoon, the salinity distribution pattern remained similar to that of summer (Fig.21). But the region of high salinity waters increased spatially; see for example the location of 36psu contour. There is also an indication of westward extension of low salinity waters from the southeastern region of the study domain.

In winter season advection of high salinity waters from the north showed a decrease, as inferred from the location of 36psu contour which was very close to  $10^{\circ}\text{N}$  (Fig.22). The low salinity waters seen in the northeastern region showed a westward extension. In fact this low salinity water is seen south of Sri Lanka and up to eastern part of peninsular India. This, in fact, is the signature of advection of low salinity Bay of Bengal waters in to the Arabian Sea, which occurs during winter season. There is also another region of westward advection of low salinity waters from the southeaster region near  $10^{\circ}\text{S}$ . This is the signature of Indonesian through flow.

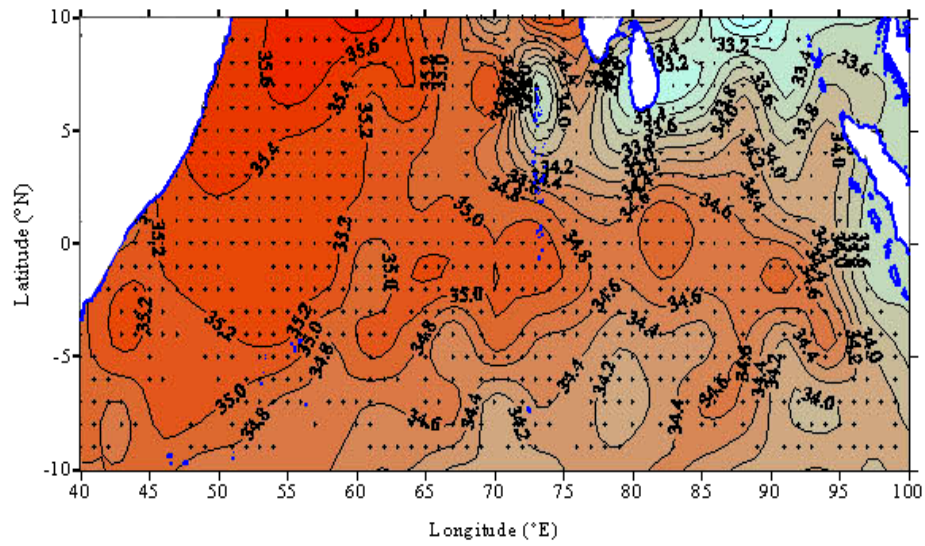


Fig.19 Spatial distribution of SSS (psu) during spring inter-monsoon.

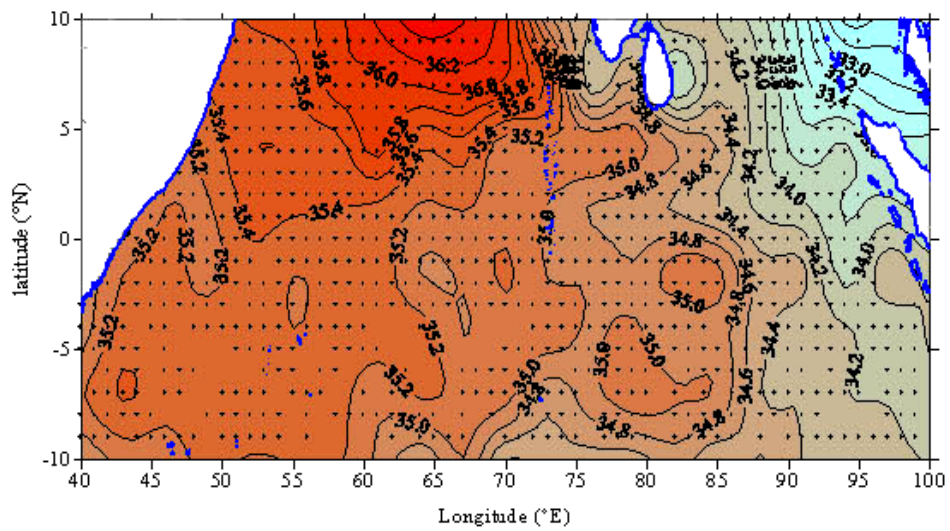


Fig.20 Spatial distribution of SSS (psu) during summer monsoon.

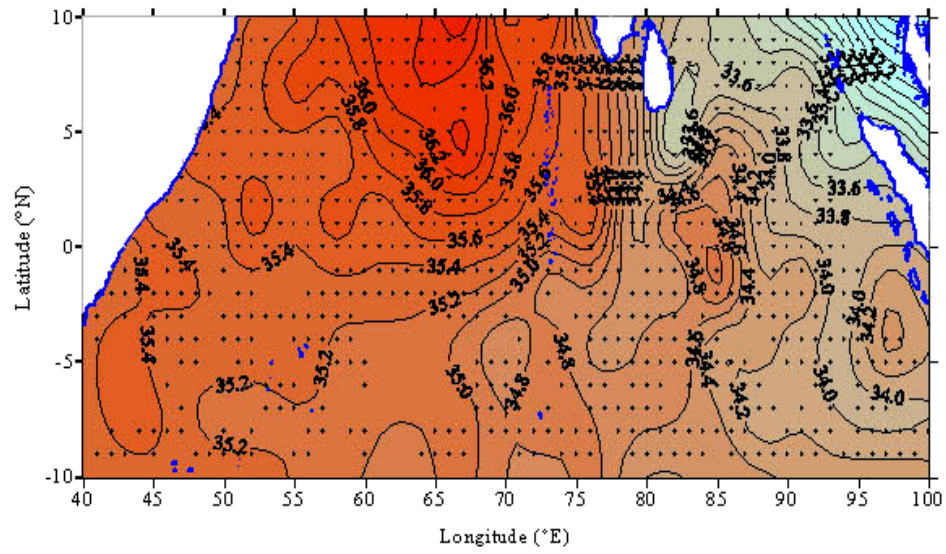


Fig.21 Spatial distribution of SSS (psu) during fall inter-monsoon.

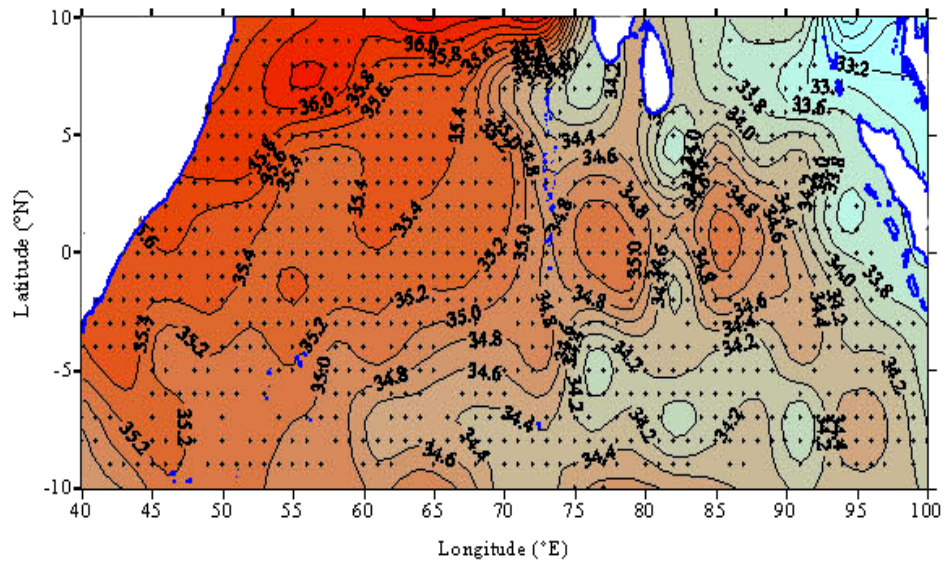


Fig.22 Spatial distribution of SSS (psu) during winter monsoon.

In summary, the salinity distribution clearly demarcated two regimes with high salinity in the western and low salinity in the eastern regions with the central EIO being the region of mixing. The source of high salinity water is from the Arabian Sea, while the low salinity waters are of the Bay of Bengal origin. The advection of high salinity waters begins during summer monsoon which get intensified in fall-intermonsoon expanding towards south. During winter it recedes, and its region of influence was the least in spring-intermonsoon. This seasonal cycle of advection of high salinity waters from the Arabian Sea was linked to the direction of flow of zonal currents. During summer monsoon the IMC carried the high salinity waters from western EIO towards east which continued till late fall-intermonsoon. As, the winter monsoon sets in, the low salinity waters of the Bay of Bengal origin spreads towards further west from the eastern boundary by the NEC, and pushes the high salinity waters towards the west. In the north, intrusion of Bay of Bengal waters into the Arabian Sea was also seen during winter. In the south, Indonesian through flow was seen as spreading of low salinity waters near  $10^{\circ}\text{N}$ .

### **3.1.3 Seasonal cycle of mixed layer depth**

During spring-intermonsoon deep mixed layer depth (MLD), greater than 30 m, was encountered in the western EIO as well as with in  $5^{\circ}\text{N}$  to  $5^{\circ}\text{S}$  (Fig. 23). In the north of  $5^{\circ}\text{N}$  and south of  $5^{\circ}\text{S}$ , MLD was shallower than 30 m. Along the eastern boundary MLD was around 20 m while that along the western boundary was  $\sim 35\text{-}40\text{m}$ . This pattern of MLD could be understood in the light of salinity distribution and the zonal current pattern. The region of deep MLD along the equator is region where high salinity waters occurred and also the region where the spring-tie Wyrtki jet moves eastward. The deep MLD is an indication of sinking in this

region. As the eastward jet encounters the eastern boundary part of the flow will follow the coast towards north and south leading to upwelling close to the coast. The shallow MLD is an indication of this process. The shallow MLD in the north and south was associated with the low salinity in this region which shows fresh water control of MLD.

The striking feature during summer monsoon was the occurrence of shallow MLDs near peninsular India ( $< 15$  m) and east of Sri Lanka ( $< 25$  m) and near the southeastern region near the Sumatra coast ( $< 25$  m) (Fig.24). These shallow MLDs are the signature of summer upwelling. The deep MLD in the western EIO may be due to the strong wind mixing under the influence of strong southeast trade winds which turns and becomes southwesterly after crossing the equator. North of equator, a path of shallow MLD ( $< 35$  m) was noticed close to the western boundary, which may be the result of upwelling along the Somalia region.

During fall-intermonsoon, MLD in general was shallow ( $< 30$  m) in the study domain, except in patches close to the western boundary, in the central EIO, and in a zonal band in the south, south of  $5^{\circ}\text{S}$  (Fig. 25). The distinct shallow MLD patch close and parallel to the western boundary indicated the upwelling along the African coast which originated in summer and slowly gets advected offshore with time. The zonal band of shallow MLD north of  $7^{\circ}\text{N}$ , and east of  $70^{\circ}\text{E}$ , separated by Indian peninsula indicated two different processes. West of the Indian peninsula the zonal band of shallow MLD is due to the offshore advection of coastally upwelled waters under the influence of westward propagating Rossby wave. East of the Indian peninsula, the zonal band of shallow MLD is due to the advection of low salinity Bay of Bengal waters and

shows the role of fresh water in regulating MLD. The reason for deep MLD in the south may be linked to the increase in the strength of wind during this period.

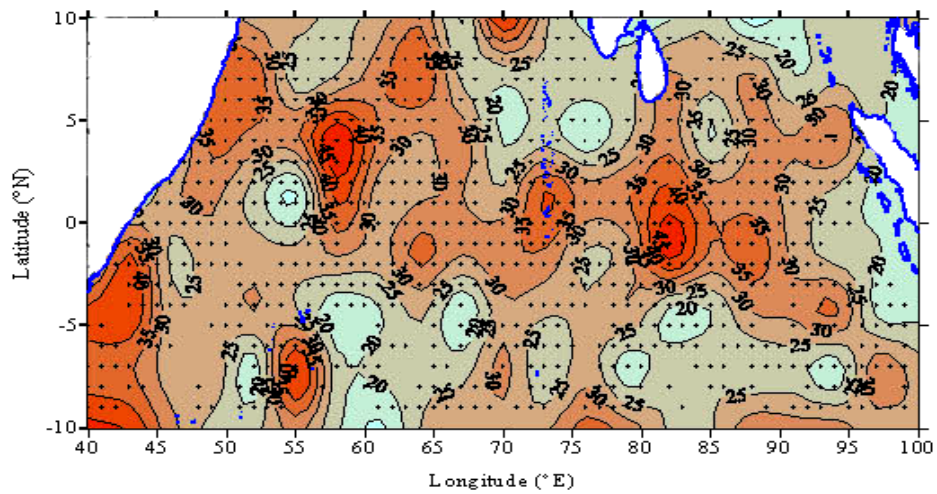


Fig.23 Spatial distribution of MLD (m) during spring inter-monsoon.

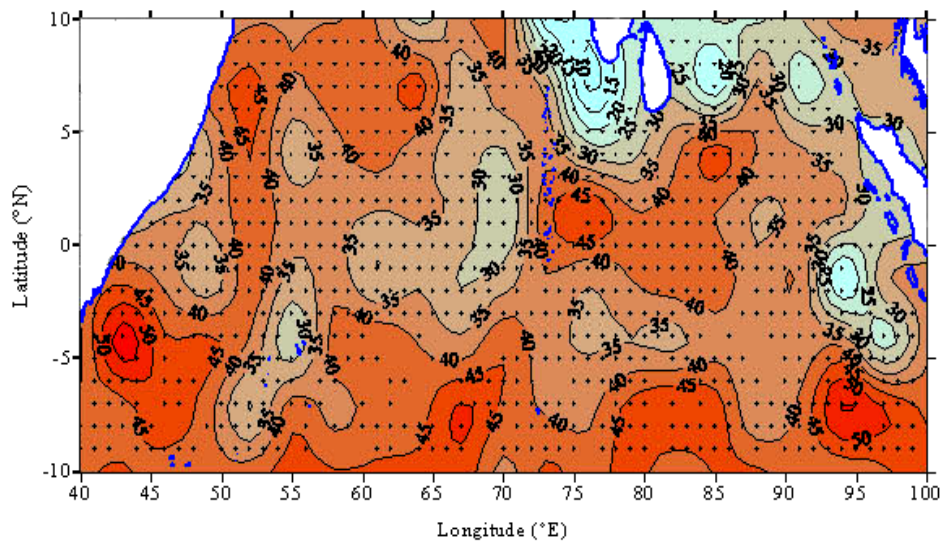


Fig.24 Spatial distribution of MLD (m) during summer monsoon.

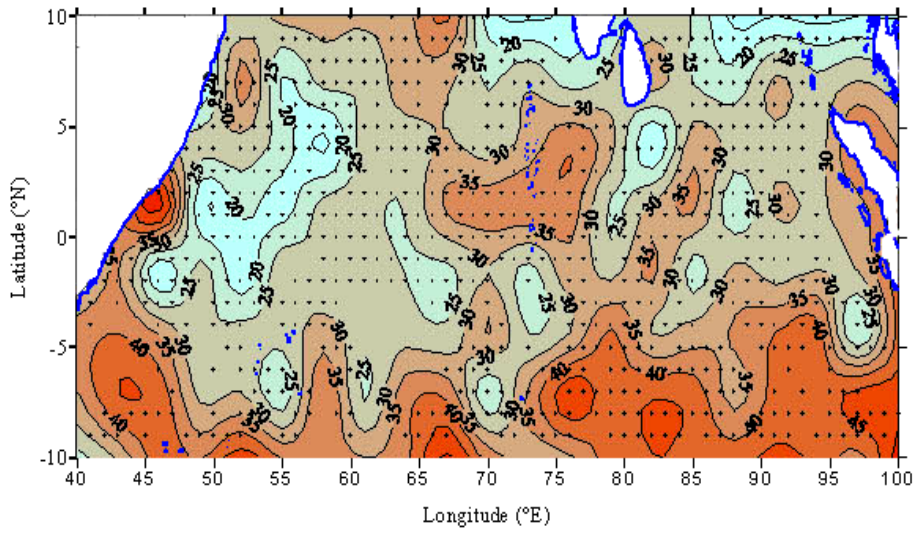


Fig.25 Spatial distribution of MLD (m) during fall inter-monsoon.

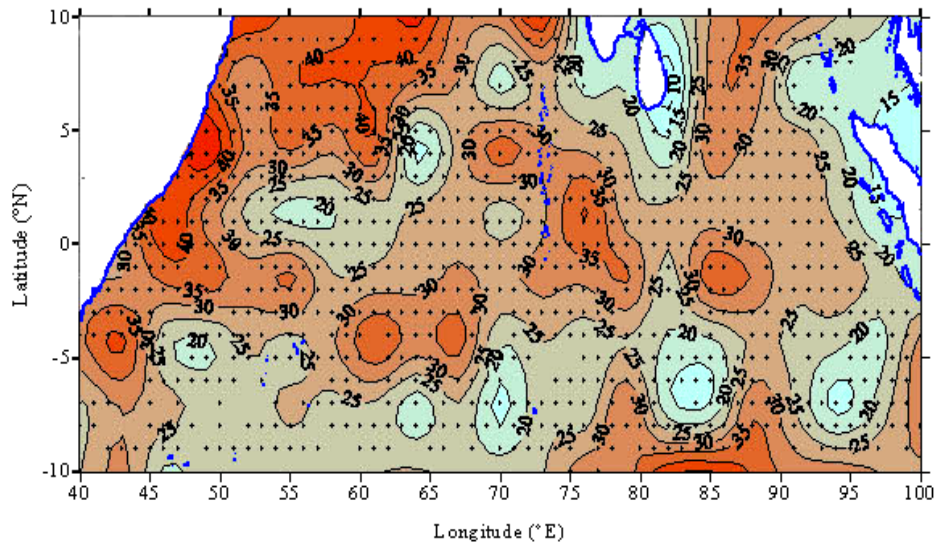


Fig.26 Spatial distribution of MLD (m) during winter monsoon.



In the winter monsoon deep MLD,  $> 30$  m, was seen in most of the region, especially in the western and central EIO regions (Fig. 26). Shallow MLDs were seen around Indo-Sri Lanka region, along the eastern boundary, and south of  $5^{\circ}\text{S}$ . In general these shallow MLD regions were also the regions where low salinity waters were observed during winter, indicating that MLD was controlled by the fresh water rather than wind or other factors. The deep MLD along the western boundary may in parts be due to the downwelling and sinking associated with the southward moving Somali current in winter

In summary, in all seasons southwestern region (south of  $2^{\circ}\text{S}$ ,  $40\text{-}50^{\circ}\text{E}$ ) showed comparatively high MLD ( $> 35$  M), while in the northwestern region deep MLD was seen during summer and winter seasons and shallow MLD during spring and fall seasons. But in all seasons, eastern boundary along Sumatra-Java region showed shallow MLD ( $\approx 25\text{m}$ ), so also the northeastern part, as well as the Indo-Sri Lanka region. The shallow MLD in summer in the Indo-Sri Lanka region was driven by the upwelling while that off African coast during fall inter-monsoon was due to eastward extension of the upwelling zone. The deeper MLD in the western region in summer and winter showed the role of wind-driven mixing of high salinity waters where stratification was less. In contrast, the shallow MLD in the eastern region showed the role of fresh water which induced strong stratification to the water column. The deep MLD in spring inter-monsoon along the equator indicated the sinking associated with the eastward moving Wyrtki jet. When it encounters the eastern boundary, the subsequent flow towards north and south give rise to upwelling, as was noticed in the form of shallow MLD near the Java-Sumatra region in spring inter-monsoon.

### **3.1.4 Seasonal cycle of Barrier layer thickness**

During spring inter-monsoon, eastern EIO east of 80°E showed a region of thick barrier layer (BLT) (> 30 m) (Fig.27). Within this region a patch of deep barrier layer occurred near the southeastern boundary where the thickness exceeded 50m. In general, the barrier layer thickness west of 80°E, varied between 10 and 20 m. However, there were also few patches of thick barrier layer in the central EIO and close to the western boundary.

In summer, there were two distinct regions where thick barrier layer was encountered, one close to the eastern boundary east of 82°E, and the other north of equator between the western boundary and west of 70°E (Fig. 28). In both regions barrier layer thickness were in excess of 50 m reaching up to 65 m. The region around the peninsular India and Sri Lanka, as well as the region south of equator and away from the eastern boundary, barrier layer was the thinnest varying between 10 to 20 m.

During fall inter-monsoon, specific changes were noticed in the distribution pattern compared to that of summer. For example, the thick barrier layer near the eastern boundary seen during summer expanded towards west up to 75°E (Fig. 29). It may be noted that though the spatial extent of the thick barrier layer patch increased towards the west compared to summer, its thickness showed a decrease. The zone of thick barrier layer seen between 5°N and 10°N in the western region in summer, seen confined zonally along 10°N between 65° and 75°E. The rest of the region showed thin barrier layer.

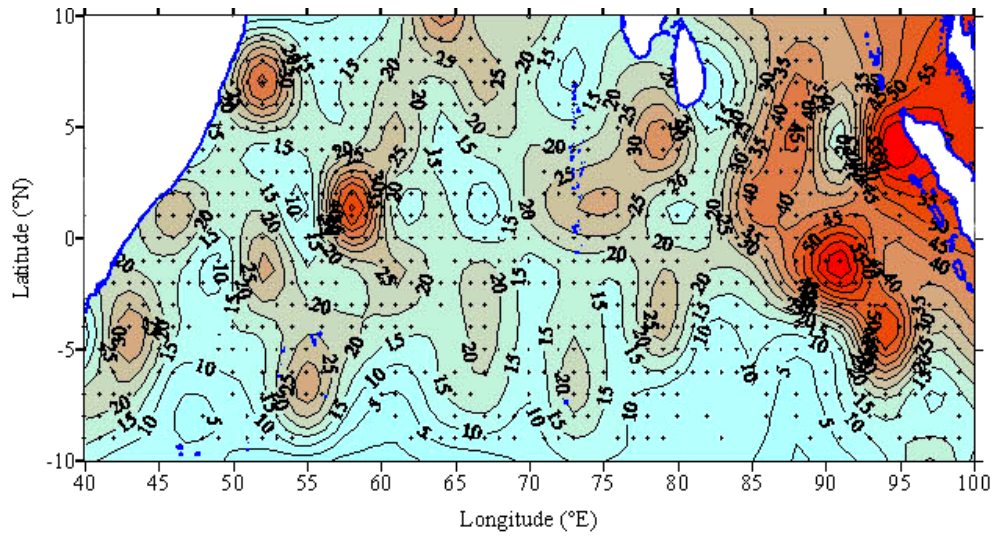


Fig.27 Spatial distribution of BLT (m) during spring inter-monsoon.

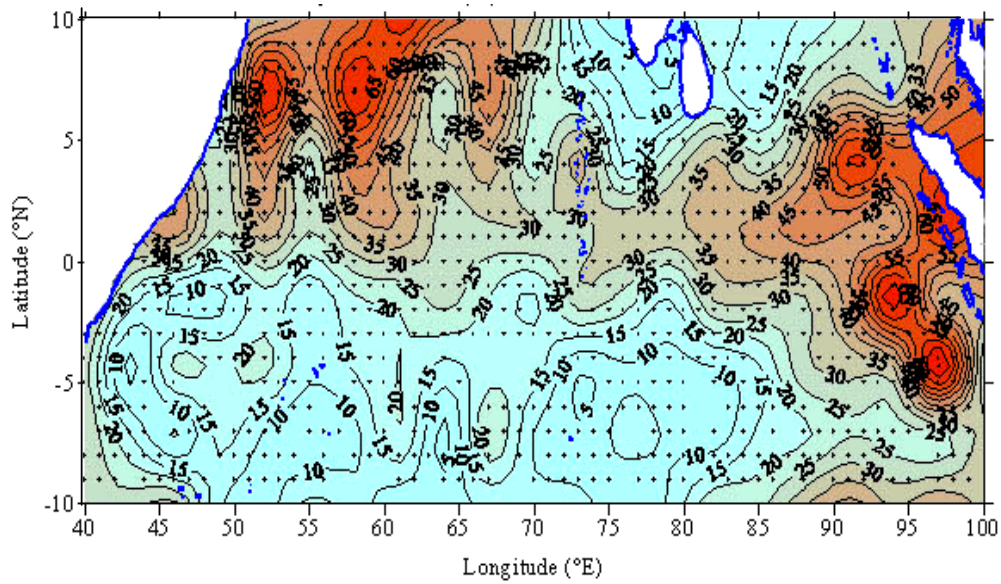


Fig.28 Spatial distribution of BLT (m) during summer monsoon.

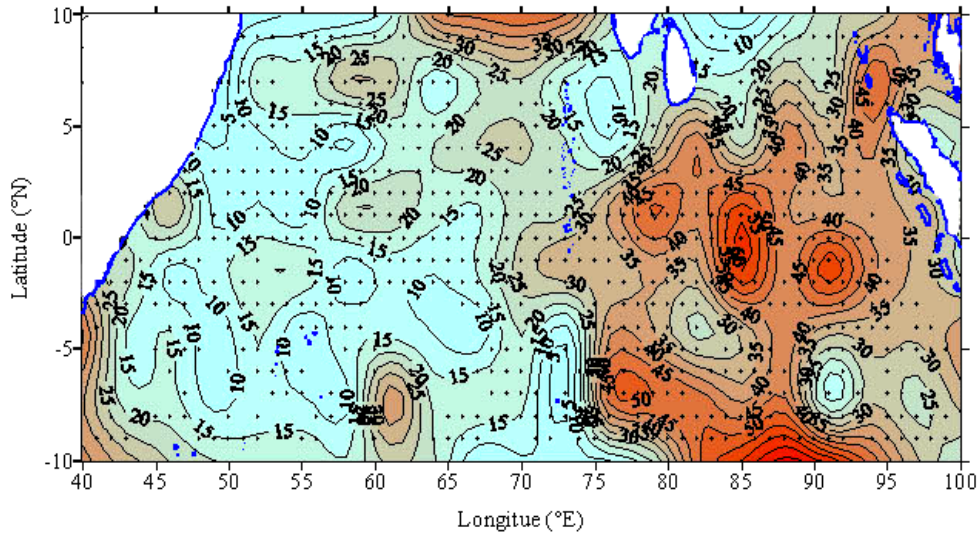


Fig.29 Spatial distribution of BLT (m) during fall inter-monsoon

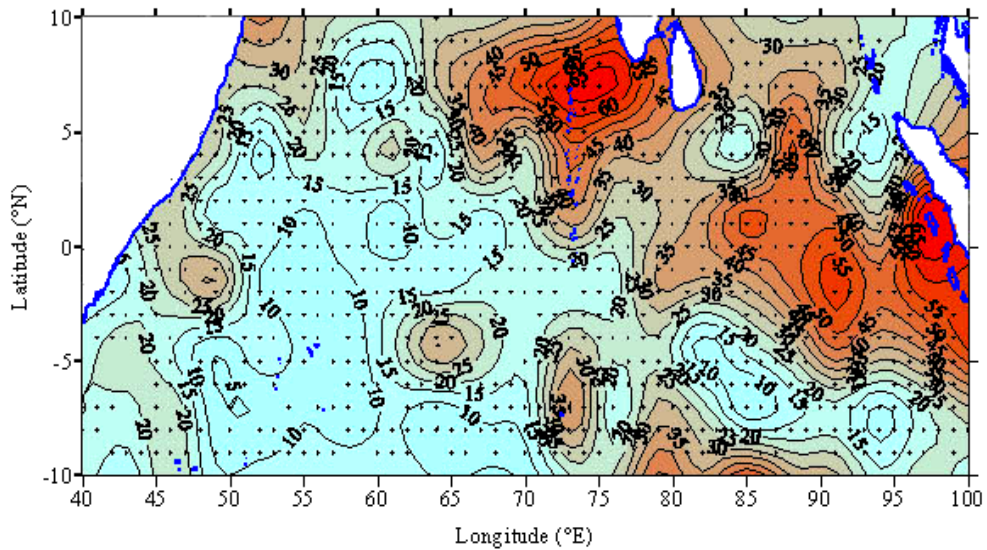


Fig.30 Spatial distribution of BLT (m) during winter monsoon

In winter, the patten of spatial distribution of barrier layer thickness was different from that seen during the rest of the season. Two regions of thick barrier layer was noticed, one patch around Indo-Sri Lanka region, the other one closer to the eastern EIO, confined to north of 5°S (Fig.30).

The thickest barrier layers in both the regions were about 50-60m. The advective processes appeared to have joined these two patches into a larger path oriented in a southeast-northwest direction.

In summary, the seasonal cycle of barrier layer thickness showed strong relationship with the distribution of sea surface salinity. In general, the region of low salinity coincided with the region of thick barrier layer. Two regions of thick barrier layer were found during fall and winter, one near the Indo-Sri Lanka and the other in the eastern EIO. Both of these regions should show strong link to fresh water flux, the former related to advective processes which transports fresher Bay of Bengal waters into the eastern part of the Arabian Sea, while the later to E-P.

### **3.1.5 Seasonal cycle of the middle thermocline**

During spring inter-monsoon, mid-thermocline depth (D20) was deeper in the study domain except in three regions where D20 was less than 100 m (Fig. 31). These three regions were a small patch south of Sri Lanka, zonal band south of 5°S, and southern part of Sumatra. Deepest D20 of greater than 140 m was encountered in the northern most part of Java and northwestern region.

The spatial structure of D20 seen during spring inter-monsoon becomes more organized in summer with the two shallow region of D20 off the Indo-Sri Lanka and south of 5°S, becoming much more shallow (Fig. 32). The region of deep D20 in the northwestern region also extends south wards and also the deepest value encountered was 160m.

During fall inter-monsoon, also high values ( $\approx 140\text{m}$ ) were observed at the northwestern region and also in the southeastern part (south of 5°S

and 80-95°E) (Fig.33). Low values were seen at the southern region (south of 5°S and west of 70°E).

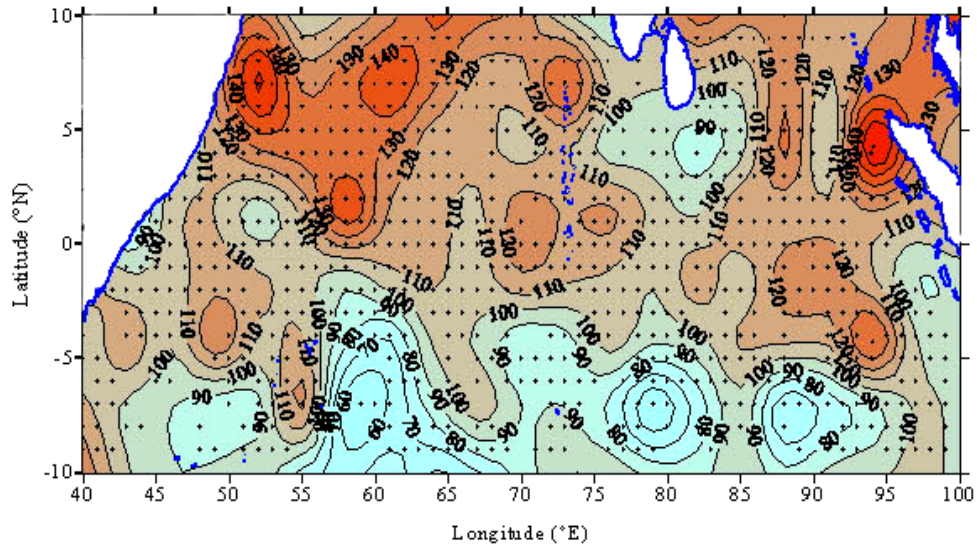


Fig.31 Spatial distribution of D20 (m) during spring inter-monsoon

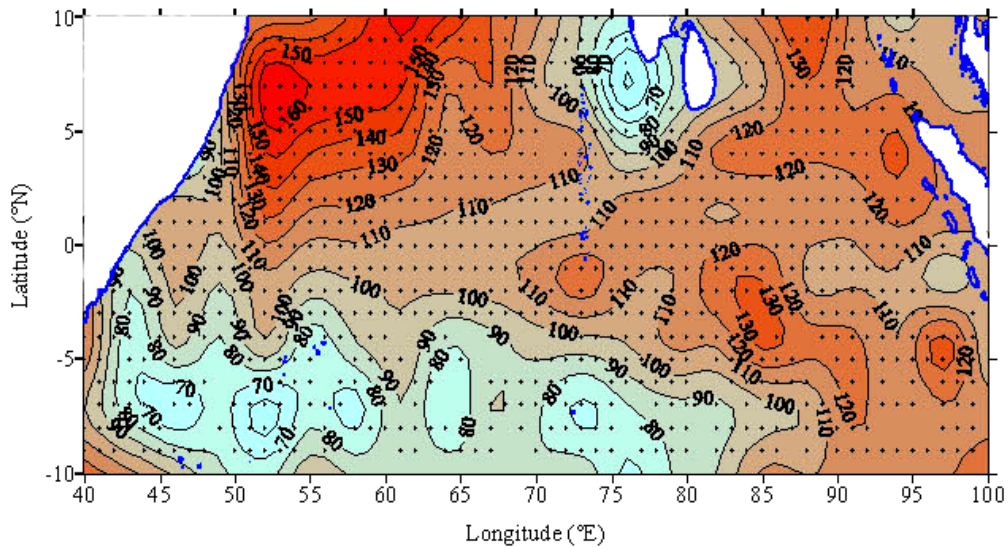


Fig.32 Spatial distribution of D20 (m) during summer monsoon

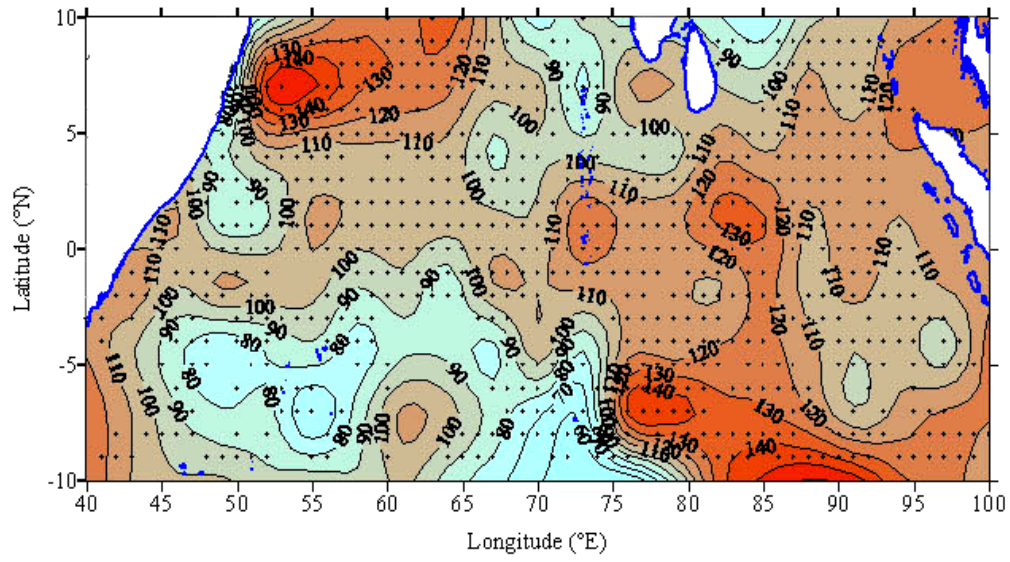


Fig.33 Spatial distribution of D20 (m) during fall inter-monsoon

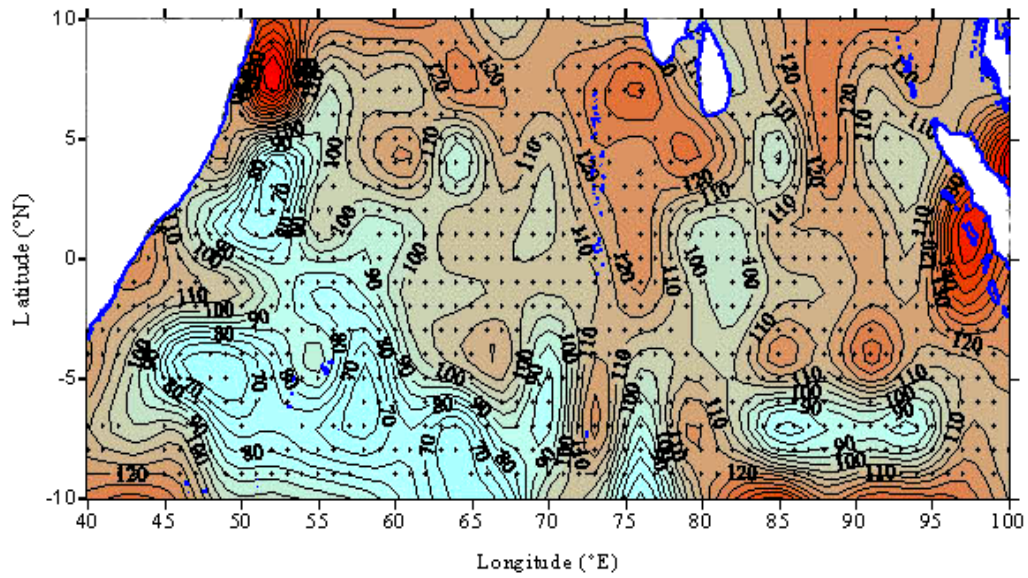


Fig.34 Spatial distribution of D20 (m) during fall winter monsoon

In winter, the western region and zonal band south of 5°S showed shallow D20 with very strong gradient varying from 100 to 70m (Fig.34). The depth of the deep D20 region decreased to 130m from the fall inter-monsoon value of 150m.

In summary, the deep D20 were seen at the northwestern region throughout the year. The shallow D20 south of Sri Lanka during spring inter-monsoon and around Indo-Sri Lanka region may have link to upwelling processes and associated thermocline changes. Similarly, the shallow D20 region seen in a zonal band south of 5°S, during summer may be related to the divergence in the wind and thermocline ventilation.

### **3.1.6 Surface current distributions**

OSCAR (Ocean Surface Current Analysis- Real time) monthly mean climatology was used to study the seasonal cycle of surface current. During January and March a fully developed westward flowing NEC was seen from north of equator up to 2°S (Fig. 35). Between 2°S and 8°S, an eastward flowing ECC was noticed all the way from west to east, and south of 8°S the flow was weak but towards west. In April NEC weakens, but the currents close to equatorial region between 2°N to 2°S and east of 65°E strengthen which is the spring-time Wyrтки jet. Strengthening of ECC was also noticed during this time. Another feature was the strong currents as a part of the clockwise gyre between 4°S and 8°S, around 60°E. Spring-time jet was also seen in May, but in the southern EIO, currents weakened further (Fig.36). By June an organized eastward flowing SMC was noticed, which was seen turning around the Indo-Sri Lanka region and flowing into the Bay of Bengal. In July, SMC was strongest east of 75°E and flows southward along the eastern boundary. Along the western boundary the flow was northerly which formed a part



of the closed anti-cyclonic gyre west of  $70^{\circ}\text{E}$ . The flow pattern during summer in south of the equator appeared as meridional flow towards south, which turned westward near the western region. The circulation remained similar in August and September (Fig. 37), but its strength progressively decreased. In fall inter-monsoon (October-November) the organized zonal flow was noticed only in the equatorial region between  $2^{\circ}\text{N}$  and  $2^{\circ}\text{S}$ , while in the rest of the region the flow was weak and variable. In December, once again the signature of westward flowing NEC was discernible, especially in the eastern region north of equator.

In summary, the seasonal cycle of surface current reflects, the response of upper ocean circulation to seasonally reversing monsoon winds. During winter when the equatorial Indian Ocean resembles the other equatorial regions of the world ocean, the NEC flows westward from north of equator and extends up to  $2^{\circ}\text{S}$ , followed by ECC between  $2^{\circ}\text{S}$  and  $8^{\circ}\text{S}$  flowing towards east. South of ECC, the SEC flows towards west. In summer, the NEC was replaced by the eastward flowing SMC, which merging with ECC flows to east as a strong current forced by summer monsoon winds. During spring and fall inter-monsoons when the equatorial winds are westerly, an organized zonal flow was seen only within the equatorial wave guide,  $2^{\circ}\text{N}$  and  $2^{\circ}\text{S}$ , which flows towards the east and was the Wyrтки jet. During this period, current elsewhere in the study domain was weak and und organized.

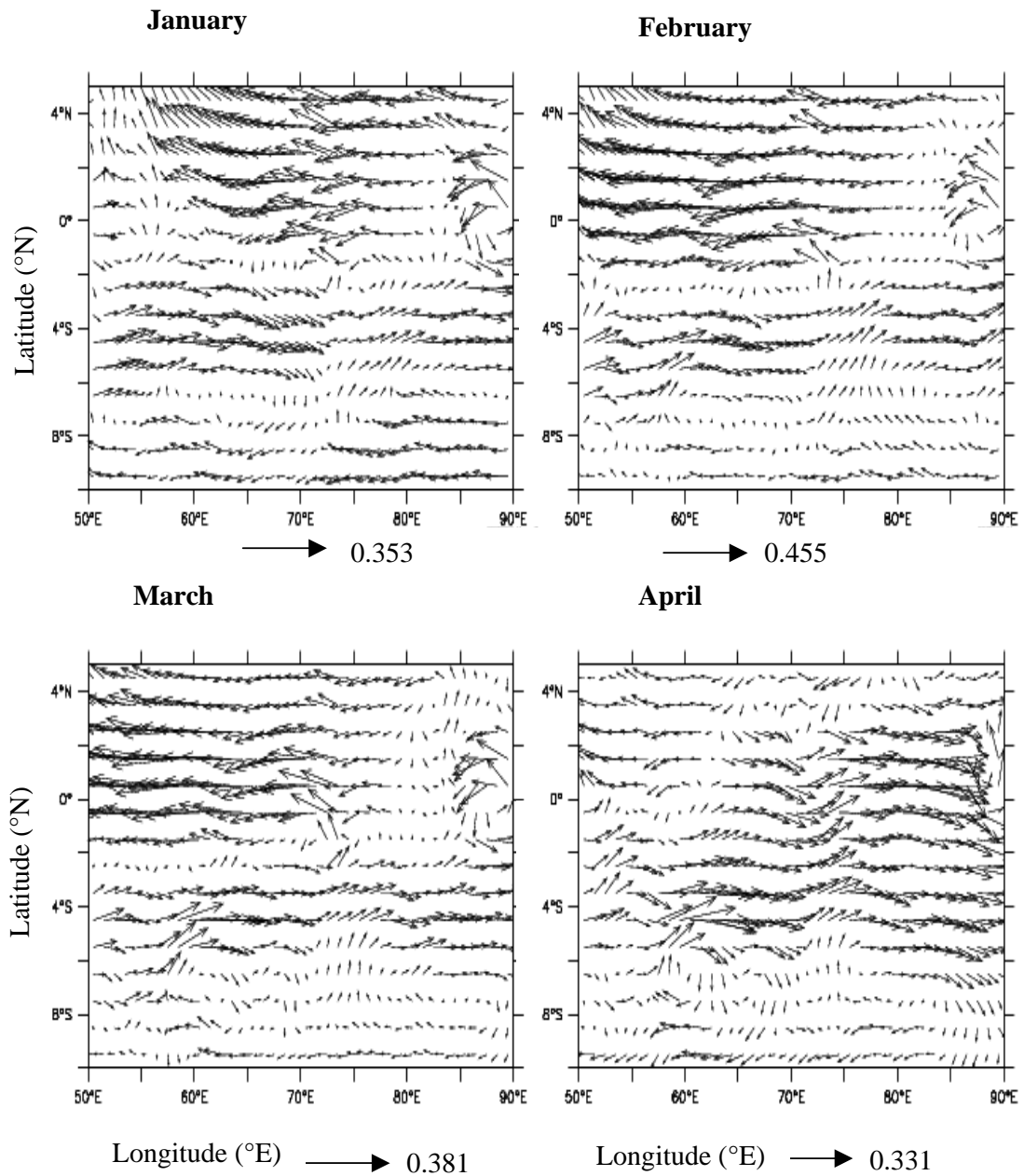


Fig.35 Surface current distribution during January, February, March and April

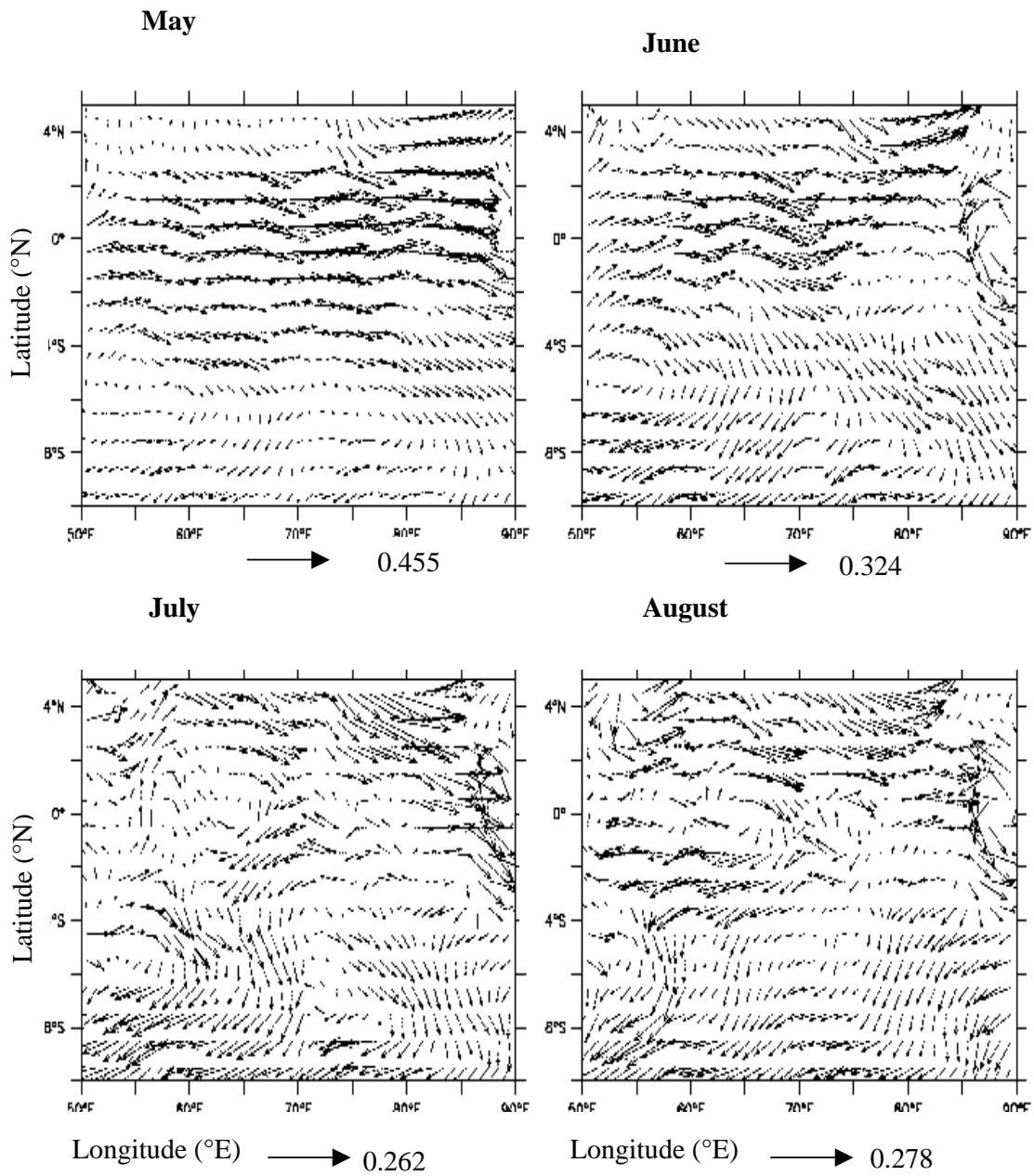


Fig.36 Surface current distribution during May, June, July and August

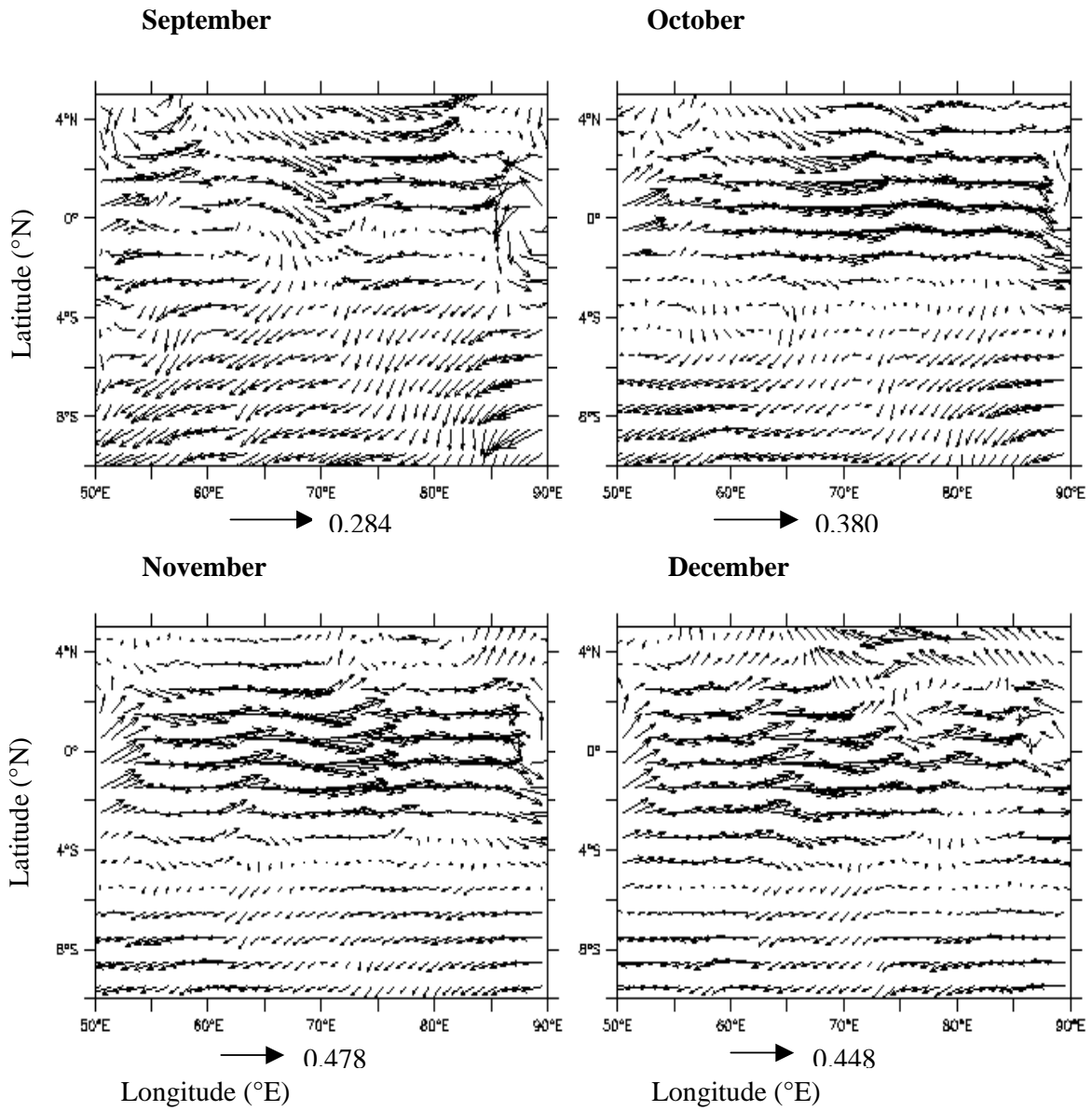


Fig.37 Surface current distribution during September, October, November and December

## **3.2 Seasonal cycle of atmospheric parameters**

### **3.2.1 Seasonal cycle of Air temperature**

Air temperature in January and February varied between 25 to 28°C, with colder air mass close to the western boundary and near Indo-Sri Lanka region (Fig. 38). Very cold region near the Java coast appears to be a data error. Atmospheric heating was discernible during March and air temperature attained its peak seasonal value in April when the entire study domain had a temperature in excess of 29°C, except in localized patches of colder air.

Atmospheric heating showed a decrease in May with colder temperature (~27°C) in the southwestern region. This trend continued in June and persisted till September when the temperature dropped to the cold of the seasonal value along the western boundary and in the southwestern parts. The temperature variation was 4°C (24.5°C – 28.5°C). This cooling of atmosphere, in general, must be related to the cloud cover during summer monsoon and in particular along the western boundary must be due to the upwelling of colder waters. The colder air temperature in the southern region west of 70°E must be driven by sensible heat loss due to the shoaling of thermocline under wind-divergence.

In October, the observed warming of air temperature takes place due to secondary heating in fall inter-monsoon (Fig. 40). During November and December the spatial variation of air temperature in the study domain was the least, 1.5°C (26.5°C – 28°C).

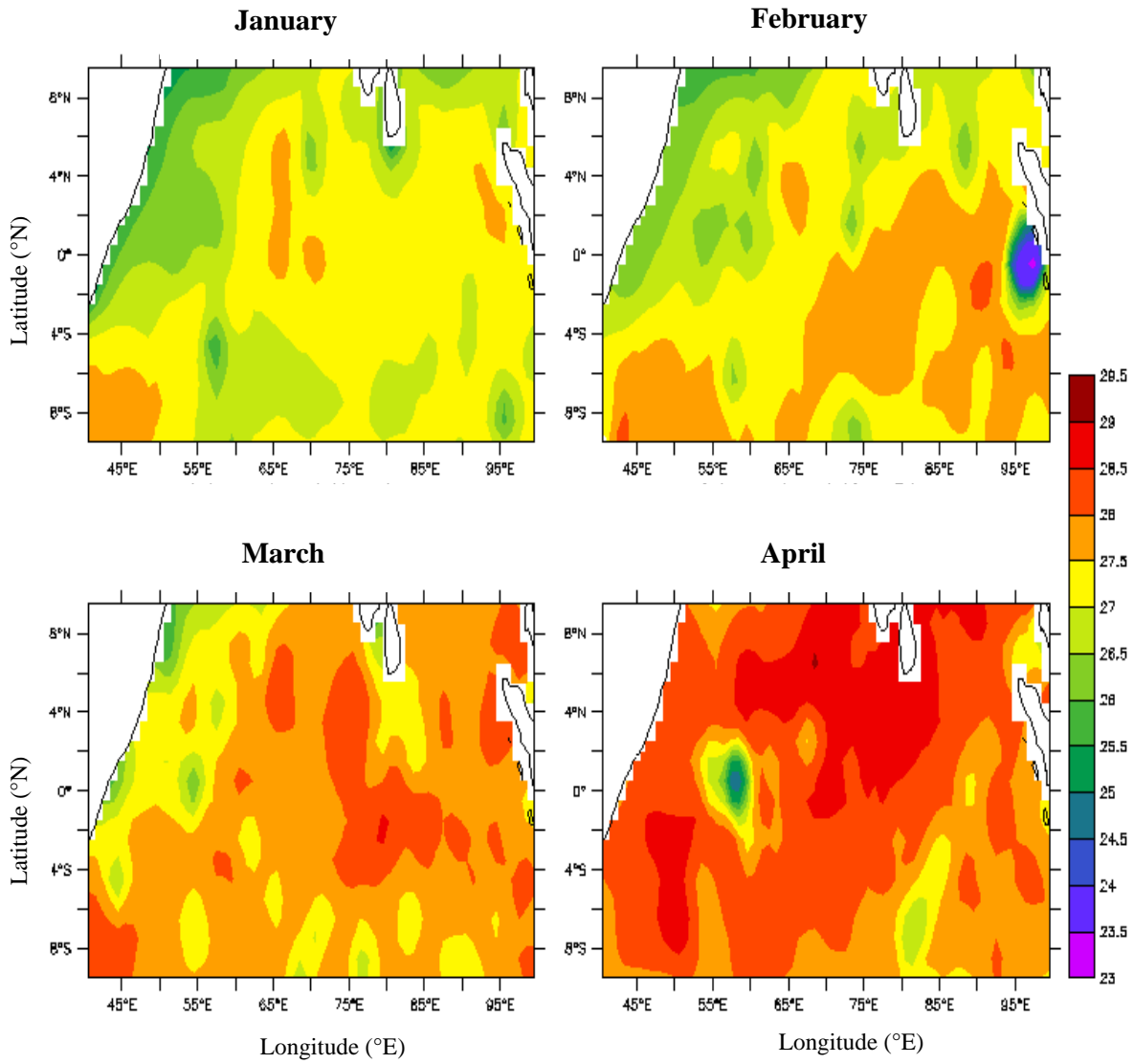


Fig.38 Air temperature (°C) at 10m heights during January, February, March and April.

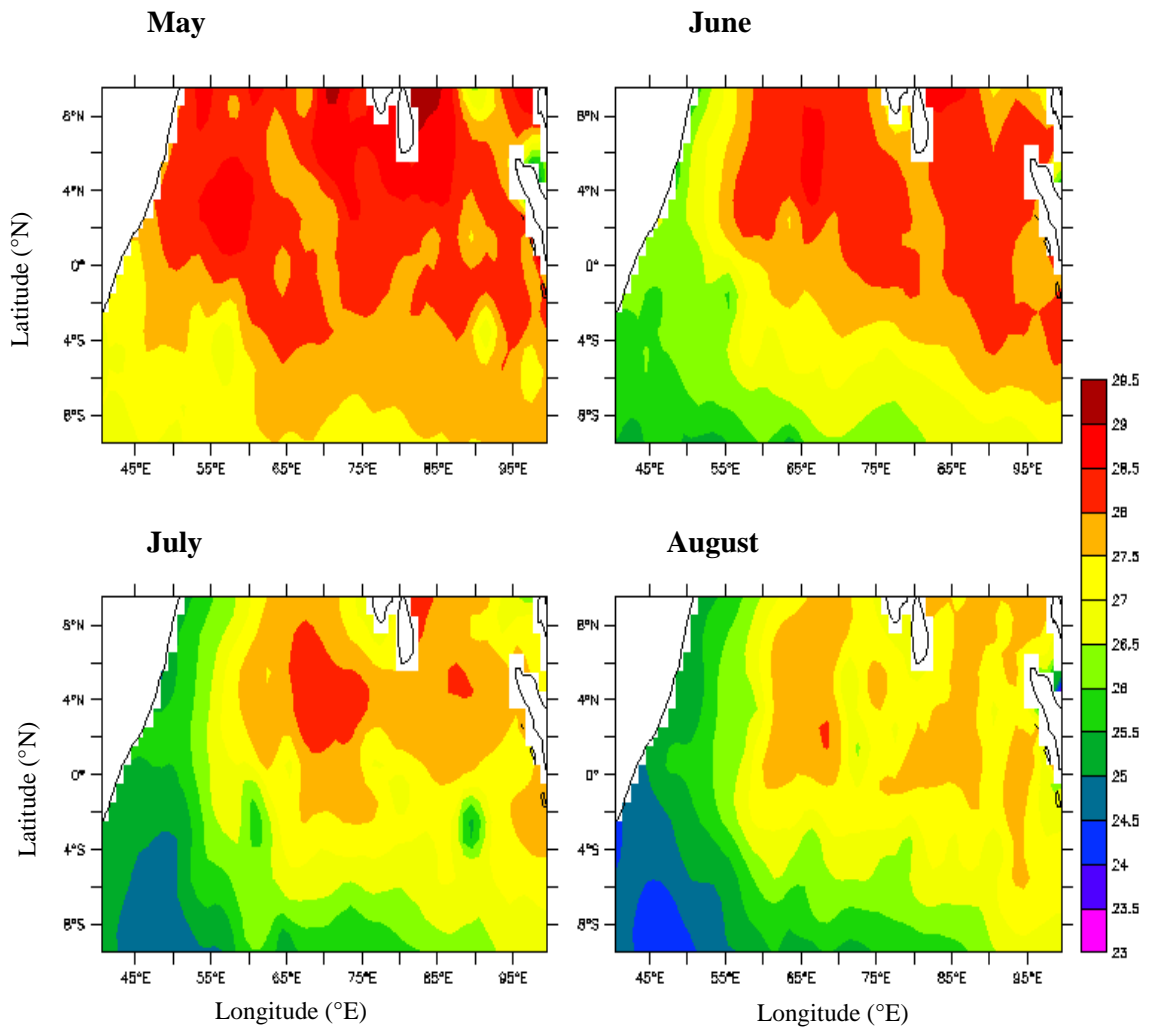


Fig.39 Air temperature (°C) at 10m heights during May, June, July and August.

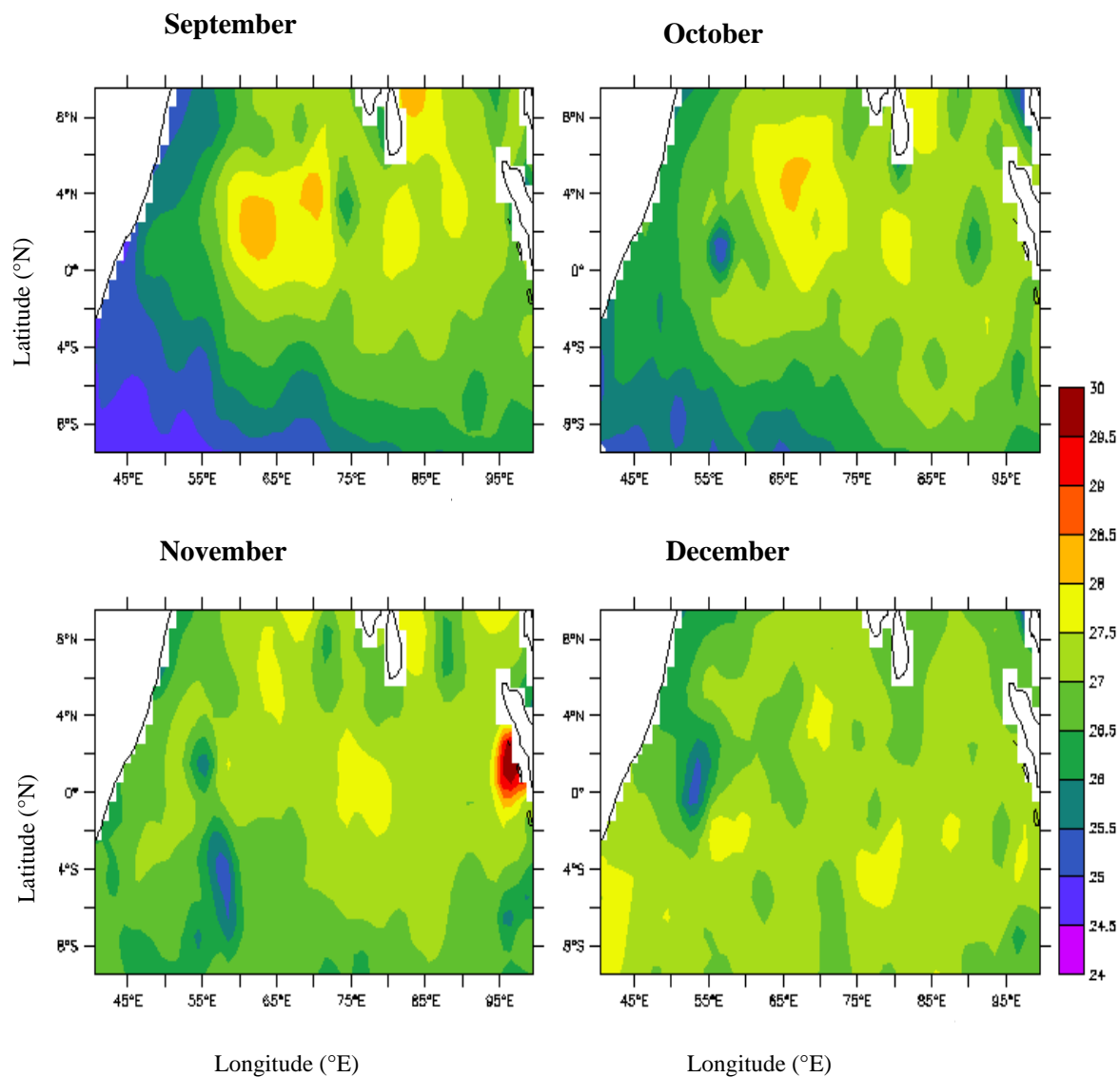


Fig.40 Air temperature (°C) at 10m heights during September, October, November and December.

In summary seasonal cycle of air temperature showed two warming periods one during spring inter-monsoon (29.5°C) and other during fall inter-monsoon (28.5°C). The amplitude of the seasonal cycle of air temperature was about 4°C, while the spatial variation was least during



April ( $1^{\circ}\text{C}$ ) and November ( $1.5^{\circ}\text{C}$ ). The cooling of air temperature during summer near the western boundary was related to sensible heat loss due to the upwelled colder surface waters, whereas that in the south the cooling of air temperature must be linked to the thermocline ridge driven by the divergence in the wind field.

### **3.2.2 Seasonal variation of fresh water flux**

During January, spatial distribution of fresh water flux (E-P) showed a region of intense precipitation, in excess of 2 m per year, in the eastern part which extends towards west in the southern region (Fig. 41). The western region was region of net fresh water loss where evaporation was over 1m per year. The pattern remained more or less similar until April, though the intensity of both net evaporation as well as precipitation showed a decrease. In May the region of net evaporation along the western boundary was the least (Fig. 42). In fact, most of the study domain was under the influence of net precipitation, intensity of which ranged from 1 to 3 m per year. Once again from June to September, an increased net evaporation was noticed in the northwestern region. Note that the entire western region during this period has net evaporation. The region south of peninsular India showed excess precipitation during June to August to the tune of 1-2 m per year. From September to December an increased net precipitation was noticed in the entire eastern region, east of  $75^{\circ}\text{E}$  (Fig.43). This region showed a westward extension in the south with time.

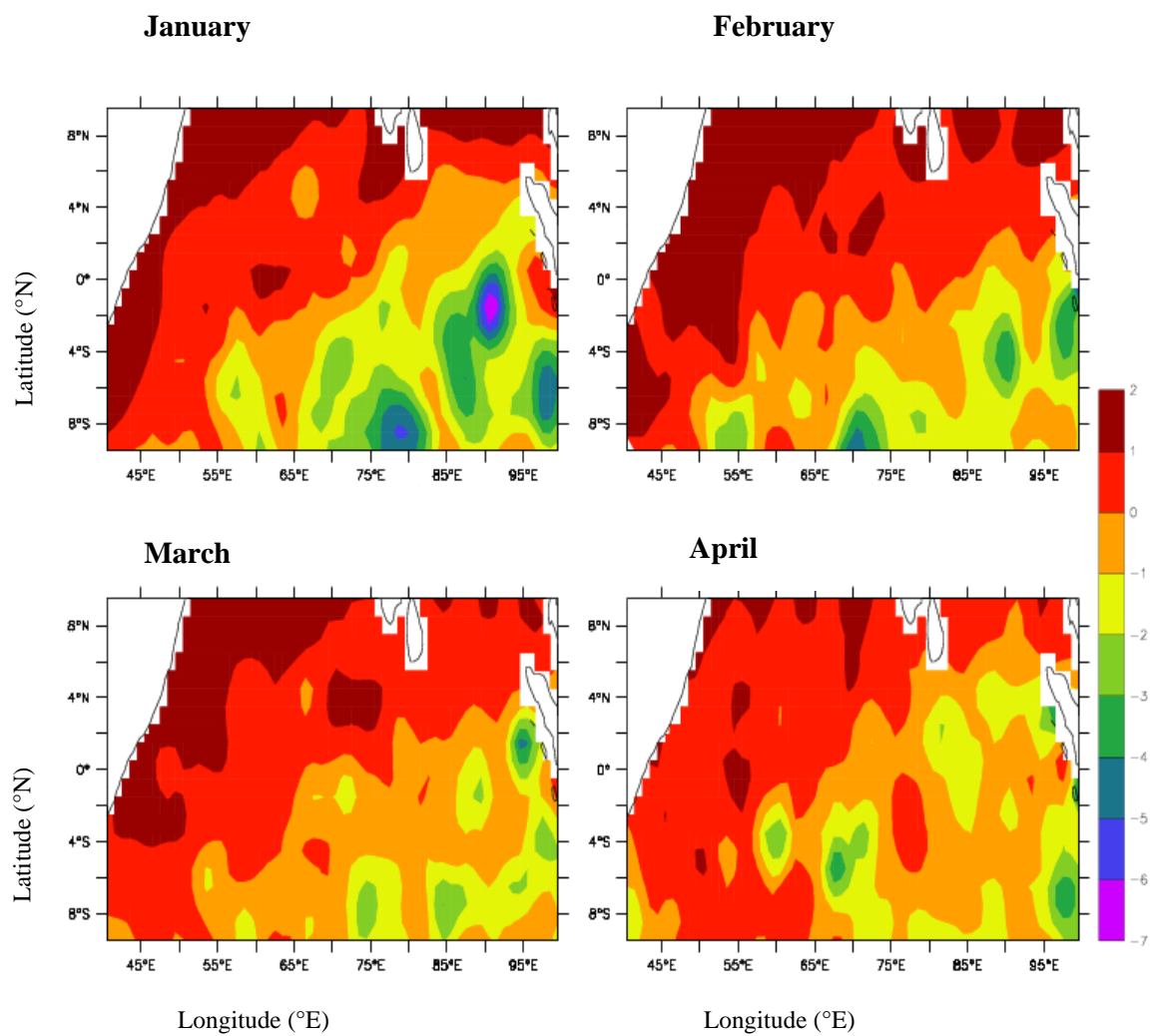


Fig.41 Fresh water flux (E-P) (m/year) during January, February, March and April.

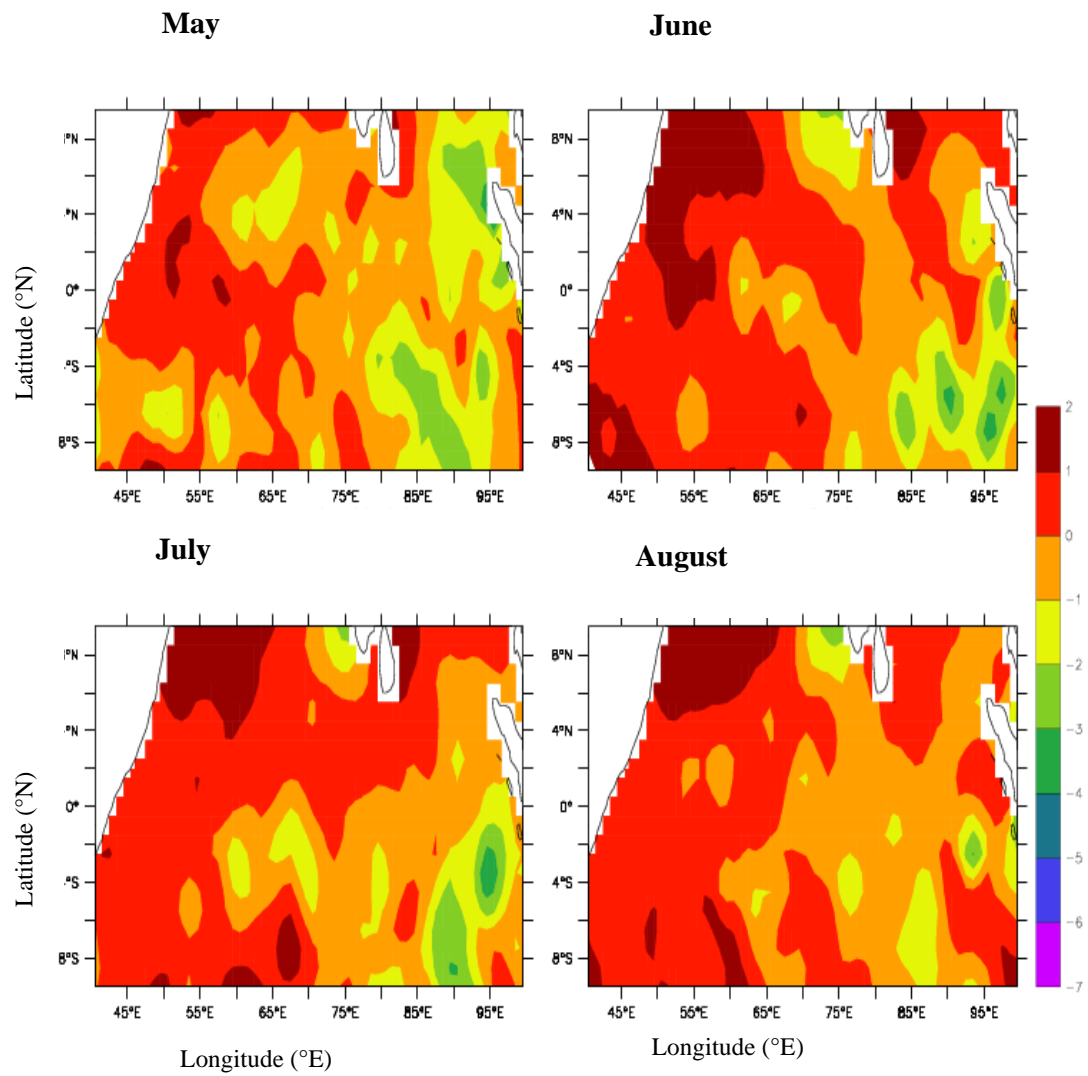


Fig.42 Fresh water flux (E-P) (m/year) during May, June, July and August

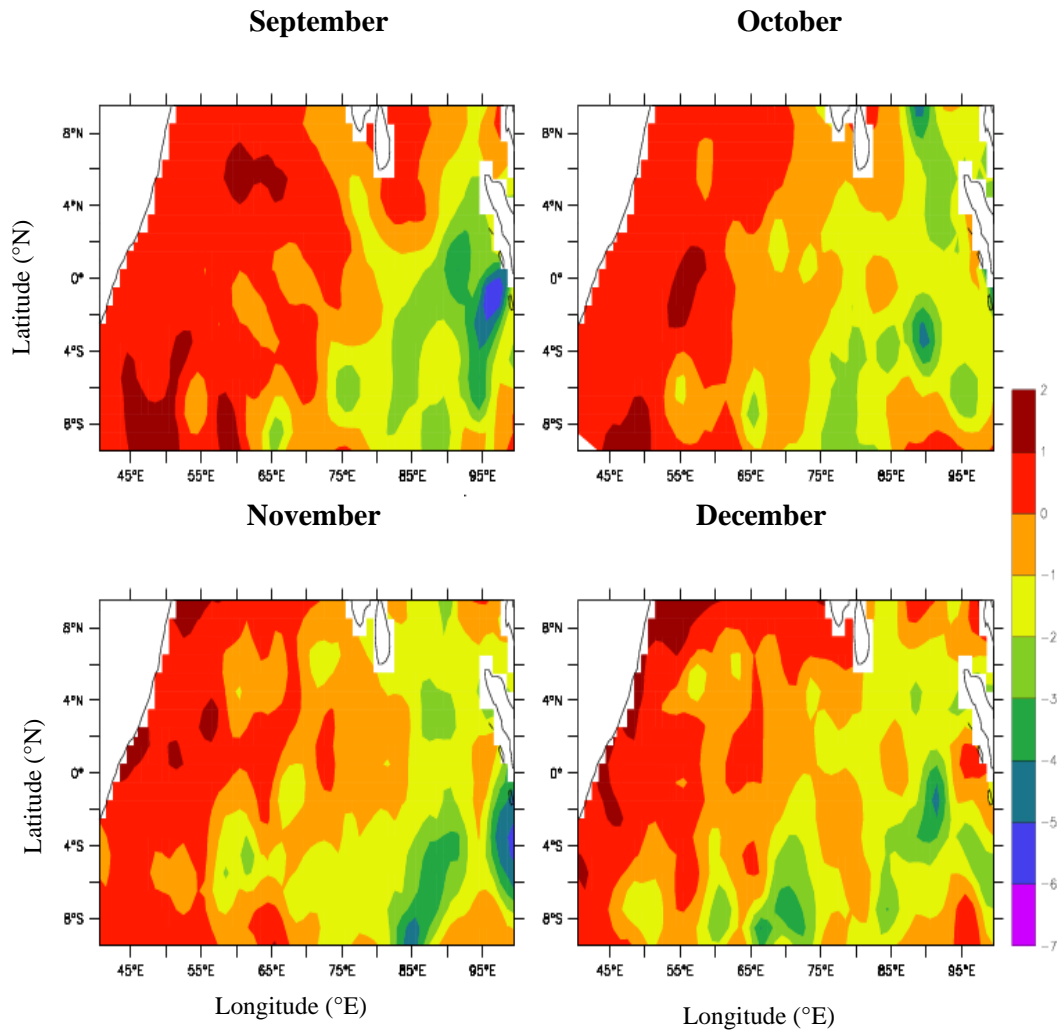


Fig.43 Fresh water flux (E-P) (m/year) during September, October, November and December

In summary, the seasonal cycle of fresh water flux showed that the western EIO perennially lost fresh water while the eastern EIO was a region of net gain. This gain in the eastern region begins in September, peaks in January and begins to decay in March. A region of net precipitation developed south of Indian peninsula in June and continued to exist till August.

### **3.2.3 Seasonal cycle of Net Heat Flux**

The net heat flux showed a region of net heat loss, of about  $30 \text{ W/m}^2$  in the northern region (Fig. 44). For example, in the western region (southern Arabian Sea) the heat loss occurred north of  $4^\circ\text{N}$ , while that in the eastern part (southern Bay of Bengal) was in the north of  $2^\circ\text{N}$ . In the western EIO, south of equator a net heat gain of about  $100 \text{ W/m}^2$  was noticed which reduced its magnitude towards east. In February, the entire study domain showed net heat gain, while the net gain south of equator showed increase in magnitude. In March and April, the net heat gain intensified further with highest values of  $\sim 160 \text{ W/m}^2$  towards the western region. With the onset of southwest monsoon winds, and associated cloud cover, the net heat gain showed drastic reduction, progressively from May to July (Fig.45). The southern region, south of  $5^\circ\text{S}$  showed a net heat loss of about  $30 \text{ W/m}^2$  which may be due to intense evaporation as seen from the E-P values. There was also a small region of net heat loss in southern part of the Arabian Sea in June which was due to evaporative cooling. Along the western boundary, especially near the Somali region, a net heat gain was noticed during June which peaks in September (Fig. 46). In November and December, this region of net heat gain moves and extends towards southeast. The southward movement is linked to the movement of sun towards southern hemisphere at this period. In

December a region of net heat loss starts developing in the north, north of 6°N.

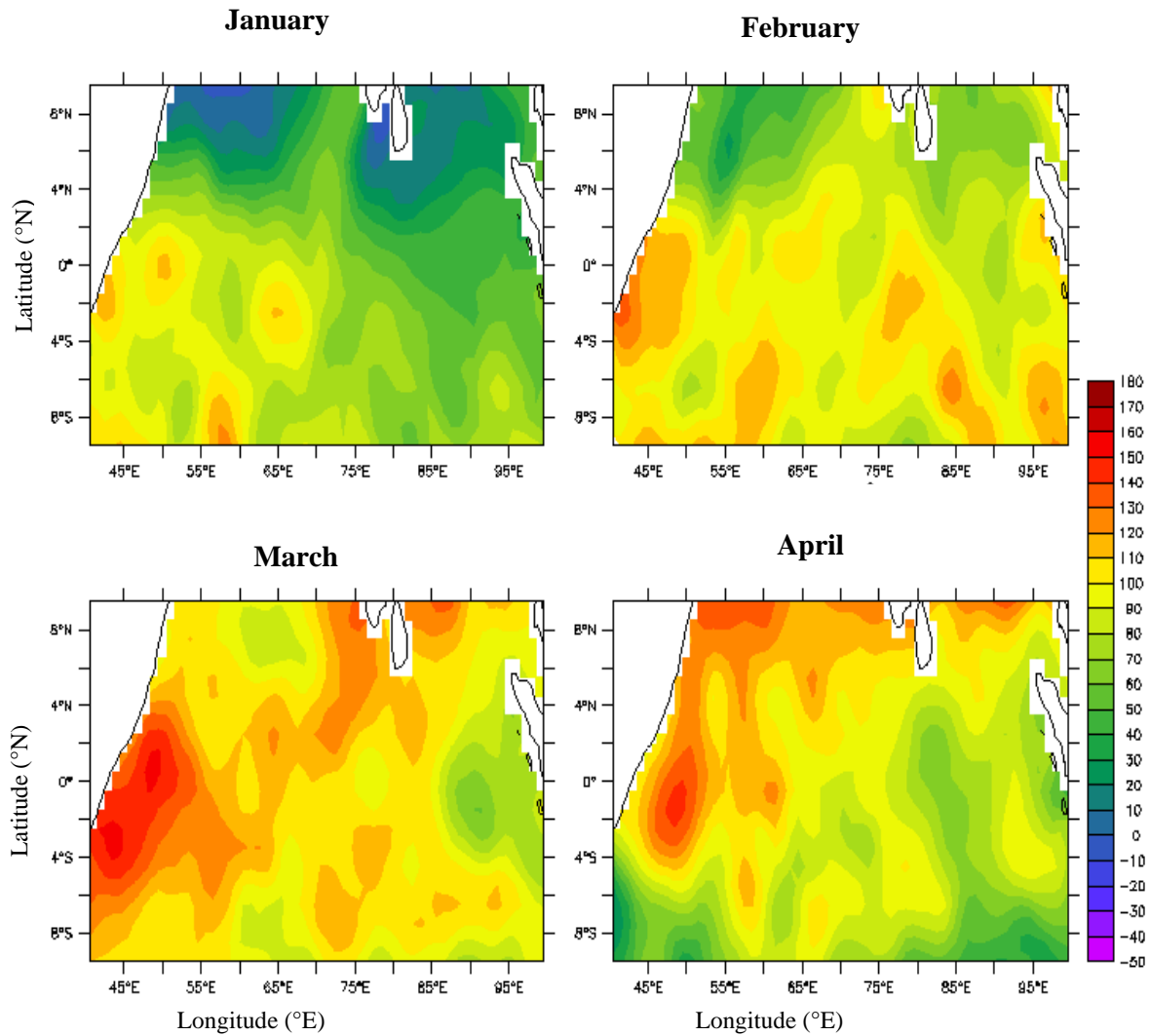


Fig.44 Net heat flux ( $\text{W/m}^2$ ) during January, February, March and April.

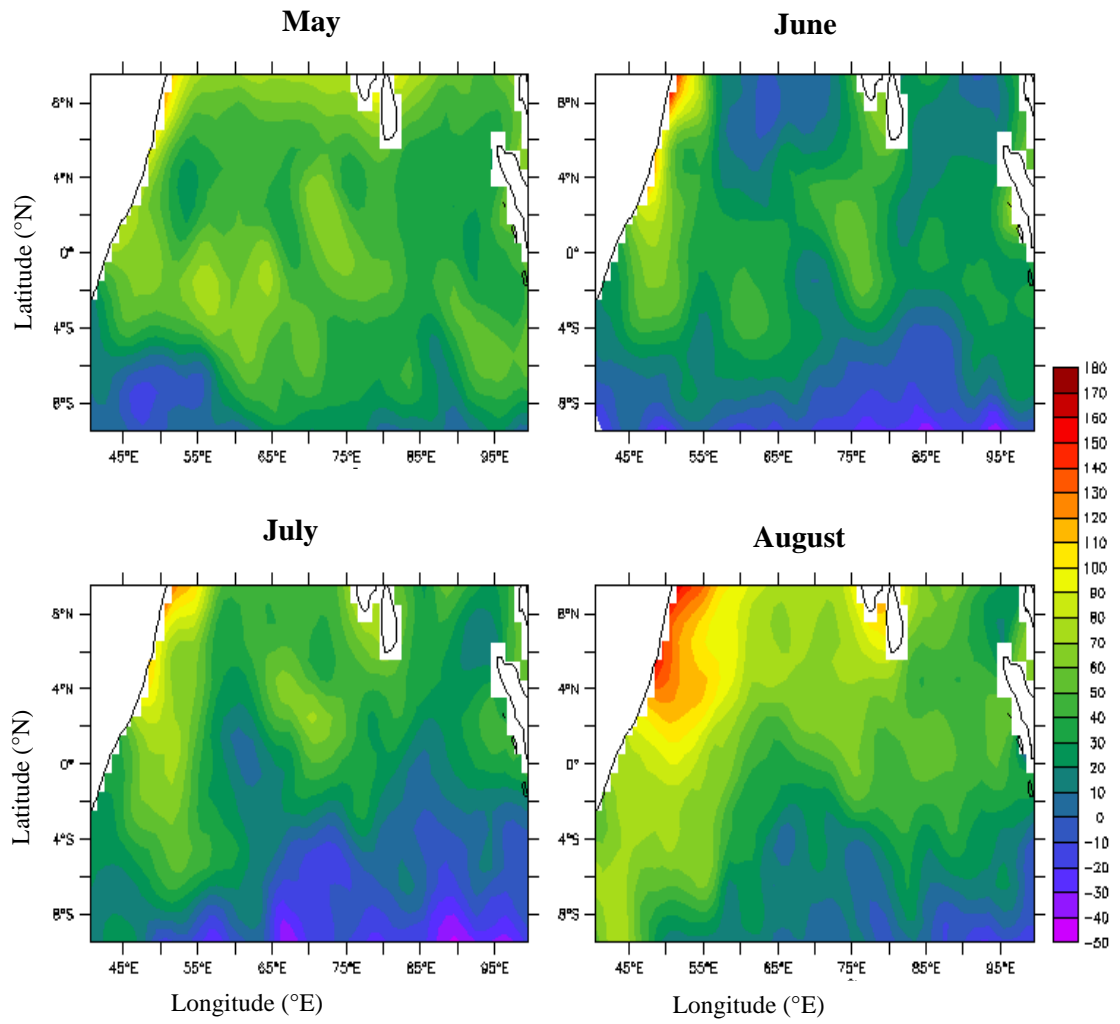


Fig.45 Net heat flux ( $\text{W/m}^2$ ) during May, June, July and August.

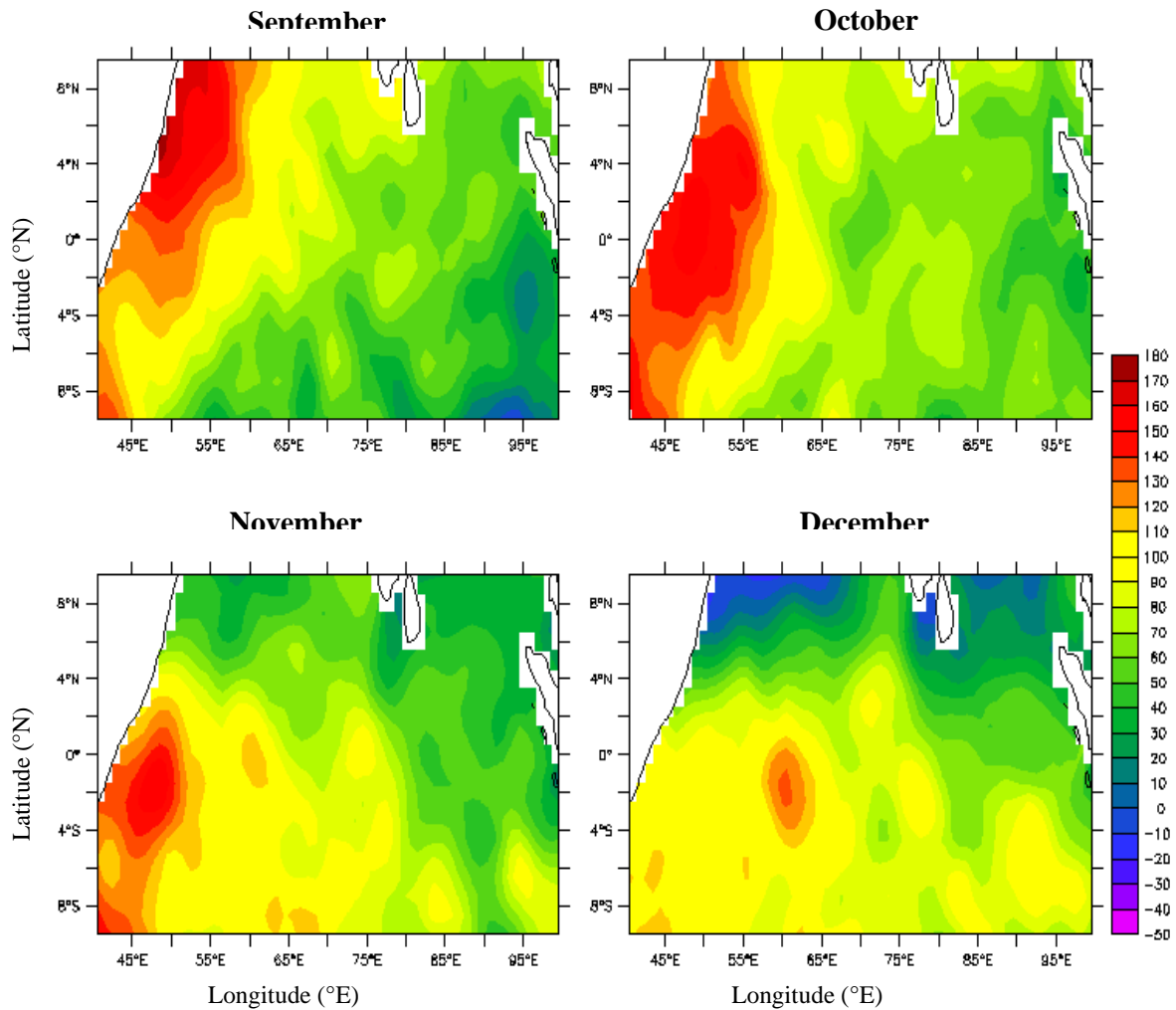


Fig.46 Net heat flux ( $\text{W/m}^2$ ) during September, October, November and December

In summary, the seasonal cycle of net heat flux showed that the entire region gains heat during February to April and in October-November. The southern parts of the Arabian Sea as well as the Bay of Bengal showed net heat loss during December and January. There was also net heat loss due to evaporative cooling in the southern Arabian Sea during June. With the onset of southwest monsoon wind and cloud cover, the net



heat gain decreased in May and June. The western boundary, especially the Somali region showed a strong heat gain in July which peaked in September. The heat loss in the south during June to August may arise due to two mechanisms - the evaporative cooling driven by strong southerly trade winds as well as the sensible heat loss due to the thermocline ridge driven by wind divergence.

### **3.2.4 Seasonal cycle of Scalar wind**

During January high wind speed were seen along the Somali coast ( $>6.2\text{m/s}$ ) and also in the northeastern region ( $\approx 5.8\text{m/s}$ ) especially near the southeastern coast of India and Sri Lanka (Fig. 47). Low wind speed was seen in the southwestern coast of India and near the Sumatra coast. Pattern was much similar in February, except that the wind speed in the northeastern region encompassing Indo-Sri Lanka region showed a decrease. In March and April, the wind speed further decreased and was the least of all months. With the onset of southwest monsoon, the wind speed showed dramatic increase in May ( $12\text{-}14\text{ m/s}$ ) (Fig.48). The core of high wind speed indicated the axis along which the southerly trade winds crossed the equator and moved as strong southwesterly monsoon winds towards the north. During June to August the northern region, especially western part ( $\sim 15\text{ m/s}$ ), showed stronger winds, while the southern region became progressively weaker. In October the wind speed was once again less, but towards the south it showed an increase (Fig. 49). In fact, the southern region, south of  $5^{\circ}\text{N}$ , showed a gradual strengthening of winds from August, which peaked in October and decayed by December. In the northern region, north of equator, the wind speed showed an increase in

November and reached the speed of 7 m/s by December. This was the northeast trade winds of continental origin.

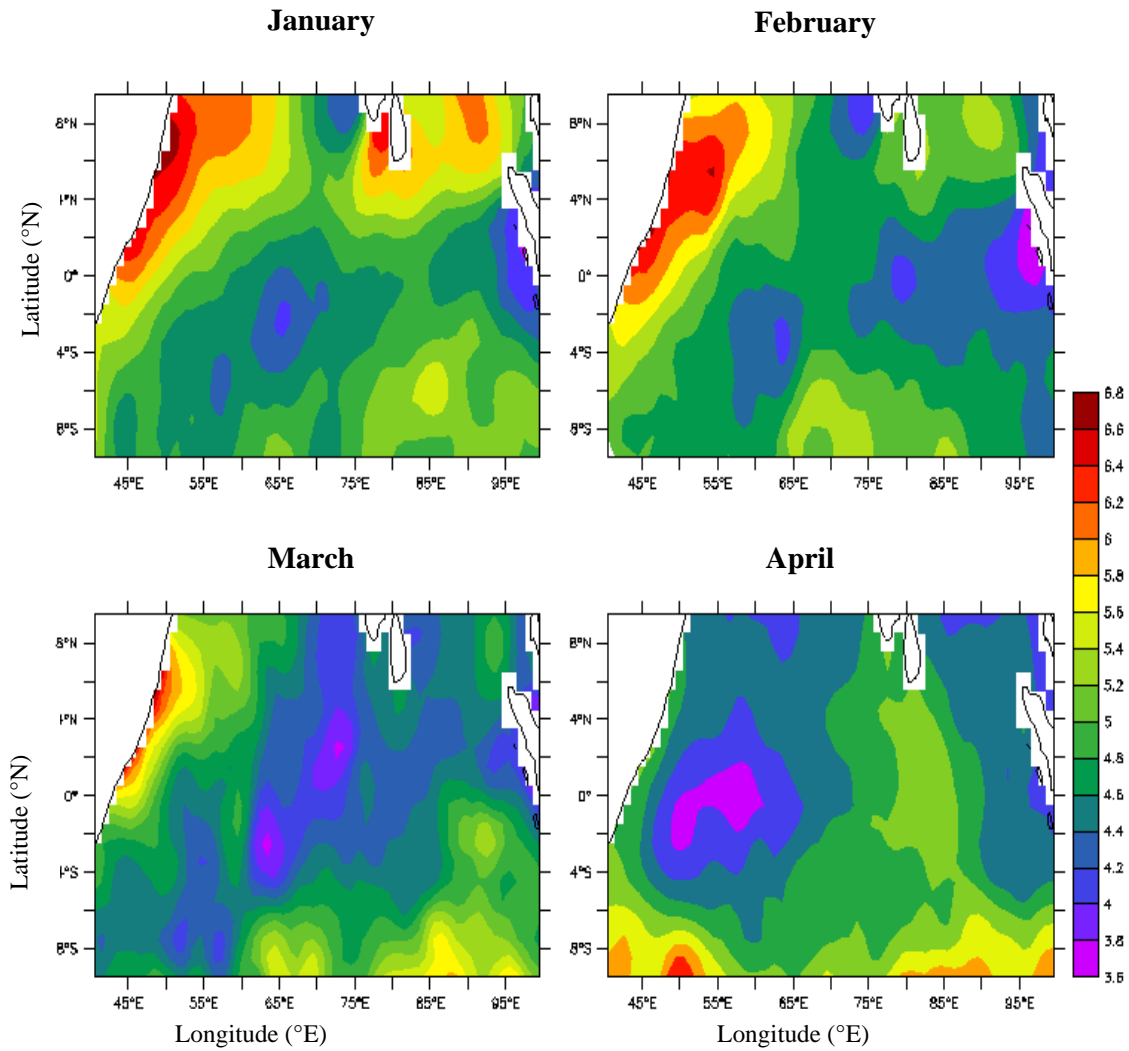


Fig.47 Wind speed (m/s) during January, February, March and April.

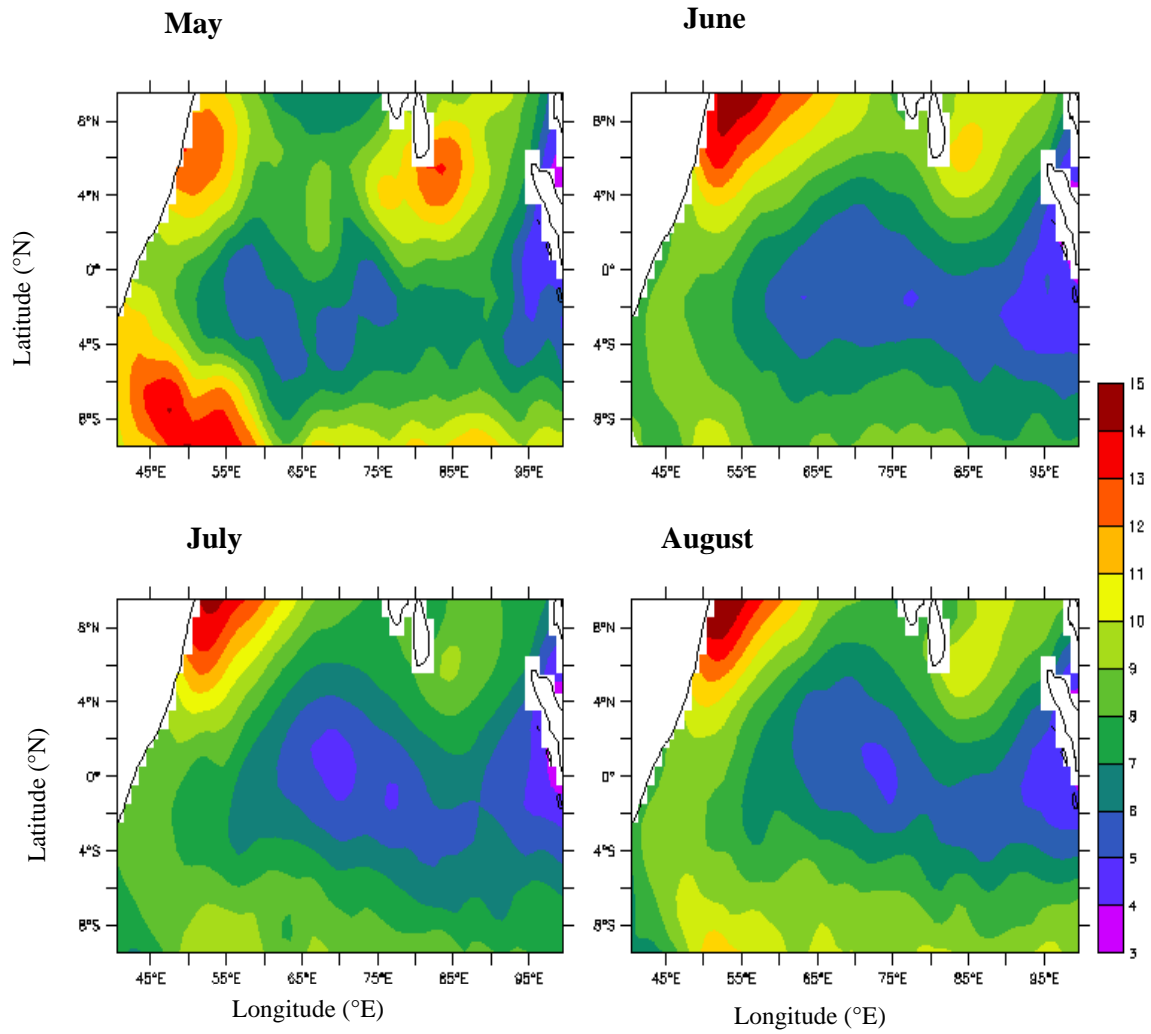


Fig.48 Wind speed (m/s) during May, June, July and August.

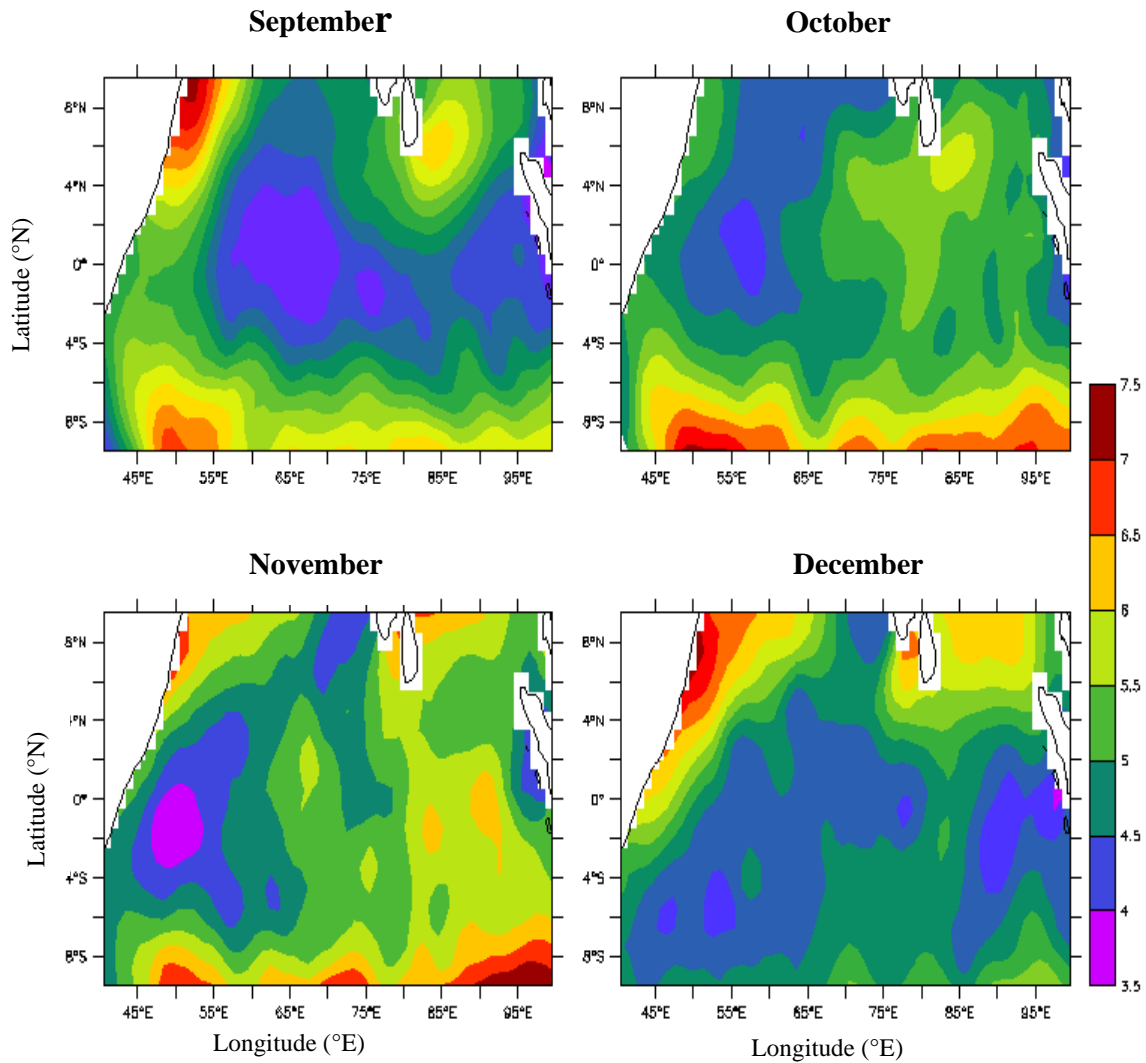


Fig.49 Wind speed (m/s) during September, October, November and December.

In summary, the seasonal cycle of scalar wind showed two periods of strengthening one during summer monsoon (15 m/s) and the other during winter (~7 m/s). In the spring and fall inter-monsoons the wind speeds

were the least ( $\sim 3-4$  m/s). The southern region, south of  $5^{\circ}\text{S}$ , showed an intensification of speed during August to November.

### **3.2.5 Seasonal cycle of wind stress curl**

The spatial distribution of wind stress curl showed two distinct regions of positive and negative curl during January (Fig. 50). Positive curl ( $1 - 1.5$   $\text{N/m}^3$ ) was noticed around Indo-Sri Lanka region and eastern part of the southern region south of  $6^{\circ}\text{S}$ . The negative curl ( $1 - 1.5$   $\text{N/m}^3$ ) was seen in the northern Sumatra coast. Zero wind stress curl was observed around the equatorial region. During February, the zero curl region expanded away from the equatorial region. A negative was seen along the western boundary, except in the north, and also off Sumatra and extended towards southwestward. During March and April, the regions of negative curl reduced in its spatial extent and a region of strong positive curl ( $0.5 - 1.5$   $\text{N/m}^3$ ) was located south of  $4^{\circ}\text{S}$ . By May (Fig.51) a region of negative curl was seen around Indo-Sri Lanka and persisted until September (Fig.52). During this period, a strong positive curl ( $3 - 5$   $\text{N/m}^3$ ) developed along the western boundary, associated with strong southwest monsoon winds (Fig.51). In August the entire study domain, except east of Sri Lanka and southwestern corner, had positive curl. By September, the strength of the positive curl along the western boundary weakened and disappeared in November (Fig.52). The negative curl region seen around Indo-Sri Lanka showed an expansion in its spatial extent from October. During November-December the entire region north of  $4^{\circ}\text{S}$  had negative curl, except a small patch of positive curl off peninsular India.

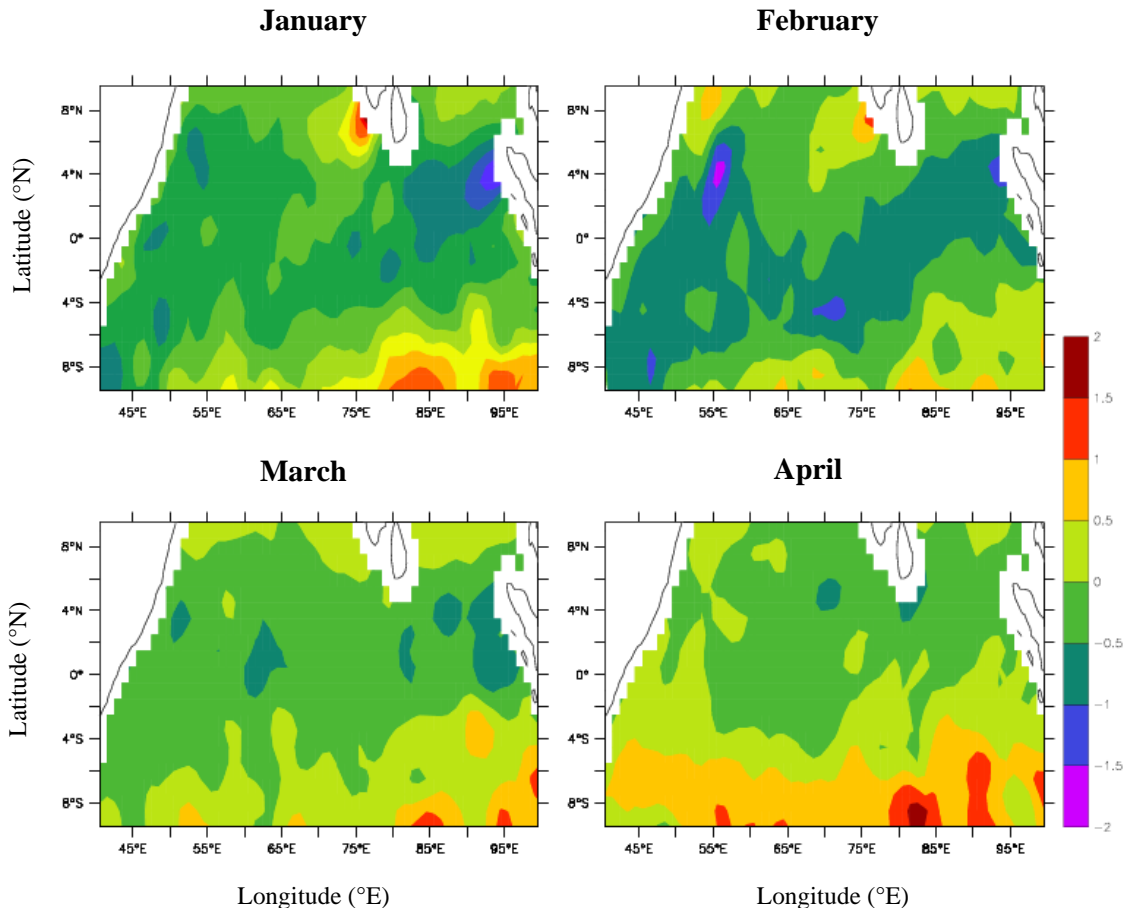


Fig.50 Wind stress curl ( $\text{N/m}^3$ ) during January, February, March and April

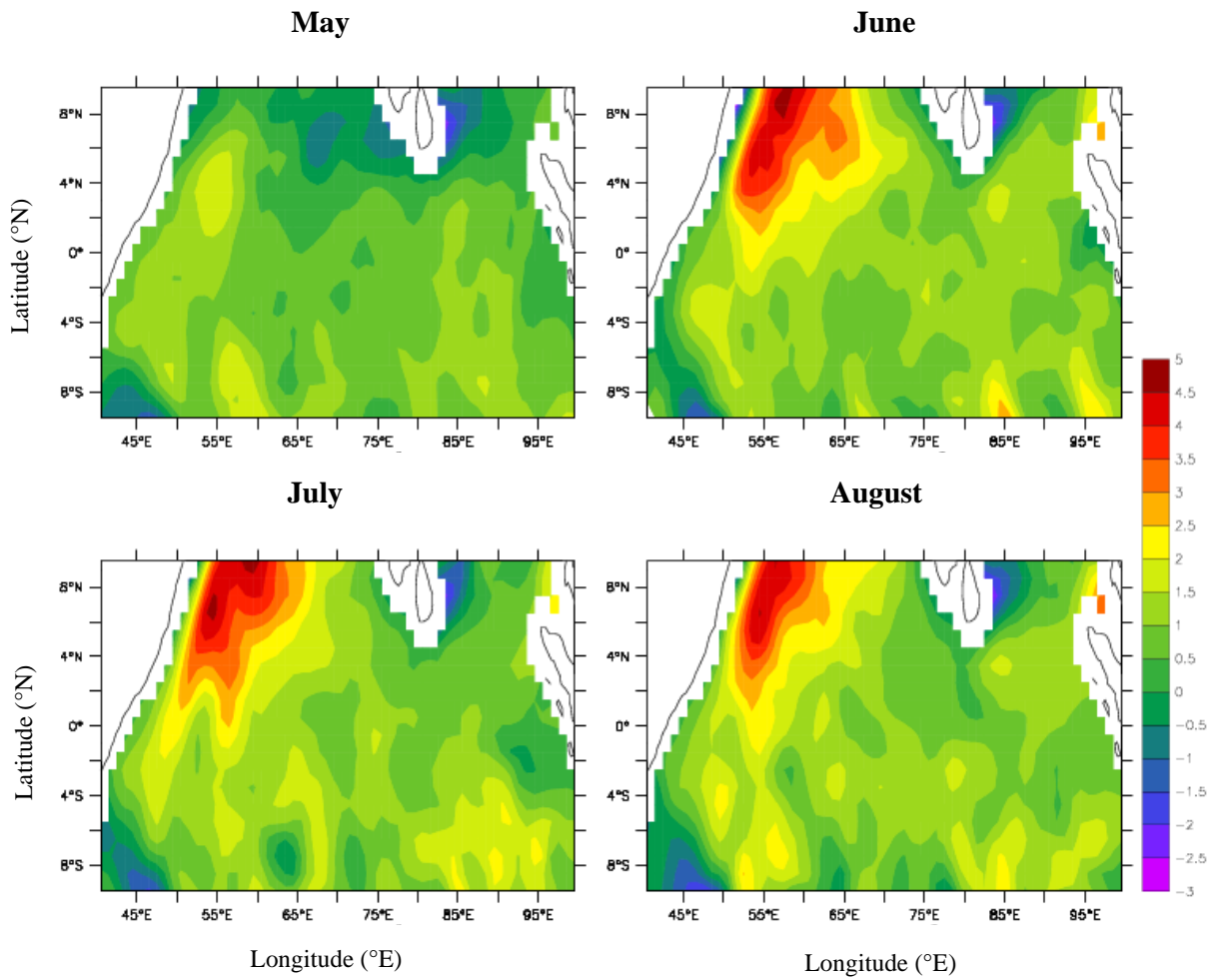


Fig. 51 Wind stress curl (N/m<sup>3</sup>) during May, June, July and August

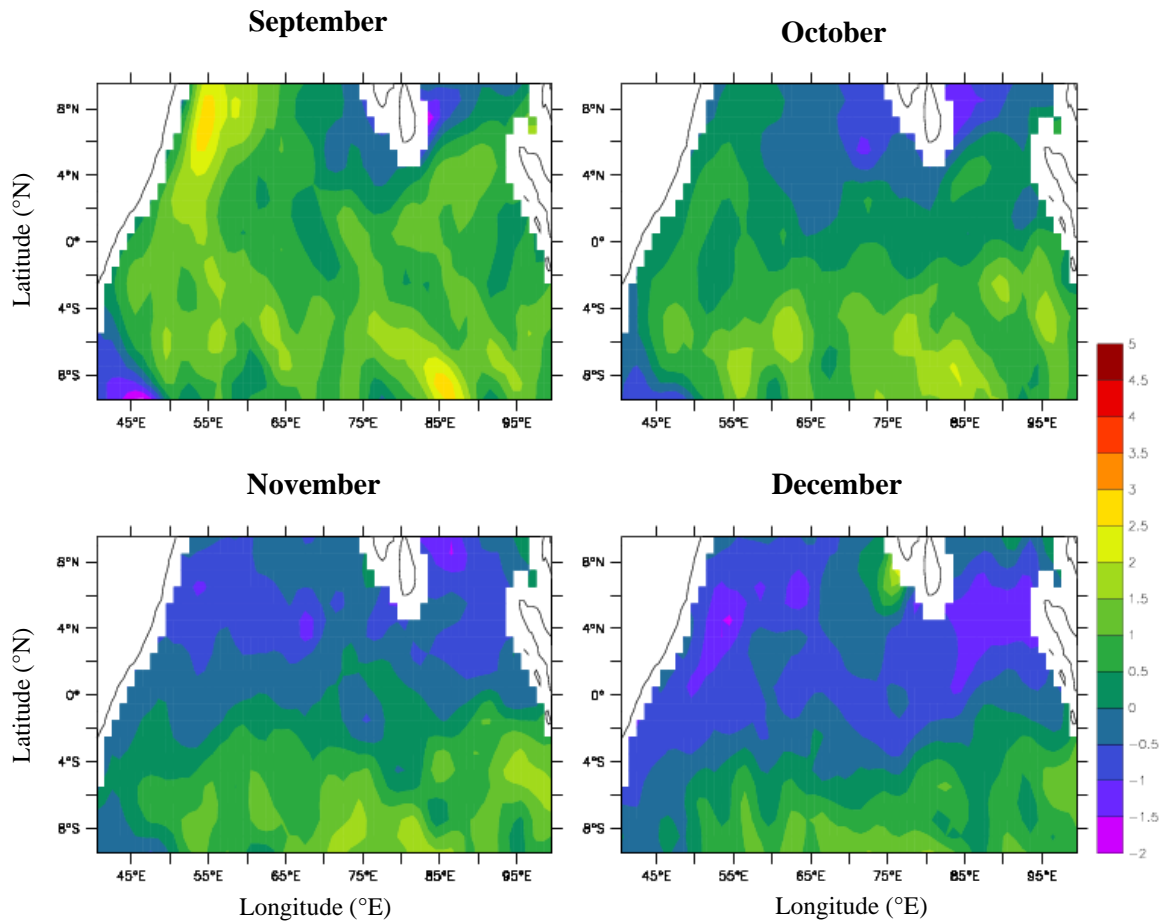


Fig. 52 Wind stress curl ( $N/m^3$ ) during September, October, November and December

In summary, the seasonal cycle of wind stress curl showed the development of positive curl along the western boundary with the onset of south west monsoon winds which attained its maximum strength in July and decayed by October. During winter, a region of positive curl developed south of Indian peninsula in December, peaked in January and disappeared by April. During summer, however, a negative curl was seen



developing east of Sri Lanka in May and persisted till September. In winter the entire northern region, north of equator was under the influence of negative curl.

# **Chapter 4**

## **Summary and Conclusion**

Equatorial regions are special areas of the world ocean where intense air-sea interaction takes place and hence the ocean is tightly coupled to the atmosphere. Among the three equatorial regions, the Equatorial Indian Ocean (EIO) has some special feature that makes it unique. The semi-annual reversal of equatorial winds north of equator and associated changes in surface currents, warmer eastern region, higher precipitation and perennial presence of barrier layer, and lack of equatorial upwelling. In spite of its very special characteristics compared to equatorial Pacific or Atlantic, EIO is the least studied region. This is primarily due to the scarcity of observation. With the advent of ocean remote sensing technique the availability of high-resolution data, both space and time, has increased and it is now possible to address several aspects of Indian Ocean. An example of this is the recent discovery of Indian Ocean Dipole (IOD) Mode that produces anomalous atmospheric and oceanic condition, and has the potential to influence regional climate. In addition to this, the deployment of ARGO profiling floats in the Indian Ocean dramatically increased the availability of vertical profiles of temperature and salinity. This allows one to address the variability of EIO on a seasonal scale better than before. This has motivated the present work.

The present work aims at understanding the upper ocean variability of the EIO on a seasonal scale and then to explore the atmospheric forcing responsible for it. The specific objectives are:

4. Seasonal variability of sea surface temperature, sea surface salinity, mixed layer depth, barrier layer depth and depth of mid-thermocline.
5. Seasonal variability of net heat flux, fresh water flux, and momentum flux.

6. What controls the mixed layer depth and barrier layer depth in the EIO?

To achieve the above objectives, the Equatorial Indian Ocean between latitude 10°S-10°N and longitude between 40°E-110°E was selected for the present study. For the study, both *in situ* data and remote sensing data were used. The oceanographic data on temperature, salinity were obtained from 3 sources – World Ocean Database 2005 (WOD05) which contains CTD data during the period 1970-2000, Responsible National Oceanographic Data Centre (RNODC) which contains CTD data collected by Indian research vessels during the period 1983-2004, and ARGO data during 2000 to 2006. In addition to this, the monthly mean ocean surface current (Ocean Surface Current Analysis- Real time - OSCAR) data during 1992 to 2006 was also used. The atmospheric data on air temperature, wind speed and direction, net heat flux, wind stress, and fresh water flux used for this study was derived from Southampton Oceanography Center. The dataset is a modified version of the Comprehensive Ocean - Atmosphere Dataset (COADS) of marine meteorological reports spanning the period 1980 - 1993, which has been corrected for biases arising from variations in observing procedure.

The hydrographic data on temperature and salinity were subjected to the following quality control procedures to obtain quality data. First, duplicate profiles, as well as those with obvious errors, were excluded by visual inspection. Then, profiles with depths less than 50m were eliminated. The total number of CTD data after quality control was 3782 while that from ARGO was 13069. This quality-controlled data was binned into a 1-degree longitude by 1-degree latitude grid (1°×1°) within the study domain and were further used to calculate the density values.

From each of this quality controlled profiles, sea surface temperature (SST) and sea surface salinity (SSS), mixed layer depth (MLD), barrier layer thickness (BLT) and mid-thermocline depth (D20) were determined in each  $1^{\circ}\times 1^{\circ}$  grid. MLD was determined as the depth at which the density ( $\sigma_t$ ) exceeds  $0.2 \text{ kg/m}^3$  from its surface value, while BLT was determined by subtracting the MLD from the isothermal layer. In the present study, isothermal layer is defined as the depth at which the temperature decreases from SST by  $1^{\circ}\text{C}$ . Depth of  $20^{\circ}\text{C}$  isotherm was taken as mid-thermocline depth. From these values monthly mean SST, SSS, MLD, BLT and D20 were calculated for each of the  $1^{\circ}\times 1^{\circ}$  grid.

The seasonal cycle of SST showed that the highest SST occurred in spring inter-monsoon ( $30^{\circ}\text{C}$ ), followed by fall inter-monsoon ( $29^{\circ}\text{C}$ ), when the entire study domain showed the least spatial variability of  $2^{\circ}\text{C}$ . These two periods coincided by the primary and secondary heating as inferred from the net heat flux. The coldest SST was seen in summer ( $<25.5^{\circ}\text{C}$ ), followed by winter ( $<26.5^{\circ}\text{C}$ ) near the western boundary and southern part of peninsular India (only during summer). Though the spatial variability of SST during summer as well as winter was about  $4^{\circ}\text{C}$ , the SST gradient near the western boundary was large in summer. In general, western EIO was colder than eastern EIO in any given season, and the SST in the eastern EIO was always  $>29^{\circ}\text{C}$ .

The surface salinity distribution clearly demarcated two regimes – the high salinity western region and the low salinity eastern region. The high salinity waters in the western region were partly of local origin where the evaporation exceeds precipitation and partly derived from the high salinity Arabian Sea water. The low salinity waters in the eastern region were derived partly from the low salinity Bay of Bengal waters and partly

from the low salinity Indonesian through flow. The central EIO was the region of mixing of high salinity waters of western origin and low salinity waters of eastern origin. The advection of high salinity waters begins during summer monsoon which get intensified in fall-intermonsoon expanding towards south. During winter it recedes, and its region of influence was the least in spring-intermonsoon. This seasonal cycle of advection of high salinity waters from the Arabian Sea was linked to the direction of flow of zonal currents. During summer monsoon the IMC carried the high salinity waters from western EIO towards east which continued till late fall-intermonsoon. As, the winter monsoon sets in, the low salinity waters of the Bay of Bengal origin spreads towards further west from the eastern boundary by the NEC, and pushes the high salinity waters towards the west. In the north, intrusion of Bay of Bengal waters into the Arabian Sea was also seen during winter. In the south, Indonesian through flow was seen as spreading of low salinity waters near  $10^{\circ}\text{N}$ .

The seasonal cycle of MLD showed distinct feature which was related to the net heat, fresh water and momentum flux, and also with processes of upwelling. In all seasons southwestern region (south of  $2^{\circ}\text{S}$ ,  $40\text{-}50^{\circ}\text{E}$ ) showed comparatively high MLD ( $> 35\text{ M}$ ), while in the northwestern region deep MLD was seen during summer and winter seasons and shallow MLD during spring and fall seasons. But in all seasons, eastern boundary along Sumatra-Java region showed shallow MLD ( $\approx 25\text{m}$ ), so also the northeastern part, as well as the Indo-Sri Lanka region. The shallow MLD in summer in the Indo-Sri Lanka region was driven by the upwelling while that off African coast during fall inter-monsoon was due to eastward extension of the upwelling zone. The deeper MLD in the western region in summer and winter showed the role of wind-driven mixing of high salinity waters where stratification was less. In contrast, the shallow MLD in the eastern region showed the role of fresh water

which induced strong stratification to the water column. The deep MLD in spring inter-monsoon along the equator indicated the sinking associated with the eastward moving Wyrtki jet. When it encounters the eastern boundary, the subsequent flow towards north and south give rise to upwelling, as was noticed in the form of shallow MLD near the Java-Sumatra region in spring inter-monsoon. Thus, the seasonality in the mixed layer depth showed close coupling between the processes of upwelling and also momentum flux. The positive momentum flux and associated divergence gave rise to shallow MLD while the negative flux and convergence lead to deep MLD. This showed the control of wind in regulating the mixed layer. MLD also responded with the fresh water flux, the region of negative fresh water flux were the region of shallow MLD indicating the fresh water control of MLD. The deep MLD in the equatorial region during spring and fall inter-monsoons when the net heat flux is positive shows that during this period of heating, the mixed layer is controlled not by heat flux but by the ocean dynamics such as strong eastward jet.

The seasonal cycle of barrier layer thickness showed strong relationship with the distribution of sea surface salinity. In general, the region of low salinity coincided with the region of thick barrier layer. Two regions of thick barrier layer were found during fall and winter, one near the Indo-Sri Lanka and the other in the eastern EIO. Both of these regions showed strong link to fresh water flux, the former related to advective processes which transports fresher Bay of Bengal waters into the eastern part of the Arabian Sea, while the later to excessive precipitation in this region.

The seasonal variability of the mid-thermocline depth again showed strong connection with wind divergence and upwelling processes. The

deep D20 were seen at the northwestern region through out the year. The shallow D20 south of Sri Lanka during spring inter-monsoon and around Indo-Sri Lanka region were driven by the upwelling processes and associated thermocline changes. Similarly, the shallow D20 region seen in a zonal band south of 5°S, during summer was related to the divergence in the wind field and thermocline ventilation.

The seasonal cycle of surface current reflected the response of upper Ocean to seasonally reversing monsoon winds. During winter when the equatorial Indian Ocean resembled the other equatorial regions of the world ocean, the westward NEC was seen from north of equator up to 2°S, followed by ECC between 2°S and 8°S flowing towards east. South of ECC, the SEC was towards west. In summer, the NEC was replaced by the eastward flowing SMC, which merged with ECC and flows to east as a strong current forced by summer monsoon winds. During spring and fall inter-monsoons when the equatorial winds were westerly, an organized zonal flow was seen only within the equatorial wave guide, 2°N and 2°S, which flows towards the east and was the Wyrтки jet. During this period, current elsewhere in the study domain was weak and unorganized.

The pattern of seasonal variation of air temperature was similar to that of SST. The air temperature showed two warming periods one during spring inter-monsoon (29.5°C) and other during fall inter-monsoon (28.5°C). The amplitude of the seasonal cycle of air temperature was about 4°C, while the spatial variation was least during April (1°C) and November (1.5°C). The cooling of air temperature during summer near the western boundary was related to sensible heat loss due to the upwelled colder surface waters, where as that in the south the cooling of air temperature



must be linked to the thermocline ridge driven by the divergence in the wind field.

The seasonal cycle of fresh water flux showed that the western EIO perennially lost fresh water while the eastern EIO was a region of net gain. This was reflected in the surface salinity where fresher waters were noticed in the eastern region while saltier waters were towards the west. The excess precipitation over evaporation in the eastern region begins in September, peaks in January and begins to decay in March. A region of net precipitation developed south of Indian peninsula in June and continued to exist till August.

The net heat flux showed that the entire region gains heat during February to April and in October-November. The southern parts of the Arabian Sea as well as the Bay of Bengal showed net heat loss during December and January. There was also net heat loss due to evaporative cooling in the southern Arabian Sea during June. With the onset of southwest monsoon wind and cloud cover, the net heat gain decreased in May and June. The western boundary, especially the Somali region showed a strong heat gain in July which peaked in September. The heat loss in the south during June to August may arise due to two mechanisms - the evaporative cooling driven by strong southerly trade winds as well as the sensible heat loss due to the thermocline ridge driven by wind divergence. Thus, the net heat flux showed close correspondence with the distribution pattern of SST as well as temperature.

The seasonal cycle of scalar wind showed two periods of strengthening one during summer monsoon (15 m/s) and the other during winter (~7 m/s). In the spring and fall inter-monsoons the wind speeds were the least

(~3-4 m/s). The southern region, south of 5°S, showed an intensification of speed during August to November.

The wind stress curl showed the development of positive curl along the western boundary with the onset of south west monsoon winds which attained its maximum strength in July and decayed by October. During winter, a region of positive curl developed south of Indian peninsula in December, peaked in January and disappeared by April. During summer, however, a negative curl was seen developing east of Sri Lanka in May and persisted till September. In winter the entire northern region, north of equator was under the influence of negative curl.

Thus, the study of the seasonal cycle of the ocean and atmospheric parameters showed very strong coupling. The seasonal cycle of mixed layer depth and barrier layer thickness were tightly coupled to the variability in the momentum and fresh water fluxes. In fact heat flux had little role in regulating the mixed layer. On the contrary, ocean dynamics played a major role in regulating the mixed layer in the equatorial wave-guide during spring and fall inter-monsoons. Though, the heat flux during both these periods were positive which coincided with the primary and secondary heating, the mixed layer were expected to be thinner, deep MLDs were encountered in the equatorial wave guide. It is quite natural to expect that these seasonal changes in the upper ocean physics will have great impact in the biogeochemical cycles, and there is ample scope for addressing the coupling between the physical forcing and biogeochemical variability in the equatorial Indian Ocean. This would need special targeted co-located measurements.

## References

- Anderson, D.L.T., Carrington, D.J., 1993. Modelling interannual variability in the Indian Ocean using momentum fluxes from the UKMO and ECMWF. *Journal of Geophysical Research*, 98, 12483-12499.
- Bathen, K.H., 1972. On the seasonal changes in the depth of mixed layer in the north Pacific Ocean. *Journal of Geophysical Research*, **77**, 7138–7150.
- Behera, SK, Yamagata, T. 2001. Subtropical SST dipole events in the southern Indian Ocean. *Geophysical Research Letters*, 28, 327–330.
- Broecker, W.S. 1991. The Great Ocean Conveyor. *Oceanography*, 4, 79-89.
- Dorman, C.E. and Bourke, R.H 1978. A temperature correction for Tucker's ocean rainfall estimates. *Q. J. Royal Meteor. Soc.*, 104, 765 – 773.
- Gadgil, S., Joseph, P. V. and Joshi, N.V 1984. Ocean atmosphere coupling over monsoon regions, *Nature*, 312, 141-143.
- Godfrey, J.S., 1996. The effect of the Indonesian throughflow on ocean circulation and heat exchange with the atmosphere: A review. *Journal of Geophysical Research*, 101, 12,217-12,238.
- Gordon, A.L., 1986. Inter ocean exchange of thermocline water. *Journal of Geophysical Research*, 91, 5037-5046.

Goswami, B.N., 1998. Interannual variations of the Indian summer monsoon in a GCM: external conditions versus internal feedbacks. *Journal of Climate*, 11, 501-522.

Greischar, L. and Hastenrath, S. 2000. The rainy seasons of the 1990s in northeast Brazil: Real-time forecasts and verification. *Journal of Climate*, 13, 3821-3826.

Hastenrath, S. and Lamb, P. J., 1979. *Climatic Atlas of the Indian Ocean. Part II: The Oceanic Heat Budget*. University of Wisconsin Press, pp.93

Hastenrath, S., and Greischar, L., 1989. Upper-Ocean Structure. Vol. 3, *Climatic Atlas of the Indian Ocean*, University of Wisconsin Press, pp. 273.

Hastenrath, S., and Greischar, L., 1993. The monsoonal heat budget of the hydrosphere-atmosphere system in the Indian Ocean sector. *Journal of Geophysical Research*, 98, 6869–6881.

Hirst, A.C. and Godfrey, J.S., 1993. The role of Indonesian throughflow in a global ocean GCM. *Journal of Physical oceanography*, 23, 1057-1086.

Hsiung, J., Newell, R.E. and Houghtby, T. 1989. The annual cycle of oceanic heat storage and oceanic meridional heat transport. *Quart. J. Roy. Meteor. Soc.*, 115, 1–28.

Huang, B., Kinter, J.L., 2002. The interannual variability in the tropical Indian Ocean and its relations to El Nino-Southern Oscillation. *Journal of Geophysical Research*, 107, pp.3199 (doi:10.1029/2001JC001278).

Jochum and Murtugudde, 2005. Internal variability of Indian ocean SST, *Journal of climate*, 18, 3726-3738.

Kindle, J.C. and Thompson, J.D., 1989. The 26- 50 days oscillation in the western Indian Ocean: Model Results. *Journal of Geophysical Research*, 94, 4721-4736.

Klein, S.A., B.J. Soden, and Lau, N.C., 1999. Remote sea surface temperature variations during ENSO: evidence for a tropical atmospheric bridge. *Journal of climate*, 12, 917-932.

Knox, R., 1976. On a long series of measurements of Indian Ocean equatorial currents near Addu Atoll. *Deep-Sea Research*, 23, 211–221.

Krishnamurti, T. N., and Ardunay, P., 1980. The 10 to 20 day westward propagating mode and breaks in the monsoons. *Tellus*, 32, 15-26.

Krishnamurti, T. N., Oosterhof, D. K. and Mehta, A. V. 1988. Air–sea interaction on the time scale of 30 to 50 days. *Journal of Atmospheric Science*, 45, 1304–1322.

Lee, T. and Marotzke, J. 1998. Seasonal cycle of meridional overturning and heat transport of the Indian Ocean. *Journal of Physical Oceanography*, 28, 923-943.

Levitus, S., 1987. Meridional Ekman heat fluxes for the world ocean and individual ocean basins. *Journal of Physical Oceanography*, 17, 1484–1492.

Levitus, S., 1982. Climatological atlas of the world ocean, NOAA Prof. Paper no. 13, U. S. Govt. Printing office, Washington, D.C., pp.173

Lukas, R. and Lindstrom, E. 1991. The mixed layer of western equatorial Pacific Ocean. *Journal of Geophysical Research*, 96, 3343–3357.

Luyten, J.R. and Roemmich D.H., 1982. Equatorial currents at semiannual period in the Indian Ocean. *Journal of Physical Oceanography*, 12, 406-413.

Madden R. and Julian, P., 1994. Observations of the 40-50 day tropical oscillation: A review. *Monthly Weather Review*, 112, 814-837.

Madden, R. A. and Julian, P.R., 1972. Description of global-scale circulation cells in the Tropics with a 40-50 day period. *Journal of Atmospheric Science*, 29, 1109-1123.

Masson S., Delecluse, P. Boulanger, J.P. and Menkes, C., 2002. A model study of the seasonal variability and formation mechanisms of the barrier layer in the eastern equatorial Indian Ocean. *Journal of Geophysical Research*, 107, 8017, doi:10.1029/2001JC000832.

Mc Phaden, M., 1982. Variability in the central Indian Ocean. Part I: Ocean dynamics. *Journal of Marine Research*, 40, 157–176.

Meyers, G., Bailey, R.J. and Worby, A.P., 1995. Geostrophic transport of Indonesian throughflow. *Deep Sea Research*, 42, 7, 1163-1174.

Murtugudde, R., Busalacchi, A.J. and Beauchamp, J., 1998. Seasonal to interannual effects of the Indonesian throughflow on the tropical Indo-Pacific basin. *Journal of Geophysical Research*, 103, C10, 21425-21441.

Murtugudde, R., and Busalacchi, A.J., 1999. Interannual variability of the dynamics and thermodynamics of the tropical Indian Ocean. *Journal of Climate*, 12, 2300-2326.

Murtugudde, R., McCreary, J.P. and Busalacchi, A.J., 2000. Oceanic processes associated with anomalous events in the Indian Ocean with relevance to 1997-98. *Journal of Geophysical Research*, 105, 3295-3306.

O'Brien, J. J., and Hurlburt, H. E., 1974. Equatorial jet in the Indian Ocean: Theory, *Science*, 184, 1075-1077.

Potemra, J.T., 1999. Contribution of equatorial Pacific winds to southern tropical Indian Ocean Rossby waves. *Journal of Geophysical Research*, 106, pp. 2407.

Rao, R.R., Molinari, R.L. and Festa, J.F., 1989. Evolution of the climatological near-surface thermal structure of the tropical Indian Ocean. 1. Description of mean monthly mixed layer depth, and sea surface temperature, surface current, and surface meteorological fields. *Journal of Geophysical Research*, 94, 10 801-10 815.

Rao, R.R., Sivakumar, R., 2000. Seasonal variability of near-surface thermal structure and heat budget of the mixed layer of the Indian Ocean from new global ocean temperature climatology. *Journal of Geophysical Research*, 105, 995-1015.

Rao, A.S, Behera, S.K., Masumoto, Y. and Yamagata, T., 2002. Interannual variability in the subsurface Indian Ocean with special emphasis on the Indian Ocean Dipole. *Deep Sea Research-II*, 49, 1549-1572.

Reverdin, G., Luyten, J., 1986. Near-surface meanders in the equatorial Indian Ocean. *Journal of Physical Oceanography*, 16, 16, 1088-1100.

Reverdin, Gilles.,1987. The Upper Equatorial Indian Ocean-The Climatological Seasonal Cycle. *Journal of Physical Oceanography*, 17, 7, 903-927.

Reynolds, R.W. 1988. A real-time global sea surface temperature analysis. *Journal of Climate*, 175-86.

Rodwell, Mark J., Hoskins, Brian J., 1995. A Model of the Asian Summer Monsoon. Part II: Cross-Equatorial Flow and PV Behavior. *Journal of the Atmospheric Sciences*: 52, No. 9, 1329-1340.

Saji, N.H., Goswami, B.N., Vinayachandran, P.N., Yamagata, T., 1999. A dipole mode in the tropical Indian Ocean. *Nature*, 401, 360-363.

Schiller, A., Godfrey, J.S., McIntosh, P.C., Meyers G. and Wijffels, S.E., 1998. Seasonal near-surface dynamics of the Indian Ocean and Indonesian throughflow in a global ocean general circulation model. *Journal of Physical Oceanography*. 28, 2288-2312.

Schneider, N. and Muller, P., 1990. The meridional and seasonal structures of the mixed layer depth and its diurnal amplitude observed during the Hawaii-to-Tahiti shuttle experiment. *Journal of Physical Oceanography*, 20, 1395–1404.

Schneider, N. and Barnett, T.P., 1997. Indonesian throughflow in a coupled general circulation model. *Journal of Geophysical Research*, 102, C6, 12341-12358.



Schott, F. A., and J. P. McCreary Jr., 2001. The monsoon circulation of the Indian Ocean. *Progress in Oceanography*, 51, Elsevier, 1–123.

Sikka, D.R., Sulochana Gadgil, 1980. On the Maximum Cloud Zone and the ITCZ over Indian longitudes during the Southwest Monsoon. *Monthly Weather Review*, 108, 1840-1853.

Sprintall, J., Gordon, A. L., Murtugudde, R. and Susanto, R. D., 2000. A semiannual Indian Ocean forced Kelvin wave observed in the Indonesian seas in May 1997, *Journal of Geophysical Research*, 105, 17,217 – 17,230.

Sprintall, J., Tomczak, M., 1992. Evidence of the barrier layer in the surface layer of the tropics, *Journal of Geophysical Research*, 97, 7305 – 7316.

Stull, R. B., 1988. *An Introduction to Boundary Layer Meteorology*. Kluwer Academic, pp.666.

Tomczak, M. and Godfrey, J.S. 1994. *Regional Oceanography : An Introduction*. Pergamon, pp. 422.

Tsai, P.T.H., Brien, J. O and Luther, M.E., 1992. The 26-day oscillation observed in the satellite sea surface temperature measurements in the equatorial western Indian Ocean. *J. Geophysical Research*, 97, 9605-9618.

Tucker, G. B., 1961. Precipitation over the North Atlantic Ocean. *Q. J. Royal Meteor. Soc.*, 87, 147 - 158.

Wyrski, K., 1964. The thermal structure of the eastern Pacific Ocean, Deutsche Hydrographic Zeitschrift Supplement, A8, 6–84.

Wyrski, K., 1973. An equatorial jet in the Indian Ocean. *Science*, 181, 262-264.

Xie, S.P., Annamalai, H., Schott, F.A., McCreary, J.P., 2002. Structure and mechanisms of south Indian Ocean climate variability. *Journal of Climate*, 15,867 –878.

Yamagata, T., Keizeku, M. and Masumoto, Y. 1996. Seasonal variations in the equatorial Indian Ocean and their impact on the Lombok throughflow. *Journal of Geophysical Research*, 101, 12 465-12 473.

Yasunari, Y., 1981. Structure of an Indian summer monsoon system with around 40-day period; *Journal of Meteorological Society, Japan*, 59, 336-354.